Oscillating Gradient Spin Echo (OGSE): A Study of Short Diffusion Time Effects in Human Brain at 3T

by

Maria Fernanda Padron Olivas

A thesis submitted in partial fulfillment of the requirements for the degree of

Master of Science

Department of Biomedical Engineering

University of Alberta

Abstract

Diffusion-weighted magnetic resonance imaging (DWI) is a non-invasive MRI technique that is sensitive to the diffusion of water molecules within the body. Its ability to encode water displacements enables it to detect changes in neural microstructure, such as those due to normal healthy aging or even those caused by pathological conditions. Diffusion MRI sequences will be less or more sensitive to diffusion depending upon the time that they encode or measure these displacements, known as the diffusion time. For instance, the oscillating gradient spin echo (OGSE) diffusion sequence encodes water diffusion within the frequency spectrum of its gradient oscillations. As the frequency is increased, the diffusion time decreases and water molecules will reach less cellular boundaries over larger spatial scales. With less restrictions to diffusion, measurable changes in diffusion parameters can be detected, such as an increase in mean and radial diffusivities (MD and RD, respectively). Hence, OGSE can unmask spatial-dimension tissue differences (e.g. such as axon diameters) and achieve unique imaging contrast mechanisms related to cell size, as found previously in animal models.

However, translating OGSE to human applications is highly challenging due to hardware constraints (such as limited gradient strength) in clinical scanners. Consequently, there are only a few OGSE studies in healthy human brain, using frequencies in the range of $f =$ 18-63 Hz. In this work, OGSE was evaluated in human brain on a 3T clinical MRI system with oscillation frequencies of $f = 40 - 50$ Hz. The acquired images provided adequate data quality and greater OGSE MD values relative to the MD from the conventional diffusion sequence pulsed gradient spin echo (PGSE). Nonetheless, raw OGSE and PGSE scans demonstrated image artifacts such as Gibbs ringing (GR) that affected the accurate estimation of diffusion metrics, necessitating image acquisition optimization.

Fluid-attenuated inversion-recovery (FLAIR) was implemented for the first time with OGSE in acquisition to suppress the sharp signal intensity transitions at cerebrospinal fluid (CSF)/tissue boundaries causing the ringing. FLAIR was found effective in preventing GR as compared to remedial post-acquisition correction methods, as it substantially increased image quality in OGSE/PGSE DWIs and provided homogeneous MD maps. Region-of-interest analysis was then performed on several white matter tracts and two deep gray matter structures in eight subjects on OGSE FLAIR - PGSE FLAIR diffusion maps. Results from the OGSE-PGSE difference maps showed significantly elevated MD and RD with shorter diffusion time in the corticospinal tract, superior longitudinal fasciculus, and posterior limb of the internal capsule, that was greater than in the other white matter tracts and both gray matter regions.

OGSE FLAIR, although characterized by lengthy scan times, proved a reliable and effective method to investigate potential axon-scale differences in healthy white matter, with potential to explore changes in tissue microstructure in the mechanisms of disease.

Preface

This thesis is an original work by María Fernanda Padrón Olivas. The research project, of which this thesis is a part, received research ethics approval from the University of Alberta Research Ethics Board, Project Name "Development of Magnetic Resonance Imaging and Its Application to Human Disease (Controls)", No. Pro00002112, 2017-2019.

Chapter 3 of this thesis will be submitted for publication.

To my parents Victor and Lupita,

For teaching me that the only limit is the one we set for ourselves.

It would not be much of a universe if it wasn't home to the people you love.

– Stephen Hawking

Excellence is an art won by training and habituation: we do not act rightly because we have virtue or excellence, but we rather have these because we have acted rightly… we are what we repeatedly do. Excellence, then, is not an act but a habit.

– Will Durant

Acknowledgements

There are multiple people whom I would like to acknowledge for their support in the development of this thesis. To start I would like to express my superior gratitude to my supervisor, Dr. Christian Beaulieu, for his extraordinary guidance and teachings, for sharing his wisdom and inspiring me to uncover the answers to our research questions. I will always feel thankful and honored to have been his student and a part of his research lab. A sincere thank you to my supervisory committee members, Rob Stobbe and Alan Wilman, for taking the time to revise my thesis and contributing with much valuable feedback. In addition, I want to thank Thorsten Feiweier for developing the Advanced Diffusion WIP and enabling it on our Siemens Prisma 3T scanner, which ultimately constituted the basis of my work.

Thanks to Peter Seres for his patience in helping me acquire my experiments and teaching me to operate the MRI scanner on my own. Thanks to Maisie Goh for always keeping me on track with my paperwork and for her worthy advice on student matters and life in general. Moreover, I would like to express my appreciation to Catherine Leung for her kindness and the occasional delicious pastries she generously shared with me.

A special thank you to my fellow lab colleagues, for introducing me to research practices and solving my work-related doubts. To all my RTF friends, for bearing with me and making these two years in Edmonton feel like home, in addition to being my gym buddies and putting up with my crazy workouts. It was truly a pleasure to meet everyone and to learn about the diverse cultural backgrounds. Lunchtime together was always enjoyable since I had the chance to taste the traditional homemade cuisines from the

respective different countries. I know that our friendships will continue being and hope that you will visit Mexico to try authentic flavorsome tacos.

To my parents, Victor and Lupita, and my brother, Alex, my deepest gratitude for their unconditional support throughout my graduate studies. Without them, this dream would never have been possible. Their loving and motivational talks always recharged my spirits and kept me moving forward. I would also like to thank my significant other, Christian Arvizu, for encouraging me every day towards the completion of my program and providing me kind and loving words of support. In addition and very importantly, I would like to thank God for taking care of me, for answering my prayers, and for being by my side throughout this journey.

Finally, I would like to acknowledge and thank the Mexican National Council of Science and Technology (CONACYT), the Government of Mexico, the Canadian Institutes of Health Research (CIHR), and the Heart and Stroke Foundation of Canada for funding my research and Master's program, thereby making this accomplishment possible.

Contents

List of Tables

List of Figures

Symbols and Abbreviations

$\boldsymbol{\Delta}$	time interval between diffusion gradient pulses
$\boldsymbol{\delta}$	diffusion gradient duration
$\boldsymbol{\Delta_{eff}}$	effective diffusion time
$\boldsymbol{\gamma}$	gyromagnetic ratio
$\boldsymbol{\lambda_{\parallel}}$	parallel diffusivity
$\boldsymbol{\lambda_{\perp}}$	perpendicular diffusivity
$\boldsymbol{\omega}$	angular precessional frequency
$\boldsymbol{B_0}$	static magnetic field strength
$\boldsymbol{D}$	Diffusion coefficient
ACR	Anterior corona radiata
ADC	Apparent diffusion coefficient
AD	Axial diffusivity
AxD	Axon diameter
CNS	Central nervous system
CSF	Cerebrospinal fluid
CST	Corticospinal tract
D$_{\perp}$	Perpendicular diffusion coefficient
DDR$_{\perp}$	Perpendicular diffusion dispersion rate
DWI	Diffusion weighted imaging
EPI	Echo planar imaging
FACT	Fiber Assignment by Continuous Tracking
FA	Fractional anisotropy
FLAIR	Fluid-attenuated inversion recovery
FOV	Field of view

gCC	Genu of corpus callosum
GM	Gray matter
GRAPPA	Generalized Autocalibrating Partially Parallel Acquisitions
GR	Gibbs ringing
IVIM	Intravoxel incoherent motions
MD	Mean diffusivity
MRI	Magnetic Resonance Imaging
MSD	Mean-squared displacement
NEX	Number of excitations
NMR	Nuclear Magnetic Resonance
OGSE	Oscillating gradient spin echo
PGSE	Pulsed gradient spin echo
PIS	Physically implausible signals
PLIC	Posterior limb of the internal capsule
PPF	Phase partial Fourier
RD	Radial diffusivity
RF	Radiofrequency
R	Acceleration factor
sCC	Splenium of the corpus callosum
SCR	Superior corona radiata
SLF	Superior longitudinal fasciculus
SNR	Signal-to-noise ratio
SS-EPI	Single-shot echo-planar imaging
T1	Longitudinal relaxation time/ Spin-lattice relaxation
T2	Transverse relaxation time/ Spin-spin relaxation
TA	Total acquisition time
TE	Echo time
TI	Inversion time
TR	Repetition time
TV	Total Variation
WM	White matter
ZF	zero filling

1 Introduction to Diffusion MRI

Magnetic Resonance Imaging or MRI is a non-invasive medical imaging technique that can capture in vivo anatomical images of the body, particularly useful for soft tissues. Additional to imaging structures, this technology expands our understanding of human physiology in both health and disease, providing information regarding normal bodily processes as well as being a valuable diagnostic tool to examine the mechanisms behind different pathologies.

However, the basic contrast mechanisms available for standard MRI, namely T1, T2, and proton density, offer limited or no information on structural connectivity of the brain. Diffusion weighted imaging (DWI) is an MRI technique that overcomes such limitations. It constitutes not only a methodology to image the structure, but also a tool to estimate axonal connections and orientations while additionally allowing the quantification of diffusion parameters relevant to depict healthy and abnormal conditions (e.g. ischemic stroke). The characteristic capabilities of diffusion MRI arise from its sensitivity to the displacement of water molecules within biological cellular compartments. Based on the time allowed for molecules to diffuse, they are expected to reach different hindrance levels. Hence, a comparison of the obtained diffusion parameters as a function of diffusion time can reveal more detailed information from the underlying microstructure.

Over the past few years, an approach has been increasingly used in animal models (and more recently in few human studies) to image at short diffusion times: the Oscillating Gradient Spin Echo (OGSE) diffusion sequence. Due to the nature of the oscillating gradients, the OGSE method is able to explore smaller-scale diffusion restrictions, enabling a greater insight and understanding of tissue organization in vivo. However, human brain OGSE acquisitions face numerous limitations, including problematic hardware restrictions that hamper the use of desired scanning parameters and degrade image quality. The aim of this research then is to design a viable OGSE protocol at 3T to obtain high-quality human brain images at short diffusion times and through the measurement of diffusion metrics, infer details on the composition of the intricate brain microstructure.

1.1 Self-Diffusion of Water Molecules

Every particle, being liquid or gas, experiences molecular diffusion at a temperature above zero on the Kelvin scale due to thermal energy. Robert Brown first made this observation in 1827 when he detected a self-diffusing motion of pollen particles suspended in water [1], thereupon identifying the phenomenon with the term Brownian motion. Molecules present in an isotropic medium (i.e. free diffusion, such as in a water container) diffuse unobstructed and collide only with other adjacent water molecules. Therefore, they exhibit an equal probability of diffusing in any direction under a specified amount of time.

That is, for a hypothetical case of a particle diffusing in one dimension, it has an equal probability of moving either one step forward (+1) or one step backward (-1). If the experiment was repeated multiple times, after a time t, the molecule's average traveled distance would equal zero and its displacement could effectively be modeled using a Gaussian distribution (i.e. consequentially also termed Gaussian diffusion). However, no useful information can be extracted from a zero net displacement. To overcome this shortfall, Albert Einstein later developed a mathematical model based upon Brown's observations to describe the molecules' displacement as a *mean* *squared displacement* [2]:

$$\langle x^2 \rangle = n_i D t \tag{1.1}$$

where x^2 is the mean-squared displacement (MSD) of the diffusive particle, n_i is a constant dependent on the particle's dimensionality of displacement (i.e. $n_i = 2$, 4, and 6 for dimensions 1 (along x, or i=x), 2 (along y, or i=y), and 3 (along z, or i=z), respectively), D is the diffusion coefficient (itself reliant on a frictional coefficient, Boltzmann's constant, and the absolute temperature of the medium), and t is the diffusion time. An alternative terminology that has been used to describe the unpredicted molecular diffusions is 'random walk', as illustrated in Figure 1.1 for a particle moving in a three-dimensional space.

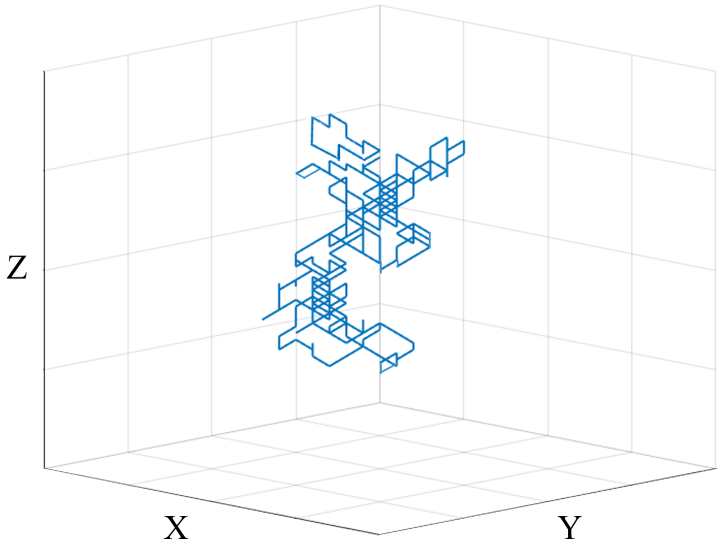

Figure 1.1: Random walk. Simulation of path traveled by random walk of a water molecule in a three-dimensional space after N = 100 steps.

Such valuable work led to many important applications, including the foundation for diffusion effects in Nuclear Magnetic Resonance (NMR) in the 1950s [3–5] and its later implementation in human studies, discussed in the next section.

1.2 Diffusion Imaging in MR

1.2.1 The Diffusion Encoding Scheme

The human body is composed of approximately 60% water [6]. As discussed before, water molecules are in constant movement and interact with surrounding elements, spreading in unpredicted directions. Important information can be extracted from this characteristic random walk within the body by sampling tissue microstructure using Diffusion MRI. It all started in 1965, when Stejskal and Tanner developed the Pulsed Gradient Spin Echo (PGSE) method to measure the diffusion of spins by applying a pair of pulsed gradients [7] on a simple spin-echo sequence [3]. Recalling the basics of MRI, a linear gradient alters the spins' frequency of precession by spatially varying the magnetic field they perceive (i.e. slightly adding and/or subtracting from the static magnetic field), as of the Larmor equation:

$$\omega(r) = \gamma(B_0 + G \cdot r) \tag{1.2}$$

where ω is the precessional frequency, γ is the gyromagnetic ratio unique for every nuclear species (i.e. for hydrogen 2.675×10^8 rad/s/T or 42.58 MHz/T), B_0 is the strength of the main magnetic field, G is the applied magnetic field gradient parallel to B_0, and r is the position of the spins. After the first diffusion gradient is applied subsequent to the excitation radiofrequency (RF) pulse, the spin phase coherence becomes disrupted dependent on the spin locations. Explicitly, as the gradient varies the magnetic field, some protons will precess at a slightly faster speed than others. Therefore, by the end of the first 'dephasing' gradient, protons will be out of phase (Figure 1.2A). A second gradient set after the refocusing pulse will essentially reverse the phase incoherence, causing the slower protons to precess more rapidly and vice versa. By the end of the 'rephasing' gradient, spin phase coherence will be restored and the full diffusion-weighted MR signal can be acquired (Figure 1.2A).

The previous scenario assumes that the spins remained static during the application of the diffusion-sensitizing gradients. However, in reality this is never the case. As mentioned previously, water molecules are in constant motion due to thermal energy. To illustrate an example, one can simplify the explanation by referring to an individual diffusing spin. Initially, the spin will experience the dephasing gradient and precess at a different frequency than its fellow neighbors. After a diffusion time Δ, the spin will disperse and perceive a different 'unexpected' magnetic field in its new location, causing it to change phase. Considering that all water molecules have also diffused, the rephasing gradient will fail to converge the transverse magnetization (bulk dephasing) inducing a collective loss of signal (Figure 1.2B).

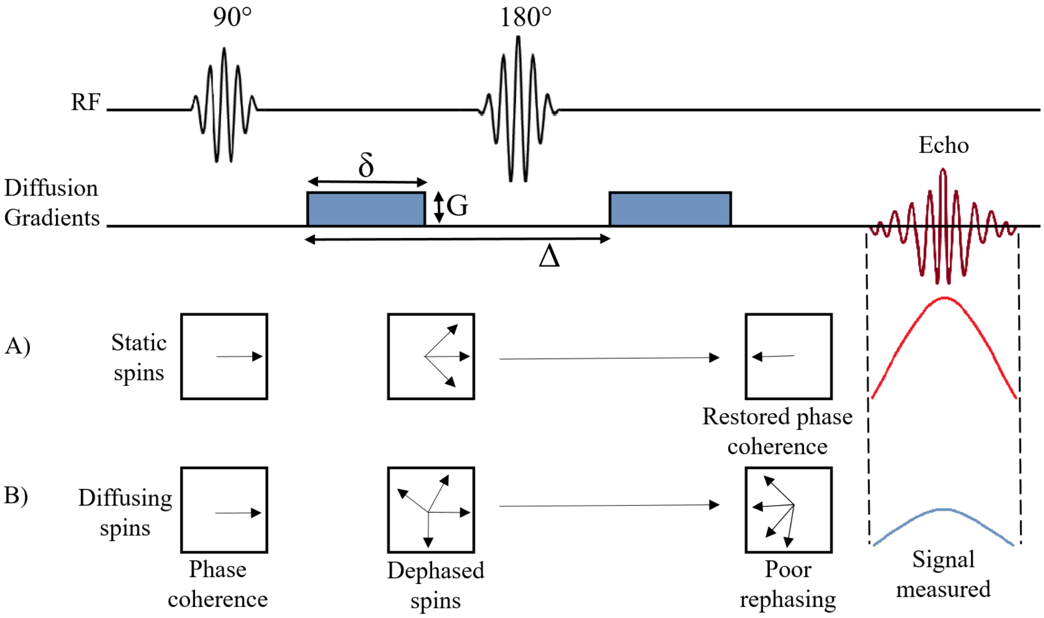

Figure 1.2: Diffusion gradients. Schematic of typical application of diffusion pulsed gradients in an environment with A) static spins, and B) diffusing spins. Adapted from Patterson et al., 2008. [8]

In brief, Diffusion MR is able to measure diffusion of spins by 'tagging' them with phase and measuring the difference in signal reduction. It is important to note that the gradient pairs only spatially encode water displacement along the predetermined axis, thus they are conventionally applied in all three orthogonal directions: X-gradient (encodes diffusion from left to right), Y-gradient (encodes diffusion in the anterior-posterior direction) and Z-gradient (encodes diffusion superior-inferior).

The pair of diffusion gradients is formally known as the pulsed gradient spin-echo (PGSE) diffusion sequence, which has been the gold-standard method to measure molecular motion. An equal amplitude G, duration δ, and time interval between the two gradient pulses (known as the diffusion time) define both gradients (Figure 1.2). A combination of these parameters governs the amount of signal attenuation due to diffusion according to the Stejskal-Tanner equation [7]:

$$Ln\left(\frac{S_1}{S_0}\right) = -\gamma^2 G^2 \delta^2 D\left(\Delta - \frac{\delta}{3}\right) \tag{1.3}$$

where the signal attenuated by diffusion is denoted by S_1, S_0 represents the signal without diffusion encoding (no diffusion gradients applied), γ is the gyromagnetic ratio, G and δ are the gradient-pulse amplitude and length, D is the diffusion coefficient, and (Δ-δ/3) is the effective diffusion time ($_{\text{eff}}$), namely the time during which water displacement is sampled. In DWI, a selection of the parameters from equation (1.3) are grouped into a single element defined as the *b*-value:

$$b = -\gamma^2 G^2 \delta^2 \left(\Delta - \frac{\delta}{3}\right) \tag{1.4}$$

where b is the *b*-value in units of s/mm^2 that indicates a measure of diffusion weighting or of how sensitive the signal is to diffusion. The greater the *b*-value, the greater the diffusion weighting and induced signal loss. Simplifying equation (1.3):

$$Ln\left(\frac{S_1}{S_0}\right) = -bD \tag{1.5}$$

It was not until 1984 that the diffusion coefficient (formerly named *translational molecular self-diffusion coefficient*) was measured for the first time through in vitro MRI experiments of various fluids [9], followed by a similar NMR study in 1985 [10].

1.2.2 Tissue Compartmentalization Impact on Diffusion

1.2.2.1 Restricted and Hindered Diffusion

Until now, the word diffusion has exclusively been used to refer to a *free* diffusion regime. Nonetheless, there remains two additional types of diffusion that should be discussed in order to understand the relevance of DWI in biological systems. Within tissue, one can find numerous types of cellular compartments such as membranes and organelles that act as barriers to water diffusion. Diffusion under these circumstances is then considered to transition from a free state to a restricted or hindered environment. In the case of impermeable membranes such as inside cell boundaries, water molecules are strictly confined and their dispersion is limited solely within the compartment's perimeter; this type of intracellular diffusion is known as *restricted diffusion* (Figure 1.3).

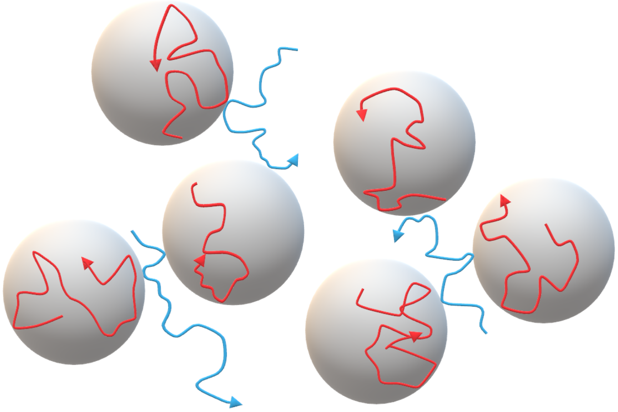

Figure 1.3: Restricted and hindered diffusion. Illustration depicting color-coded random water molecule displacements for restricted diffusion (red) inside impermeable cellular membranes and hindered diffusion (blue) naturally occurring in the interstitial fluid.

However, inside the interstitial fluid surrounding cell bodies (otherwise known as the extracellular space), the diffusion of water molecules is not entirely restricted but only partially obstructed by the multiple interactions with nearby cellular structures. Water molecules will technically be able to travel any distance (only in a longer amount of time), meanwhile colliding with each other as well as bumping back and forth between cellular membranes. Diffusion under this setting is identified as *hindered diffusion* (Figure 1.3).

With a displacement now dependent on the nature of microstructure compartmentalization, both restricted and hindered diffusion types now fall into a non-Gaussian distribution. Intuitively, the diffusion coefficient D will also vary between free, hindered, and restricted diffusion; that is, if it were to be plotted as a slope, D would decrease as it shifted from a free regime to a restricted regime (Figure 1.4).

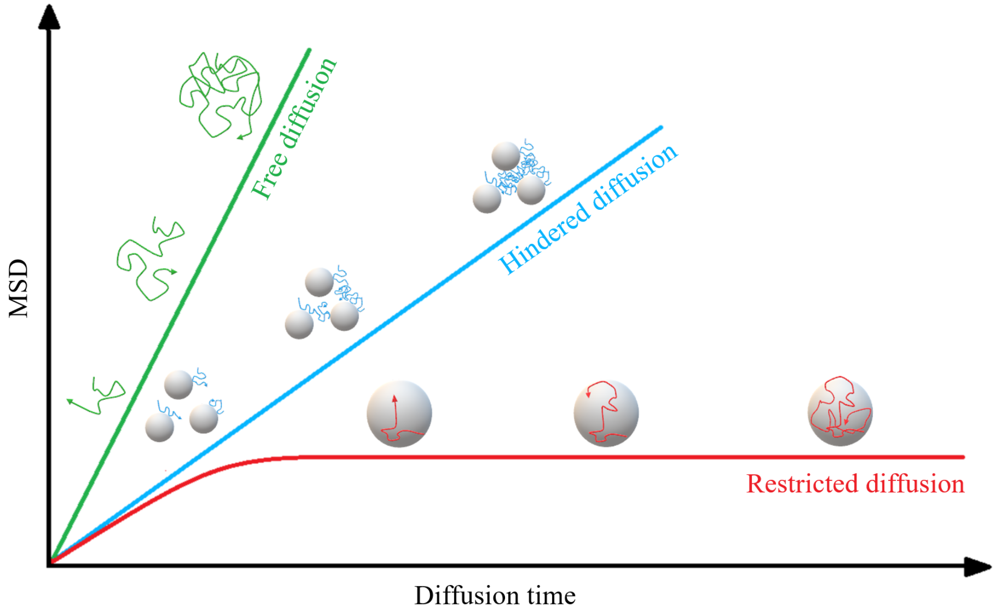

Figure 1.4: Mean squared displacement (MSD) depicted for different diffusion regimes as a function of time. By adjusting the slope (i.e. the diffusion coefficient D), one can represent free (green), hindered (blue), and restricted (red) diffusion regimes. Notice that for restricted diffusion, the MSD reaches a maximum limit as diffusion time increases.

1.2.2.2 The Apparent Diffusion Coefficient

Revisiting Einstein's diffusion equation (1.1), for a free water diffusion coefficient of $D = 3 \times 10^{-3}$ mm^2/s at 37° and diffusion time t=40 ms on a typical PGSE MRI study, the one dimensional displacement covered by a water molecule approximates 15 μm. Upon previous analyses, however, it is evident that for biological tissues the diffusion coefficient is strongly dependent on the geometric properties of the medium as well as of the time that water molecules are allowed to probe it. In the case of restrictions, molecular diffusion is strictly confined within a perimeter. During the same time frame of $t=$ 40 ms for an axon diameter of 5 μm, water molecules will long have reached the bounds of the cellular compartment and will thereafter diffuse only within the limited available area, causing a reduction of the diffusion coefficient.

Additionally, other factors regarding biological tissues must be considered. Le Bihan and others[11] observed that perfusion – blood microcirculation in the capillaries – could potentially simulate molecular water diffusion effects collected by diffusion MRI and slightly overestimate the calculation of the diffusion coefficient, particularly for very small b-values ($<$180 s/mm^2) [12]. Le Bihan and collaborators then identified this phenomenon and any additional incoherent fluid motions inside a single voxel as *intravoxel incoherent motions* (IVIM)[11].

Under the past contemplations, the diffusion coefficient term D no longer holds, but is replaced by a more inclusive designation, the *apparent diffusion coefficient* (ADC) [11]. Correspondingly, the term D in equation (1.5) is simply substituted by the term ADC; rearranging the equation yields:

$$Ln(S_1) = Ln(S_0) - b \cdot ADC \tag{1.6}$$

Clearly, there exists a linear relationship between the natural logarithm of the attenuated signal S_1 and the b-value, where the ADC represents a negative slope. In order to calculate the ADC, measurements from two different b-values are required, as shown by the simplified equation (1.7):

$$ADC = \frac{Ln(S_0) - Ln(S_1)}{b_1 - b_0} \tag{1.7}$$

where S_1 and S_0 are measured signal intensities from a diffusion-weighted image with b_1 and a non-diffusion weighted image b_0 (b-value = 0 s/mm^2), correspondingly. Figure 1.5 displays an example of signal dependence on b-value for three different slopes. As the slope becomes steeper, greater signal loss is expected at a given b-value, which is reflected as a higher ADC (i.e. red= low ADC, blue= neutral ADC, green= high ADC).

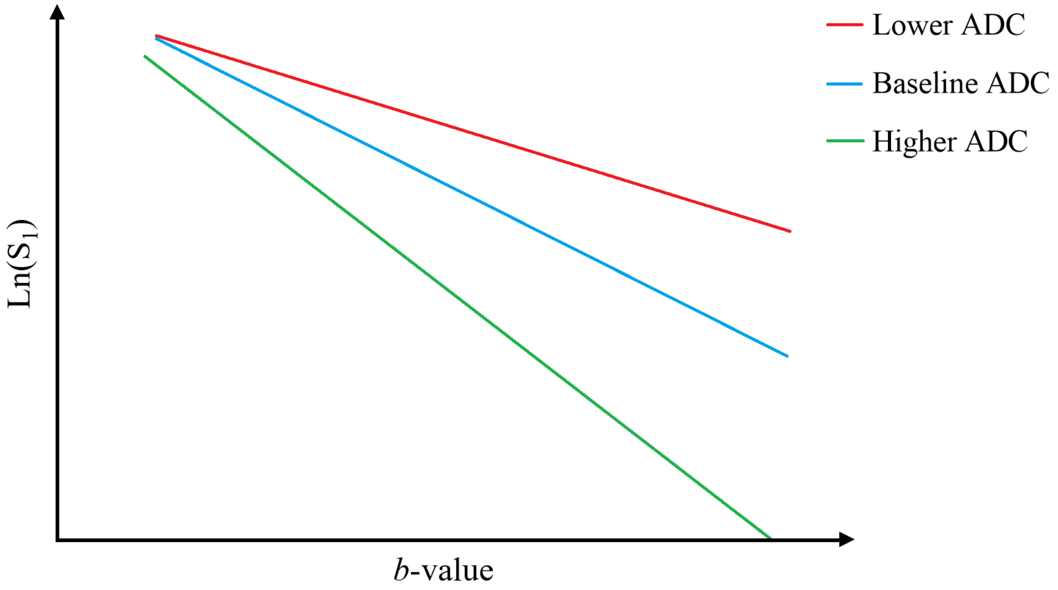

Figure 1.5: $\mathbf{Ln(S_1)}$ as a function of b-value. The ADC slope will determine the level of signal loss at each b-value; a high ADC reflects more signal loss (i.e. green line) compared to a low ADC (i.e. red line).

Knowledge of the ADC can help infer the level of water restriction and uncover micrometer-scale differences within tissue, helping to understand diffusion processes in both health and disease [13].

1.2.2.3 Isotropic vs. Anisotropic Diffusion

Molecular water diffusion is directly determined by the physical nature of the medium in which it diffuses. In cerebrospinal fluid (CSF) or say in a simple glass of water, water molecules can disperse freely in any direction. Furthermore, water is able to diffuse in any direction equally if the environment presents an arbitrary, incoherent distribution, such is the case of gray matter (GM) [14, 15]. This kind of diffusion is known as *isotropic diffusion.*

Nonetheless, in the white matter (WM), water molecules are constrained inside and around numerous, tightly packed parallel fibers: the axons. These coherent neural projections force water molecules to move predominantly along the axon as opposed to perpendicular, with a diffusion as much as four times slower for the latter [16]. Consequentially, a deviation from the intrinsic diffusion coefficient D is observed. When diffusion undergoes this type of directionality, it is termed *anisotropic diffusion* [17] (Figure 1.6).

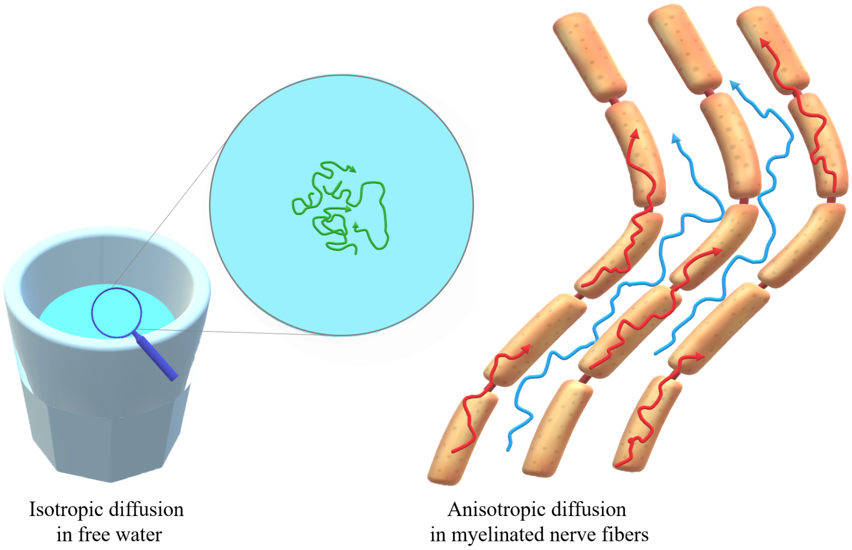

Figure 1.6: Isotropic vs anisotropic diffusion. Left: Isotropic diffusion in a glass water sample; molecules experience a random walk and diffuse freely with no particular direction. Right: Anisotropic diffusion in myelinated nerve fibers; water travels predominantly along the axon.

For a long time it was believed the primary element that governed diffusion anisotropy in nerve fibers was the myelin sheath, additional to the axonal membrane and cytoskeleton (neurofibrils such as neurofilaments and microtubules). An investigation on garfish nerves uncovered that both nonmyelinated and myelinated axons sustained a comparable amount of anisotropy, proving myelin is not a determining factor [18]. Moreover, a subsequent study of the giant axon of the squid concluded that the longitudinally oriented neurofilaments did not significantly contribute to water anisotropy in the axon; hence, the axonal membrane was determined as the main source of axonal anisotropic diffusion [19].

Recalling diffusion MRI basics, an important aspect of diffusion gradients is that they are sensitive to diffusion *only* along their axis of application. This characteristic is not as relevant under isotropic diffusion conditions, since water diffuses equally in any direction. However, in a living system with complex tissue organization that features anisotropic diffusion, a need to efficiently quantify diffusion along specific directions emerges. Axonal fibers are now coercing water to move in a particular path; therefore, the MRI scanner should be capable of acquiring signal in any given direction. By applying orthogonal diffusion gradients on the X, Y, and Z axis (or a combination of them), anisotropy-guided tissue properties unique to the underlying structures can be explored through signal intensity variations (Figure 1.7). Rather than being a drawback, anisotropy presents an advantage by serving as a means to investigate the configuration of the intricate brain microstructure, giving insight into the anatomical organization.

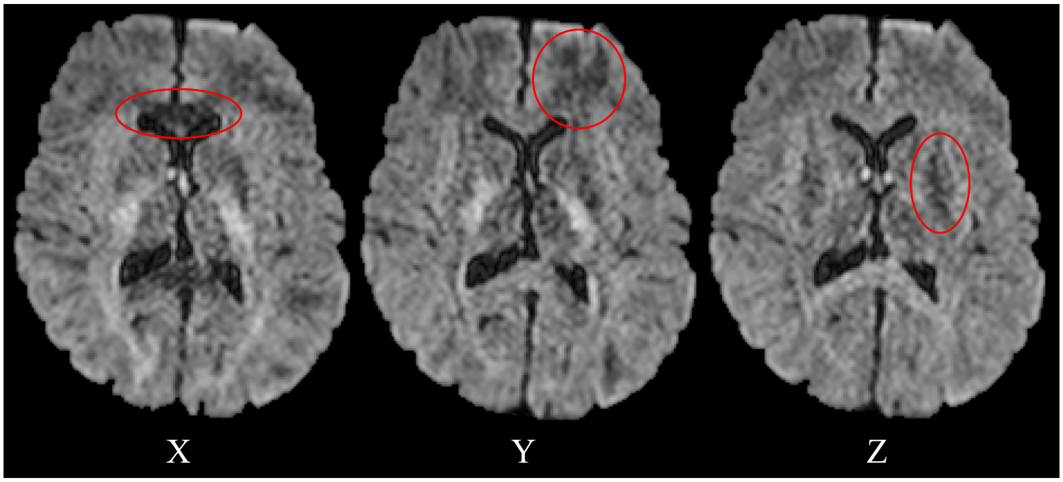

Figure 1.7: DWI images using X, Y, and Z diffusion gradients. Raw DWI images acquired with three orthogonal gradients. Areas circled in red highlight the principal direction of diffusion for underlying brain tissue (portrayed as a lower signal intensity). Left: X-gradient, higher diffusion in the genu of the corpus callosum. Center: Y-gradient, higher diffusion around the anterior region of corona radiata. Right: Z-gradient, higher diffusion in the corticospinal tract.

In summary, biological compartments (such as axonal membranes, fibers, organelles, etc.) introduce barriers that hinder/restrict water diffusion, which in turn offer a peculiar advantage. MRI studies of anisotropic water diffusion in the brain facilitate the understanding of the complicated processes occurring in the underlying microstructure by way of exploring a wide range of diffusion times and calculating the diffusion coefficient for different levels of restriction to infer the anatomic distribution of the environment at a sub-micrometer scale. The methodology through which diffusion MRI processes this information is discussed in the next section.

1.3 Diffusion Tensor Imaging (DTI)

Diffusion tensor imaging (DTI) is a diffusion MRI technique that not only quantifies, but models the main direction of diffusion as a 3-dimensional tensor, as first proposed in 1994 [20]. The importance of this technique lies in its ability to noninvasively characterize diffusion in anisotropic settings, and added to the anatomical and physiological information it reveals of biological tissues (i.e. such as the healthy macroscopic orientation of axon fibers in the nervous system, and any observed changes in the mechanisms of disease) through a variety of calculated diffusion parameters. The following sections expand on the DTI practice further.

1.3.1 The Diffusion Tensor: Mathematical Modeling

In isotropic conditions, the mean squared displacement of thermally driven water molecules remains equal in all directions; therefore, diffusion can be represented by a *sphere* (Figure 1.8A). Conversely, anisotropic diffusion is otherwise characterized by a dominant direction of diffusion, as seen along the nerve fibers in white matter [14, 16–18] and any coherently oriented barriers (i.e. cardiac muscle [21] and skeletal muscle [22]); this type of diffusion can be modeled as an *ellipsoid* (Figure 1.8B). The mathematical model behind the diffusion ellipsoid estimates and quantifies fiber-oriented anisotropic diffusion in every voxel of DWI images, and receives the name of the *diffusion tensor* $\boldsymbol{D}$ [23].

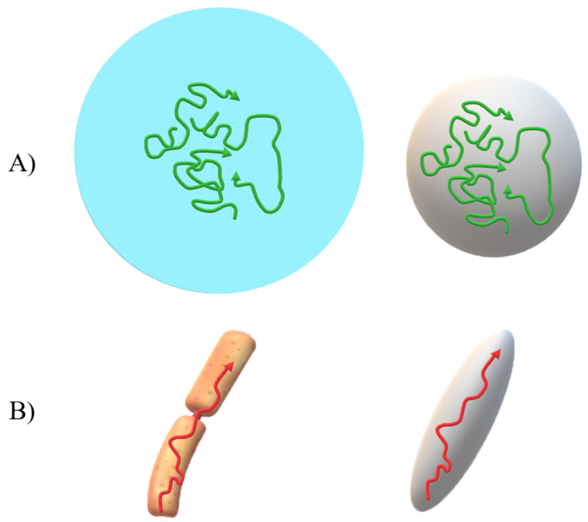

Figure 1.8: Modeling the diffusion ellipsoid. A) Isotropic diffusion can be mathematically modeled as a sphere. B) Anisotropic diffusion, such as that along nerve fibers in white matter is modeled as a diffusion ellipsoid.

For complex anisotropic media, a reformed version of (1.6) is mandatory to model diffusion as a 3-dimensional tensor. Hence, the tensor **D** is calculated for every voxel upon signal measurements from the DWIs in combination with the applied gradients in terms of the corresponding **b**-matrices [20, 24]:

$$\begin{aligned} Ln\left(\frac{S_1}{S_0}\right) &= -\sum_{i=1}^{3}\sum_{j=1}^{3} b_{ij}D_{ij} \\ &= -(b_{xx}D_{xx} + 2b_{xy}D_{xy} + 2b_{xz}D_{xz} + b_{yy}D_{yy} + 2b_{yz}D_{yz} + b_{zz}D_{zz}) \end{aligned} \tag{1.8}$$

where b_{ij} is a component of a symmetric **b**-matrix (a more inclusive b-factor that considers all applied gradients specific to the sequence) and D_{ij} is an element of the diffusion tensor **D**. It was proved previously that the ADC in diffusion imaging is calculated from the measured signal intensities of two DWIs and the b-value (b-factor) using simple linear regression equation (1.7). Likewise, for the case of diffusion *tensor* imaging a set of DWIs and affiliated **b**-matrices are utilized instead to estimate the diffusion tensor **D** using weighted multivariate linear regression [25]. The diffusion tensor **D** can then be reconstructed as a 3×3 array:

$$\mathbf{D} = \begin{bmatrix} D_{xx} & D_{xy} & D_{xz} \\ D_{yx} & D_{yy} & D_{yz} \\ D_{zx} & D_{zy} & D_{zz} \end{bmatrix} \tag{1.9}$$

Since the matrix is symmetric ($\mathrm{D_{xy}{=}D_{yx}}$, $\mathrm{D_{xz}{=}D_{zx}}$, $\mathrm{D_{yz}{=}D_{zy}}$) it contains only six unique components, and each one of them relies on the specific diffusion characteristics of the tissue. With six unknown elements of the diffusion tensor, a minimum of seven DWIs are required for the calculation –a b0 image and at least six DWIs– with each DWI acquired at a different non-collinear gradient direction [20, 26] (Figure 1.9). However, the greater the amount of acquisitions, the less susceptible the tensor is to noise, achieving a more robust estimation [27].

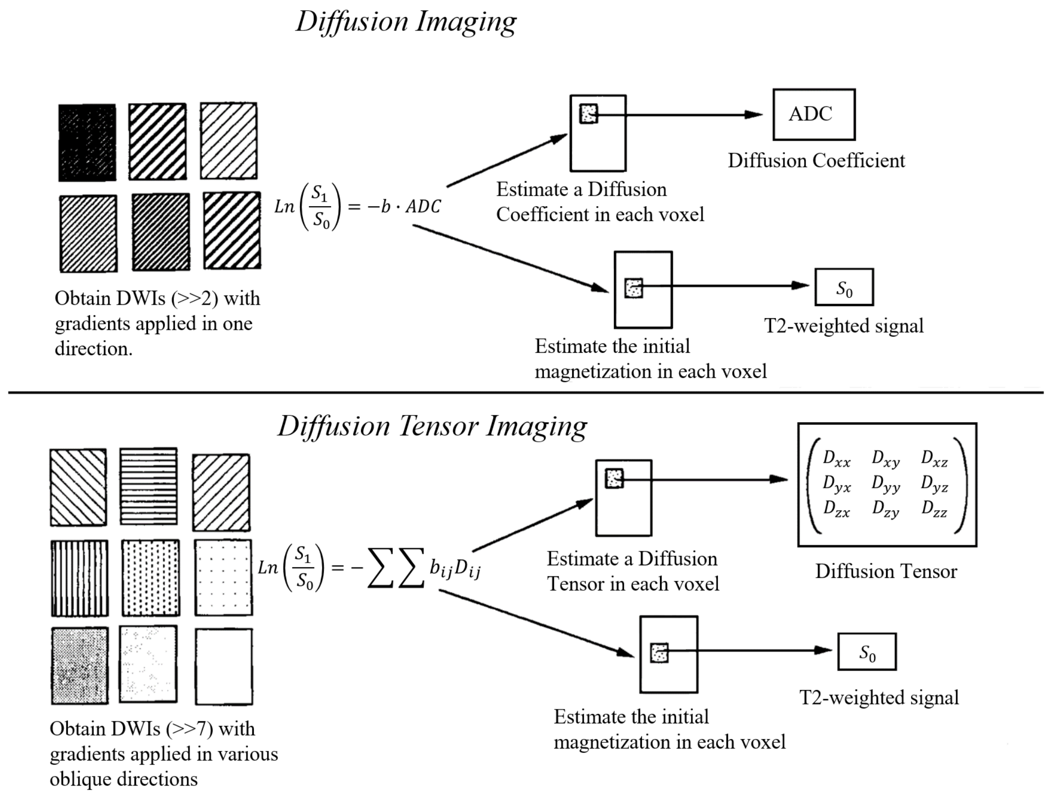

Figure 1.9: Comparison between DWI and DTI. In the manner that DWI estimates an ADC and a signal intensity value per voxel using two DWIs along one direction, DTI estimates a 3×3 diffusion tensor and a signal intensity value per voxel utilizing at least seven DWIs along non-collinear gradient directions. Figure from Peter J. Basser 1995 [28].

The diagonal tensor elements D_{xx}, D_{yy}, and D_{zz} correspond to the ADC values along the orthogonal axes x, y, z, respectively. In the case of isotropic diffusion, the diagonal elements not only equate to the ADC, but are additionally equivalent to each other (i.e. $D_{xx}=D_{yy}=D_{zz}=ADC$). Whenever the tensor is aligned completely along the principal directions x, y and z, the off-diagonal elements become zero. However, in anisotropic conditions where the principal direction of diffusion might not be aligned to the fixed axes but instead change from voxel to voxel, the off-diagonal elements do not have a straightforward significance. They do not indicate ADC values along oblique directions, but instead represent a covariance measure (or correlation of random displacements) between each pair of axes (i.e. xy, xz, yz) [29]. To define a more intuitive representation of the tensor independent of the tissue's fiber orientation, the diffusion ellipsoid model comes at hand [23].

In turn, the diffusion ellipsoid requires at least six parameters to fully represent the tensor, namely the orthogonal unit vectors $\boldsymbol{\varepsilon}_1$, $\boldsymbol{\varepsilon}_2$, and $\boldsymbol{\varepsilon}_3$ or *eigenvectors* (indicate orientation of the tensor, aka the principal directions of diffusion) and the corresponding magnitudes, the *eigenvalues* λ_1, λ_2, and λ_3 (denote the size and shape of the tensor, aka the amount of diffusion) (Figure 1.10).

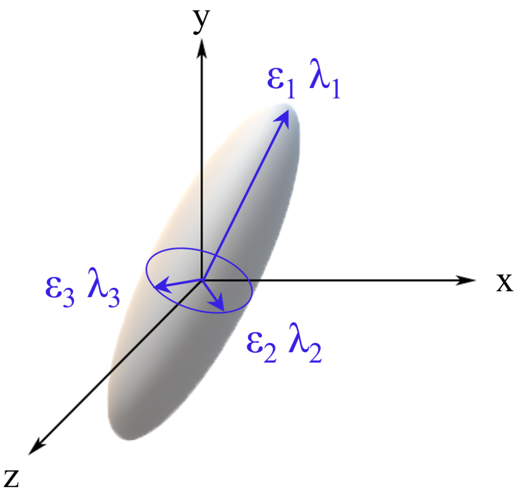

Figure 1.10: Diffusion ellipsoid. The tensor is represented by a diffusion ellipsoid, characterized by six elements: the perpendicular eigenvectors $\boldsymbol{\varepsilon}_1$, $\boldsymbol{\varepsilon}_2$, and $\boldsymbol{\varepsilon}_3$ that represent the principal orientation of the tensor, and the eigenvalues λ_1, λ_2, and λ_3 that denote the size and shape of the ellipsoid.

Mathematically, the diffusion tensor **D** can be rewritten in terms of the eigenvectors and eigenvalues by its multiplication with an eigenvector, resulting in the same eigenvector multiplied by the eigenvalue as of equation (1.10) [23]:

$$\mathbf{D}\varepsilon_i = \lambda_i \varepsilon_i \quad \text{for} \quad i = (1, 2, 3) \tag{1.10}$$

in matrix form:

$$\mathbf{D}E = \Lambda E \tag{1.11}$$

where E is the eigenvector matrix created by arranging the eigenvectors as column vectors, and Λ is the eigenvalue matrix. Since the eigenvectors are orthonormal –all three are unit vectors and mutually orthogonal– E shares the properties of a rotation matrix [30]:

$$E^{-1} = E^T \tag{1.12}$$

Therefore, equation (1.11) can be used to calculate the diffusion tensor **D**:

$$\mathbf{D} = E\Lambda E^T \tag{1.13}$$

Substituting equation (1.13) in matrix notation yields:

$$\mathbf{D} = \begin{bmatrix} \varepsilon_{1x} & \varepsilon_{2x} & \varepsilon_{3x} \\ \varepsilon_{1y} & \varepsilon_{2y} & \varepsilon_{3y} \\ \varepsilon_{1z} & \varepsilon_{2z} & \varepsilon_{3z} \end{bmatrix} \cdot \begin{bmatrix} \lambda_1 & 0 & 0 \\ 0 & \lambda_2 & 0 \\ 0 & 0 & \lambda_3 \end{bmatrix} \cdot \begin{bmatrix} \varepsilon_{1x} & \varepsilon_{1y} & \varepsilon_{1z} \\ \varepsilon_{2x} & \varepsilon_{2y} & \varepsilon_{2z} \\ \varepsilon_{3x} & \varepsilon_{3y} & \varepsilon_{3z} \end{bmatrix} = \begin{bmatrix} D_{xx} & D_{xy} & D_{xz} \\ D_{yx} & D_{yy} & D_{yz} \\ D_{zx} & D_{zy} & D_{zz} \end{bmatrix} \tag{1.14}$$

1.3.2 Key Diffusion Metrics

Equation (1.14) allows the interpretation of the diffusion tensor **D** as a 3 × 3 symmetric covariance matrix based on eigenvectors and eigenvalues that now directly represent the shape and size of the tensor as well as its orientation. Both eigenvectors and eigenvalues are paired (i.e. ε_1 with λ_1) and the eigenvalues specify the ADC estimates along the direction of the associated eigenvector.

Moreover, the eigenvalues are typically ordered from largest to smallest as $\lambda_1 \geq \lambda_2 \geq \lambda_3$, where the largest eigenvalue represents the principal direction of diffusion of the ellipsoid (since water molecules are coerced to move primarily along the fiber, $\boldsymbol{\varepsilon}_1$ indicates the local orientation of the tissue). The same eigenvalue λ_1 defines one of the core diffusion parameters, the axial diffusivity (AD) otherwise referred to as $\lambda_{\|}$, parallel, or longitudinal diffusivity:

$$AD = \lambda_1 = \lambda_{\|} = ADC_{\|} \tag{1.15}$$

Essentially, AD reflects the apparent diffusion ADC parallel to the tissue fibers. On the other hand, the apparent diffusion perpendicular to the main orientation of the fibers is characterized by radial diffusivity (RD), also termed perpendicular or transverse diffusivity, and is calculated from the smaller second (λ_2) and third (λ_3) eigenvalues:

$$RD = \frac{\lambda_2 + \lambda_3}{2} = \lambda_{\perp} = ADC_{\perp} \tag{1.16}$$

A metric that describes the global diffusion per voxel as a nondirectional measure is the mean diffusivity (MD) and is derived by taking the mean of the three eigenvalues, or performing a simple operation between the parallel and perpendicular ADCs:

$$MD = \frac{\lambda_1 + \lambda_2 + \lambda_3}{3} = \frac{Trace}{3} = \frac{ADC_{\|} + 2ADC_{\perp}}{3} \tag{1.17}$$

All three diffusion metrics AD, RD, and MD are usually set in units of mm^2/s. Fractional anisotropy (FA) is an additional central diffusion parameter; it is a scalar, unitless measure aimed to quantify the disparity level between parallel ($\lambda_{\|}$) and perpendicular ($\lambda_{\perp}$) diffusivities. In other words, FA encompasses the degree of anisotropy [28]:

$$FA = \sqrt{\frac{3}{2}}\sqrt{\frac{(\lambda_1 - MD)^2 + (\lambda_2 - MD)^2 + (\lambda_3 - MD)^2}{\lambda_1^2 + \lambda_2^2 + \lambda_3^2}} \tag{1.18}$$

and ranges between a value of 0 (isotropic) and 1 (anisotropic). Recall that for isotropic diffusion, the ADC values along the three orthogonal axes are equal (i.e. $\lambda_1 = \lambda_2 = \lambda_3$) and hence diffusion can be modeled as a sphere. As diffusion transitions to a more anisotropic condition, the eigenvalues become more dissimilar (i.e. $\lambda_{\parallel}$ increases to a greater extent compared to $\lambda_{\perp}$), causing a gradual uniaxial prolongation of the sphere towards the diffusion ellipsoid model (Figure 1.11).

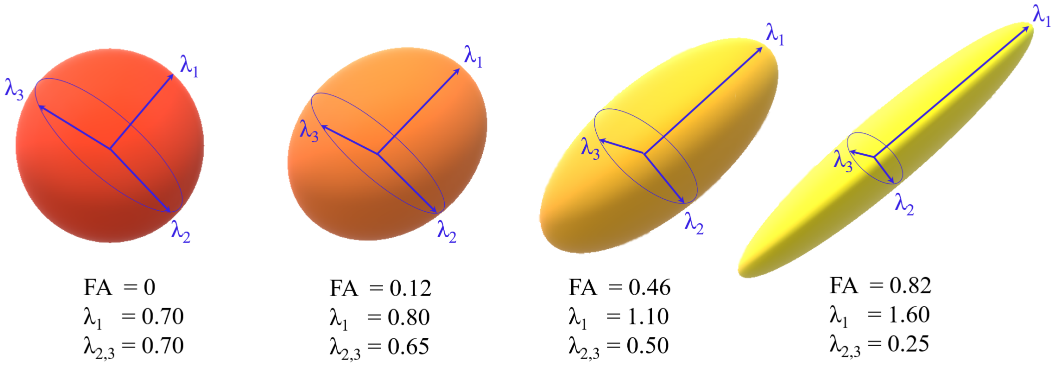

Figure 1.11: Transition from isotropic (low FA) to anisotropic (high FA) diffusion. An increment of axial diffusivity and/or a decrement of radial diffusivity cause an increase in FA, as they both move further from the mean. The four cases shown here maintain a constant MD at 0.7×10^{-3} mm^2/s. Axial and radial diffusivities are both in units of 10^{-3} mm^2/s. Adapted from Christian Beaulieu from *Diffusion MRI: From Quantitative Measurement to in Vivo Neuroanatomy*, Chapter 8, pg. 158 [31].

The estimation of the aforementioned diffusion parameters in each voxel allows the calculation of quantitative diffusion maps that reveal valuable tissue properties (i.e. they support the study of normal and abnormal conditions such as pathological restricted diffusion in ischemic stroke). Additionally, since the FA map outlines tissue with high anisotropy (shown as bright gray on a typical FA map), it delineates the underlying white matter tracts. On the contrary, the darker gray areas depict tissue with low anisotropy (i.e. isotropic diffusion such as in gray matter and CSF, or the case of crossing fibers). Figure 1.12 displays a standard map for axial, radial, and mean diffusivities (AD, RD, and MD, respectively), as well as for fractional anisotropy (FA).

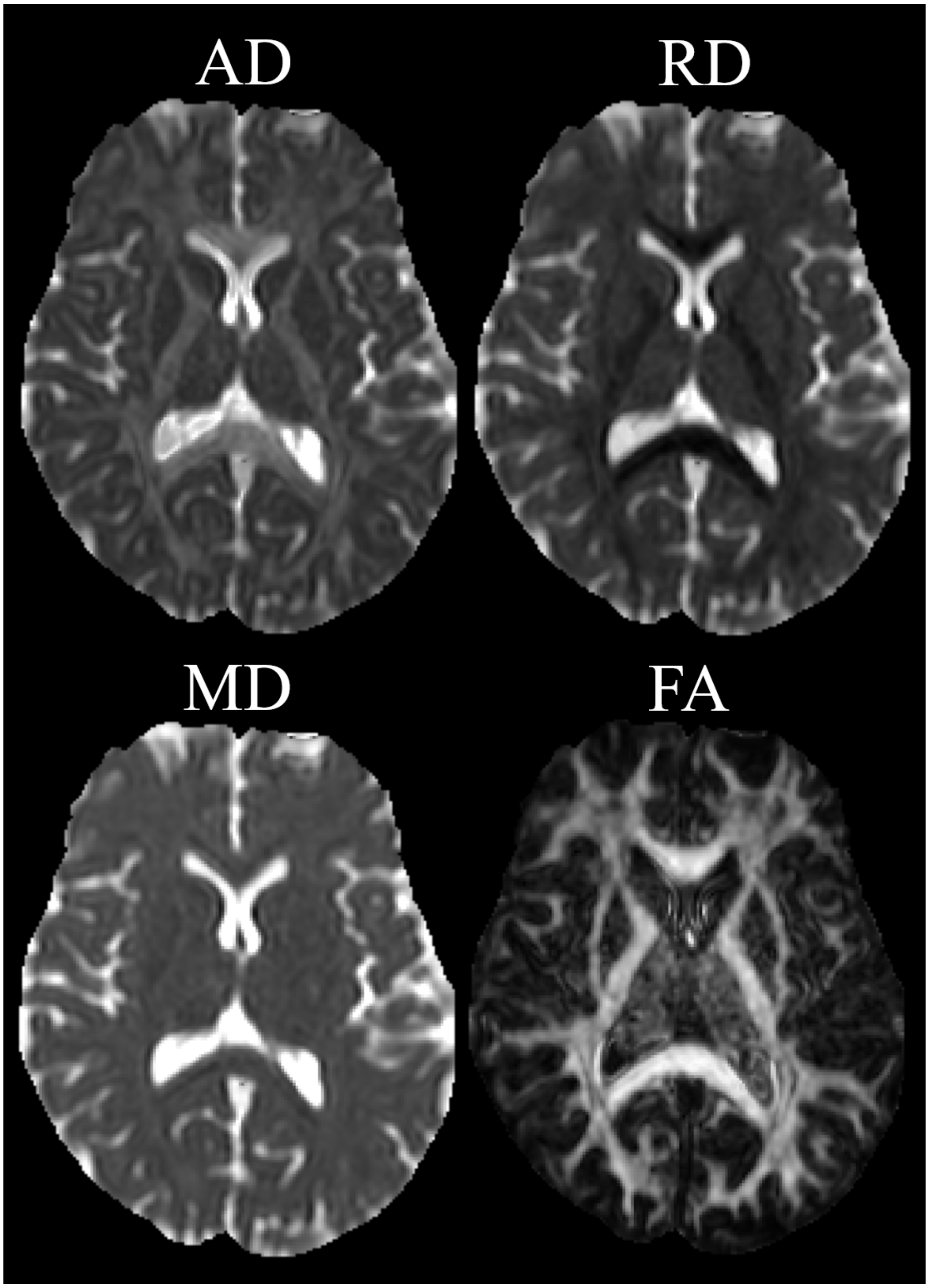

Figure 1.12: Diffusion maps. Standard maps for axial, radial and mean diffusivities (AD, RD, and MD, respectively) along with a fractional anisotropy (FA) map of a healthy subject. The bright signal (i.e. white) in the AD, RD and MD maps indicates a high amount of diffusion, as observed in the regions containing CSF such as the ventricles. The bright gray areas in the FA map depict a high degree of anisotropy, (i.e. white matter tracts), whereas areas of low anisotropy are shown in dark gray.

Furthermore, an informative color-coded FA map can be created that illustrates both water diffusion directionality and the amount of anisotropy. This calculation involves the multiplication of the FA map with a directionally-encoded color map produced from the first eigenvector of the tensor. By convention, tracts with a left-right orientation are colored in red, superior-inferiorly oriented tracts are colored blue, and finally white matter tracts extending anterior-posteriorly are colored green [32], as shown in Figure 1.13.

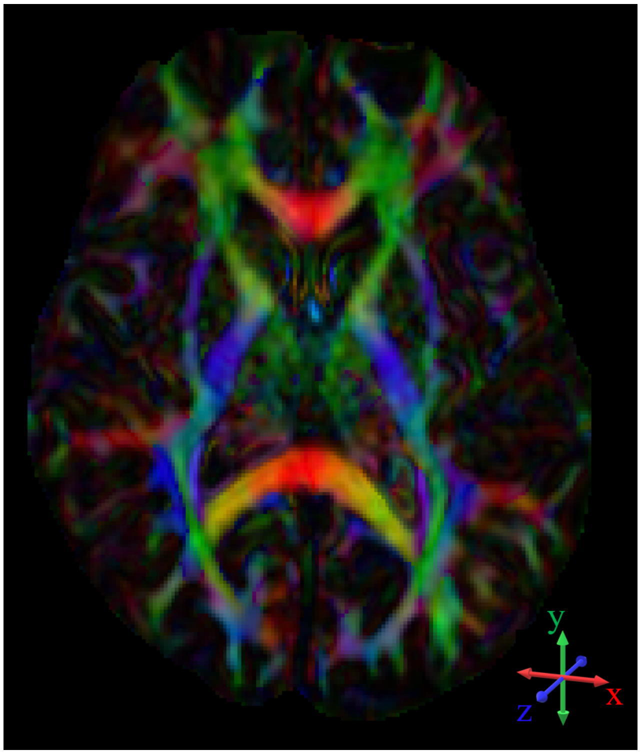

Figure 1.13: Color-coded FA map depicting the orientation of the white matter tracts in a healthy human brain. Red indicates left-right orientation, blue is superior-inferior, and green shows anterior-posterior direction.

1.3.3 DTI Data Analysis

Currently there are multiple approaches available to analyze DTI data, and the correct method to use will depend on the expected outcomes and the type of data acquired. A few of the standard approaches will be discussed in this section.

1.3.3.1 Fiber Tractography

Tractography emerged for the first time in 1999 when Susumu Mori and colleagues managed to track anisotropy-guided nerve fiber bundles in a fixed rat brain [33]. Subsequent, non-invasive *in vivo* human brain studies also accomplished neuronal fiber tracking through different mathematical algorithms that linked voxels based on the direction of the principal eigenvector by way of an FA threshold [34], seed points and termination points [35], and the Frenet equation which defined the evolution of the fiber tracts [36]. In general, tractography or fiber tracking is a technique that reconstructs an approximated 3D model of the white matter axonal pathways in the brain *in vivo*. However, it must be mentioned that it does not by any means constitute a replica of individual axons or yet a precise model of whole axon bundles, but simply a fair estimation of axonal fiber connectivity. Two tractography methodologies will be discussed.

Deterministic Tractography

Deterministic tractography, otherwise known as deterministic streamline tractography is a fiber tracking approach based on the step by step propagation of a single streamline per user-established source point or so-called *seed* point up to a termination point on the principal eigenvector field (Figure 1.14A) [37]. The streamlines are interconnected subject to the orientation of the first eigenvector of the diffusion tensor and a choice of interpolation method.

The adjacent-voxel interpolation approach is based on the pioneered fiber assignment by continuous tracking (FACT) algorithm and consists of the tracking of continuous vector fields from neighboring voxels to infer the pathway of the fiber, up until an unexpected discontinuity in fiber direction [33]. The tract termination guidelines involve specified thresholds such as a low FA (i.e. FA$<$0.2) that may implicate a transition to GM tissue or a large angle variation between succeeding steps [37].

Probabilistic Tractography

The probabilistic tractography method is not based on the orientation of the main eigenvector of the diffusion tensor like the affiliated deterministic approach, but rather estimates a probability distribution of potential tract orientations per voxel. It attempts to overcome the deterministic limitations by estimating a probability density function (PDF) that creates a distribution of the possible directions the track can undertake for each step of the algorithm, predicting several neural connections from each seed point (Figure 1.14B) [37]. In summary, probabilistic tractography does not reflect the physical connection of the white matter tracts, but merely calculates a probability distribution of tract orientations.

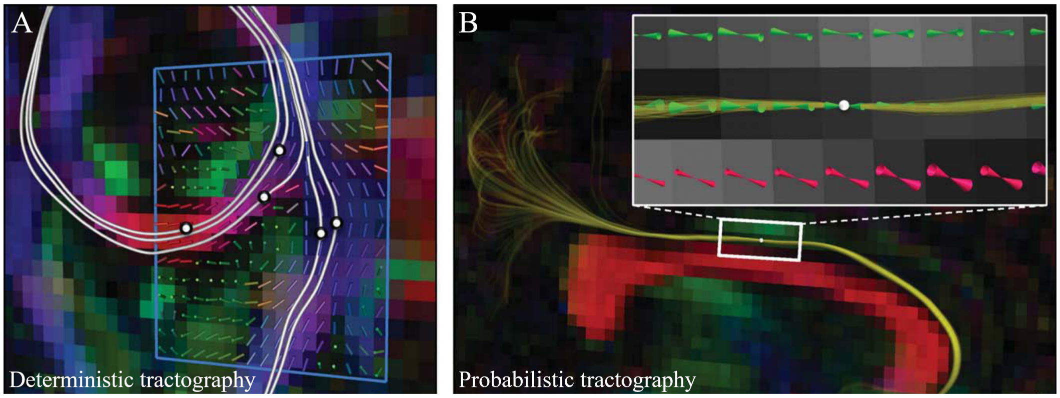

Figure 1.14: Deterministic vs probabilistic tractography. A) Deterministic tractography. Different seed points were placed across the genu of the corpus callosum (i.e. red area) and the corticospinal tract (i.e. blue area). Based on the direction of the principal eigenvector in each voxel, the algorithm bidirectionally propagated white streamlines that represent nerve fibers. B) Probabilistic tractography. Image depicts 1000 projections computed by the probability density function (PDF) originating from a single seed point, showing the user a broad map of possible tract orientations. Figure from Jacques-Donald Tournier et al. 2011 [37].

1.3.3.2 ROI Analysis

The region of interest (ROI) analysis consists of encircling a particular region on MR-acquired images to extract informative parameters from the selected voxels such as the mean, standard deviation, number of pixels, volume, etc.

The ROI should be drawn on images that facilitate the visual localization of the area under study, for instance T1 and T2-weighted images for overall structural organization, DWI and MD for stroke lesions, and FA and colored-FA for white matter tracts. In some cases, it may be helpful to make use of more than one image/map simultaneously to define an ROI, as long as the images are registered and all structures are perfectly aligned.

Examining a specific WM or GM structure through ROI analysis requires prior knowledge of the anatomy to accurately define its boundaries. For the case of lesions such as a stroke or tumor, however, a careful delineation of the affected area will suffice, and a contralateral ROI of healthy tissue can be traced to compare the acquired parameters. The ROI can be drawn either manually or via an automated segmentation method depending if the studied region is anatomic-specific (former and latter cases) or if it contains non-specific structures (i.e. lesions; former case). Additionally, ROIs can be placed in single or several slices to incorporate the entire structure and aim for a more robust measurement.

1.3.4 DTI Applications

One of the main drivers in current conducted research in the field of DTI is its potential to apply it in clinical settings. To this day and for the many reasons described in the next section, however, it is difficult to rely on the tool's accuracy of the brain's white matter pathway reconstructions. Nonetheless, due to its innate sensitivity to diffusion fluctuations, an assessment of microstructural organization can be achieved in both health and disease. A few of the most prominent DTI applications will be discussed.

To begin with, DTI has been predominantly used to non-invasively investigate white matter connections in the brain *in vivo*, such as to study normal brain development with aging [38–43]. These studies have allowed a better understanding of brain WM and even GM maturation over a lifespan, setting the basis for natural age-related diffusion changes. Secondly, white matter fiber tractography has opened new doors for surgical planning, both preoperatively [44] and intraoperatively [45, 46] aiming for higher precision of the image-guided removal of tumors while simultaneously prioritizing the preservation of undisturbed healthy tissue.

Third, DTI has played an important role in the diagnostics of brain lesions and disorders. Namely, it has been useful in the characterization of ischemic stroke, as the lesion depicts clear decreases in ADC and can be easily identified as a 'dark' region on an MD map [47–49]. Additionally, DTI has made possible the measurement of alterations and abnormalities in white matter organization in disease processes, specifically in Alzheimer's disease [50–52], multiple sclerosis [53–55], epilepsy [56], and Parkinson's disease [57, 58]. The focus of these investigations relies on identifying biological markers that can lead to a practical distinction between pathologies as well as in complementing clinical evaluations for a prompt non-invasive diagnosis.

1.3.5 DTI Limitations

Although a very revolutionary and valuable technique, DTI holds a number of limitations that cannot be ignored. To start, it stems from DWI which is confounded by low resolution (typically 2 – 3 mm), long scanning times (~5 – 10 min) partially due to the echo planar imaging (EPI) readout (discussed later in Chapter 2), low signal-to-noise ratio (SNR) – which is inversely proportional to the amount of diffusion weighting, – and high sensitivity to patient motion (therefore prone to artifacts). All previous factors are of great importance, as the quality of the acquired data has a direct influence on the correct estimation of the tensor.

The low-resolution aspect imposes a great amount of difficulty on the interpretation of the diffusion-derived measurements of microscopically organized structures that are averaged over a voxel because the acquired parameters can be misleading. That is, a voxel can contain multiple non-coherently oriented fibers and yield a low FA; however, a low anisotropy outcome is not necessarily realistic as diffusion in nerve fibers is highly anisotropic [17], yet these are not adequately aligned to aggregate their effect. In a similar manner, the cortex has shown a small degree of anisotropy of FA=0.2 [59] due to the arrangement of the smaller-scale axons and dendrites (compared to a typical FA≥0.5 in coherent white matter).

Similarly, if there are two or more WM crossing fibers within a voxel that have different directions, their averaged principal orientation will more likely fit the spherical tensor model and generate a low FA (that in this case does not translate to isotropic diffusion). Even if these two fibers happened to steer in similar directions and the voxel exhibited a high FA, the direction of the principal eigenvector of the diffusion tensor of that particular voxel would not accurately represent the microstructure underneath. In short, the DTI model cannot define more than one nerve fiber orientation per voxel and the user should never assume that the orientation of the first eigenvector represents the truthful orientation of the underlying fibers in that voxel unless the axons are perfectly coherently aligned [25]. Even when acquiring more than the minimum of six measurements along different non-collinear gradient directions, the diffusion tensor remains an eminently oversimplified, albeit useful, model of the intricate neural architecture.

Furthermore, although DTI is well suited to model free Gaussian diffusion it becomes inaccurate in restricted diffusion regimes such as in cellular compartments where water diffusion does not occur in a random fashion [25]. Additionally, DTI acquisitions are subject to long scanning times, for the most part due to the diffusion gradients pulses that prolong the echo time (TE) which in turn prolongs the repetition time (TR) for a given number of 2D slices. This is particularly troublesome in the clinical setting where the available scan time per patient is limited, and fast cost-efficient imaging and diagnostics are crucial. Moreover, DTI is incapable of distinguishing between efferent and afferent nerve fibers, as it can only characterize the trajectory of water molecular motion.

The aforementioned DTI caveats drive the ellipsoid tensor model to be commonly recognized as a less accurate method, and dubious to extrapolate to clinical applications. Nonetheless, many of the downsides can be corrected and/or ameliorated. For example, higher image resolution can improve the precision of the tensor, since smaller voxels are expected to contain less fiber populations (though decreasing SNR). Low SNR can be counteracted by acquiring more signal averages (extending scan time). A long scan time can be reduced by using single-shot echo-planar imaging (SS-EPI) that in fact has its own limitations (i.e. predisposed to B_0 susceptibility effects, eddy-current induced distortions and low spatial resolution), however these can be reduced by utilizing parallel imaging and partial Fourier to reduce the readout train in the acquisition [37].

As demonstrated, DTI can appear overwhelming with countless parameter combinations and approaches to be selected. Nevertheless, the possibility to adjust numerous variables can be seized as an advantage to optimize the imaging protocols and expand the limits of the technique.

1.4 Oscillating Gradient Spin Echo (OGSE)

1.4.1 Introduction

Recalling characteristic diffusion in white matter, water travels a distance of 8 μm during the typical PGSE diffusion time of $_{\text{eff}}= 40$ ms. Since myelinated axons in the central nervous system (CNS) have diameters that range between 0.2 – 10 μm [60], in 40 ms water molecules will long have encountered cellular barriers for any axon with a diameter below 8 μm (in essence the great majority). Consequently, the ADC will be reduced for both small and large axon diameters that fall under this particular caliber (Figure 1.15A). Imaging at such long diffusion times therefore elucidates only a small percentage of the microstructure's long-sought features and it becomes impossible to distinguish axon sizes since barriers are encountered in all cases.

If the MRI measurement was acquired in a much shorter diffusion time (i.e. $_{\text{eff}}$= 5 ms), water molecules would come across less boundaries and thus become less hindered over larger spatial scales such as in large axons, exhibiting an increase in ADC (Figure 1.15B). Hence, imaging within a smaller time frame can unmask spatial-dimension differences between small and large axons enabled by a measureable change in water diffusion with ADC. This scanning modality holds a promising standpoint to uncover smaller structural differences in nervous tissue that can lead to achieving a unique imaging contrast mechanism useful to study nerve cells both in healthy and pathological states.

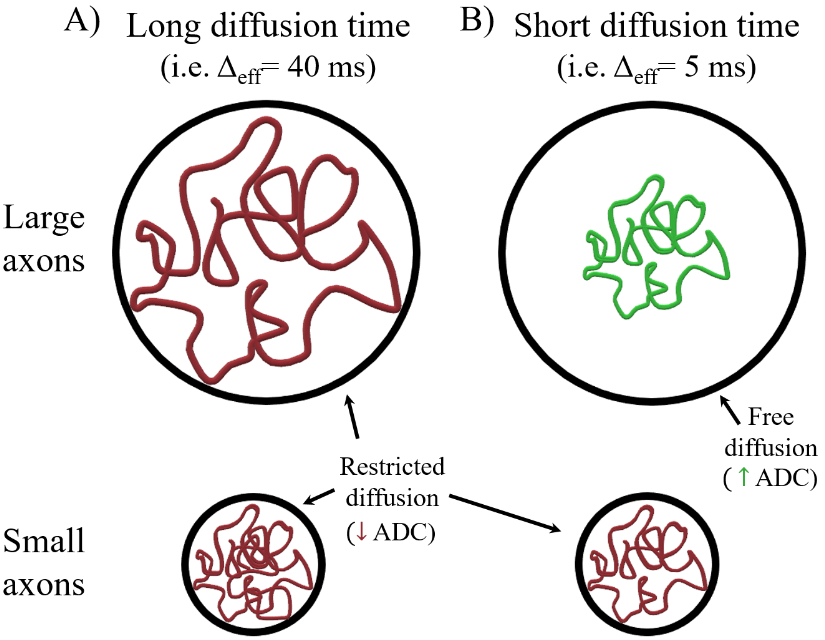

Figure 1.15: Diffusion time effects in microstructure differentiation. A) At long diffusion times (i.e. $_{\text{eff}}$= 40 ms), water molecules have enough time to come across cellular barriers in both large and small axons, indicating restricted diffusion due to a reduced ADC. B) Imaging at short diffusion times (i.e. $_{\text{eff}}$= 5 ms) only allows water to encounter barriers for smaller axons. In large axons, however, water remains unrestricted and features an increase in ADC.

Before the use of oscillating gradients, earlier studies using strong insert gradients observed diffusion-time effects on diffusion parameters in several animal models [61–64]. Nonetheless, the implementation of a shorter diffusion time with the standard PGSE diffusion imaging sequence has been particularly challenging. Revisiting the Stejskal-Tanner equation (1.3), in order to considerably decrease the diffusion time while maintaining a sufficient degree of diffusion weighting (i.e. b-value) one would need to image with much higher gradient amplitudes that are unattainable with current clinical MRI systems. Therefore, this strict unavoidable hardware limitation urges for the employment of an alternative approach to study short diffusion time effects in brain tissue.

The oscillating gradient spin echo (OGSE) diffusion sequence meets these requirements. Gross and Kosfeld first introduced the oscillating gradient methodology theoretically in 1969 [65]. More than a decade later, Stepisnik further advanced their work by conducting a frequency spectral analysis of different magnetic field gradients using a density matrix calculation, and together with Callaghan mathematically characterized the attenuated signal as [66, 67]:

$$S_1 = S_0 \exp\left(-\frac{1}{\pi}\int_0^{\infty} F(\omega)D(\omega)F(\omega)\,\mathrm{d}\omega\right) \tag{1.19}$$

where S_1 represents the signal after the application of the diffusion-weighted gradient, S_0 is the echo signal devoid of diffusion weighting, $D(\omega)$ is the tensor denoting the diffusion spectrum, and $F(\omega)$ is the frequency spectrum derived from the Fourier transform of the time integral of the gradient waveform [68, 69], defined as:

$$F(\omega) = \int_{-\infty}^{\infty} dt'\, e^{i\omega t'} \int_0^{t'} dt''\, \gamma g(t'') \tag{1.20}$$

where $g(t)$ is the amplitude of the diffusion sensitizing gradient and γ is the gyromagnetic ratio. The OGSE sequence replaces the two gradient pulses characteristic of PGSE with cosine gradients that encode water diffusion in tissue within the course of brief time intervals enabled by the frequency spectrum of the oscillations, as depicted in Figure 1.16.

Higher frequencies will accommodate microstructure sampling with shorter diffusion time periods (i.e. as oscillating frequencies increases, $_{\text{eff}}$

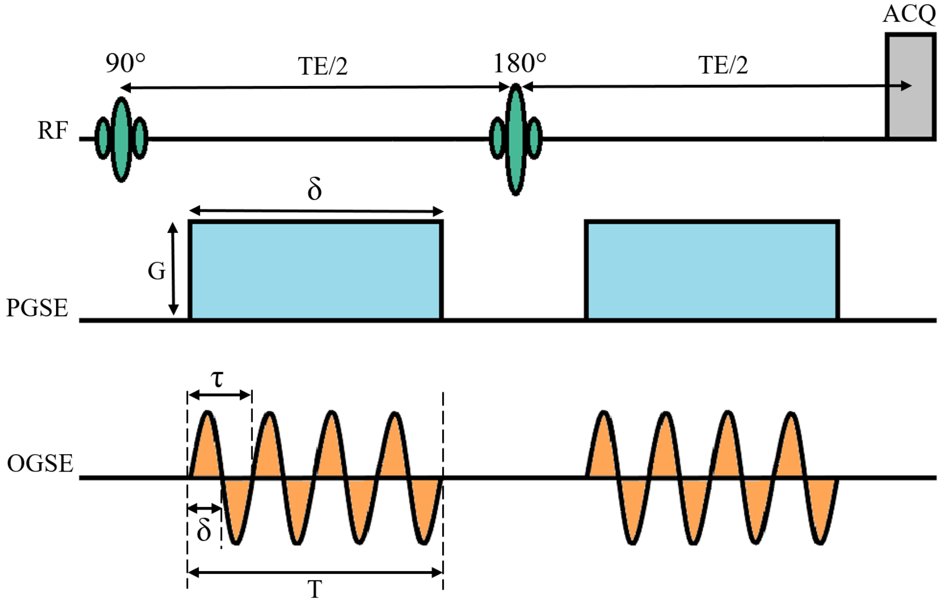

Figure 1.16: PGSE vs OGSE. Comparison of typical PGSE rectangular pulses (shown in blue) and the characteristic OGSE cosine waves (colored in orange). Both diffusion sequences measure water molecular motion during the $_{\text{eff}}$; however, due to the nature of the OGSE gradients, increasing their oscillation frequency allows to sample tissue during very short $_{\text{eff}}$ and therefore investigate shorter microstructural spatial scales.

decreases) [70–72]. However, the effective diffusion time and b-value calculation for OGSE sequences will vary depending on the type of sinusoidal waveform used (i.e. sine or cosine) and the number of periods per waveform, denoted by N. For a general sine-modulated OGSE waveform, the diffusion weighting is calculated as [69]:

$$b = \frac{3}{8}\left(\frac{\gamma G}{\pi N}\right)^2 T^3 \tag{1.21}$$

where T is the duration of the gradient waveform. Alternatively, for a standard apodized cosine-modulated OGSE waveform (i.e. apodized by replacing the start and end $\frac{1}{2}$ cosine lobes of each waveform with a complete sine lobe at double the frequency to smooth out the abrupt cosine pulse margins), the b-value resolves to [69]:

$$b = \frac{1}{8}\left(\frac{\gamma G}{\pi N}\right)^2 T^3\left(1 - \frac{1}{8N}\right) \tag{1.22}$$

Since the waveform duration is equivalent to $T= 2\pi N/\omega$ and $\omega= 2\pi/\tau$ where τ denotes the period, the effective diffusion time $_{\text{eff}}$ for a sine-modulated waveform can be calculated by rewriting equation (1.21) as [69]:

$$\Delta_{eff} = \frac{3}{8}\tau = \frac{3}{8f} \tag{1.23}$$

where f is the frequency of the oscillations. Similarly, for a cosine-modulated waveform [69]:

$$\Delta_{eff} = \frac{1}{4}\tau = \frac{1}{4f} \tag{1.24}$$

Equations (1.23) and (1.24) illustrate the inverse relationship between the effective diffusion time and the oscillation frequency of the gradients; hence, greater frequencies achieve shorter diffusion times. Utilizing cosine - modulated waveforms has its advantages over sine-modulated, as unlike PGSE and OGSE-sine, OGSE-cosine does not have its peak frequency at $f=$ 0 Hz and can therefore segregate the different frequencies. On the other hand, since PGSE is centered at 0 Hz, it masks the diffusion-time dependence of the ADC. [68, 72, 73]. Additionally, an even greater benefit can be observed when using trapezoid-cosine waveforms, since they produce a substantial increase in spectral amplitude which in turn allows for greater b-values [74] (Figure 1.17).

Having discussed the relevance of oscillating gradients, the next section will focus on reviewing previous OGSE applications, beginning with phantom studies and simulations, followed by pre-clinical and human studies.

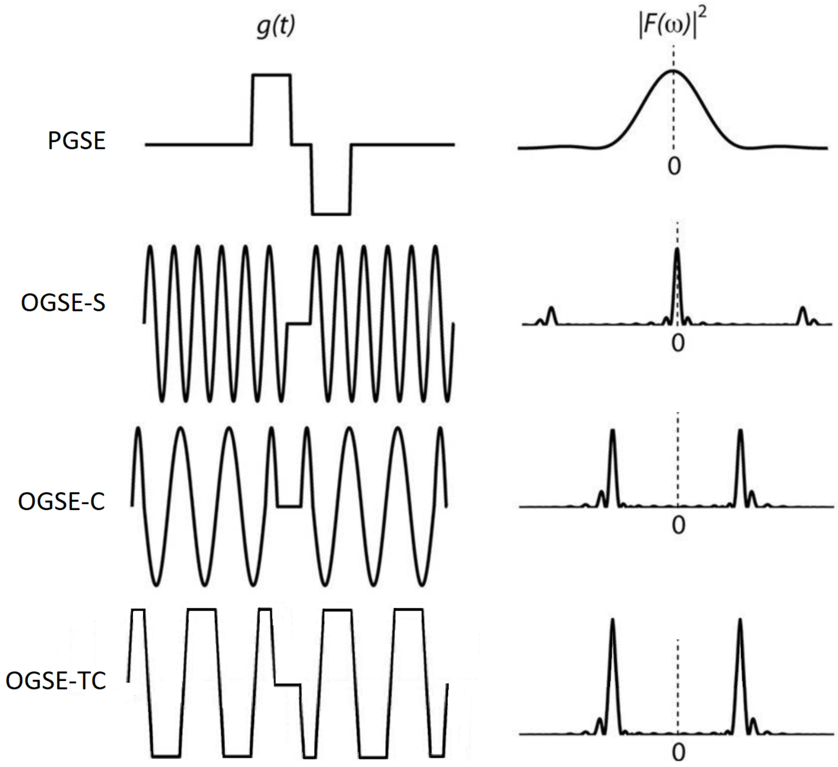

Figure 1.17: PGSE, OSGE-sine (OGSE-S), OGSE-cosine (OGSE-C), and OGSE trapezoid-cosine (OGSE-TC) waveforms (first column) shown alongside their diffusion gradient modulation spectrums (second column). Unlike PGSE and OGSE-sine, both OGSE-cosine waveforms do not have its frequency component centered at 0 Hz, which is key for OGSE diffusion-time experiments as it increases the specificity to discriminate between frequencies. Notice the spectral amplitude for OGSE-TC is considerably larger than OGSE-cosine. Adapted from Van et al., 2014. [73].

1.4.2 Previous OGSE Studies

1.4.2.1 Phantom Studies and Simulations

The first OGSE MRI experiment was conducted in 1995 on water saturated random packings of monodisperse glass spheres [75]. Since then, several OGSE experiments have been conducted to compare the effects of short diffusion times on the displacement of water for different levels of restriction. For instance, Schachter and collaborators analyzed OGSE-derived ADC values from five samples: one sample tube filled exclusively with water and the remaining four test tubes filled with water and closely packed polystyrene beads of a particular diameter each, namely of 2.8 μm, 9.1 μm, 25 μm, and

46 μm, for diffusion times ranging from ~5 ms to 30 ms (Figure 1.18) [76]. It can be observed in Figure 1.18 that at very short diffusion times (i.e. $_{\text{eff}}$=5 ms) the different-sized beads yield contrasting ADC values that allow them to be discriminated by their dimensions. On the other hand, at long diffusion times (i.e. $_{\text{eff}}$=30 ms) the diffusing water encounters more barriers and the ADC gap between different bead calibers becomes less apparent.

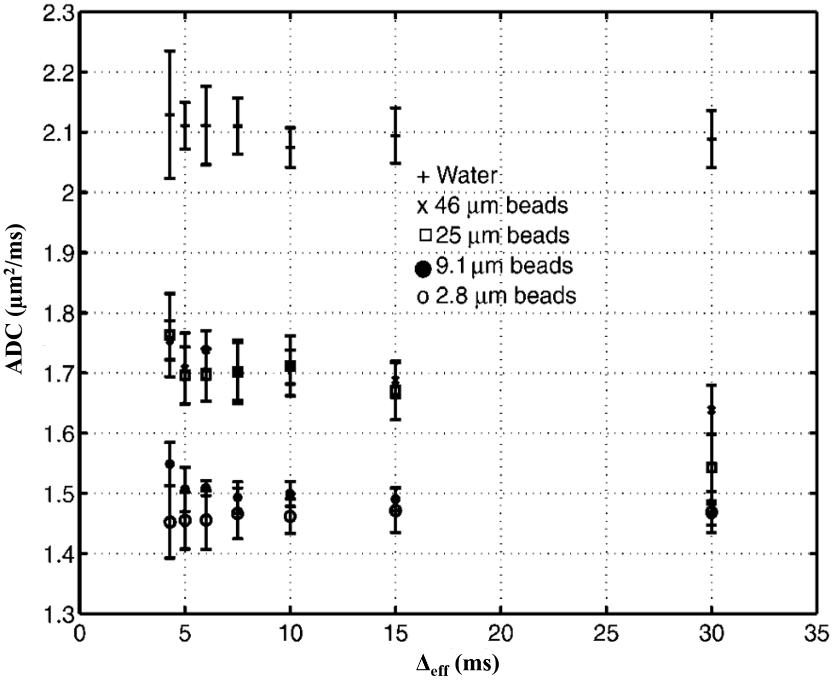

Figure 1.18: ADC variations as a function of diffusion time. Contrast in ADC values between five different samples for varied diffusion times. The sample tube with pure water features no restrictions to diffusion and therefore bears an ADC that remains consistent between diffusion times. Contrarily, the effects of diffusion time become apparent in the presence of hindrances; a distinct variation in ADC is observed for short diffusion times as opposed to a minimal ADC change for long diffusion times. Adapted from Schachter et al. 2000 [76].

Multiple additional OGSE models have been developed and simulated to study ADC changes as a function of the gradient oscillation frequency. A summary of four studies is depicted in Figure 1.19, where the models shown represent A) diffusion between two impermeable parallel planes with different levels of separation [72]; B) diffusion in spheres of different diameters [72]; C) diffusion in an array of non-permeable infinitely long cylinders [72, 77]; and D) diffusion in closed-packed spherical cells [72, 77].

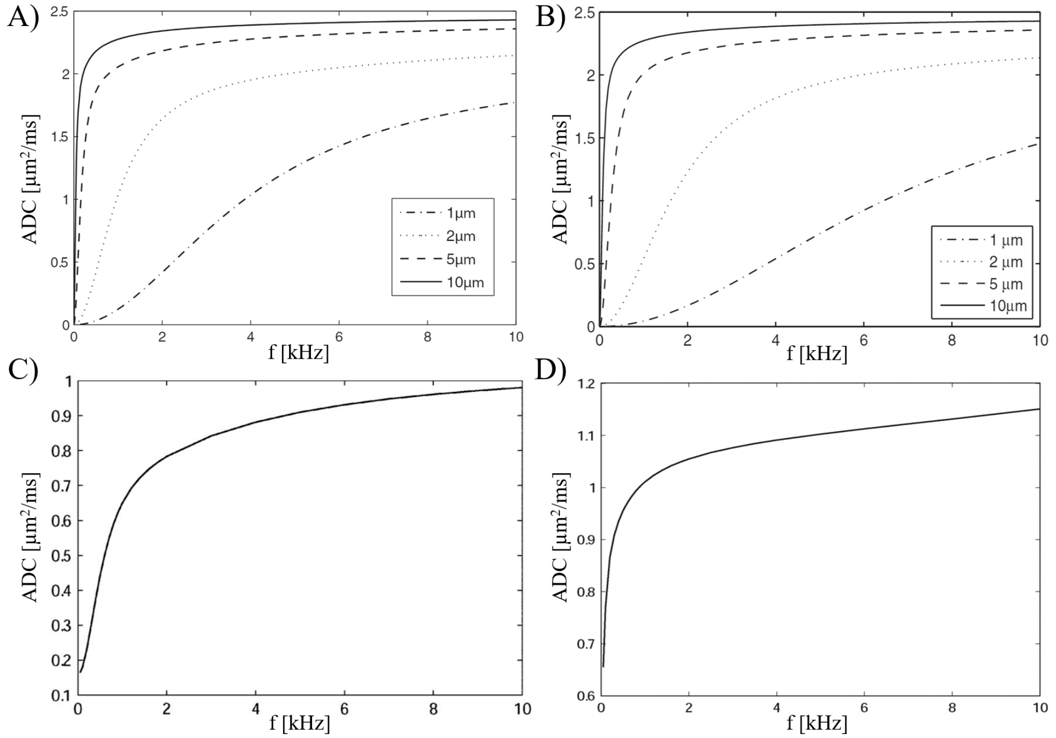

Figure 1.19: ADC variations as a function of frequency. OGSE models depicting calculated ADC dependence on oscillation frequency for A) diffusion between two infinite impermeable planes of varied separations, B) restricted diffusion in spheres of varied diameters, C) diffusion in an array of impermeable infinitely long cylinders, and D) diffusion in closely packed compartmentalized spherical cells. Note that these simulations were conducted on a scale of frequencies up to 10 kHz. Adapted from Gore et al [72].

The key takeaway from Figure 1.19A, B, lies in the clear ADC differentiation that can be made between different-sized structures with increasing frequency, especially between the smallest and largest cellular frameworks (although requiring considerably high frequencies up to 10 kHz as shown here). This valuable feature is capable of creating fine image contrast in MD maps to highlight distinct regions. Figure 1.19 B, C, shows a clear ADC increase with increasing frequencies for both simulations as water has less time to probe its environment and comes across less obstacles. Another simulation study of a white matter model with nonpermeable cylinders found that OGSE provides higher sensitivity than PGSE to investigate deeper into smaller axonal configurations [78].

ADC variations in diverse models with oscillating gradients have therefore proven to be a promising tool to explore microstructural spatial scale differences in biological tissue to ultimately infer important brain cell characteristics such as size, tortuosity, and surface-to-volume ratios [76].

1.4.2.2 Animal Studies

Numerous animal studies implementing the OGSE sequence have been acquired in the past years to investigate diffusion time-dependence properties of tissue, some of which are summarized in Table 1.1 organized by author and year of publication, specifying frequency of oscillation, diffusion times attained (shown only for oscillating gradients to correspond with alongside frequencies), and a brief summary of the work.

In agreement with the aforementioned simulations, animal studies with oscillating gradients found overall significant ADC increments as $_{\mathrm{eff}}$ was reduced [68, 79–88]. In fact, one of the studies showed greater ADC changes with increasing frequencies in rat spinal cord regions where histology indicates larger axons, suggesting that diffusion time differences and axon calibers are related [86]. Additionally, tensor eigenvalue increases concurrent with a decrease in FA were observed, as compared to imaging with the conventional PGSE sequence. As per some cases, the difference between these diffusion metrics can create an advantageous source of contrast from different cell types, such as seen for specific layers of the cerebellum and hippocampus [81, 85]. These studies covered an investigation of GM and WM of mice/rat brains in health, disease (i.e. tumor treatment response), and after the onset of stroke.

Table 1.1: Summary of previous OGSE animal studies.

Paper	**f (Hz)**	$_{\mathrm{eff}}$ **(ms)**	**Core Finding**
Does et al., 2003 [68]	-	9.75–0.375	Normal and globally ischemic rat brain study of GM showed an ADC increase up to 24% *in vivo* and 50% postmortem subject to the oscillating waveform used.
Colvin et al., 2008 [79]	30–240	$\sim 8.3 - 1$	*In vivo* OGSE rat brain imaging showed greater contrast between tumor and healthy tissue with increasing frequency (48% increase in ADC at 240 Hz) as compared to the PGSE method.
Colvin et al., 2011 [80]	120, 240	$\sim 2.1, 1$	An improved method for imaging gliomas in rat brain using oscillating gradients allowed the detection of tumor changes after treatment as early as 24 h.
Aggarwal et al., 2012 [81]	50, 100, 150	5, 2.5, 1.67	OGSE imaging of fixed mouse brain depicted enhanced contrast in specific cell layers of the cerebellum and hippocampus with increasing oscillation frequency (ADC, $\lambda_{\perp}$, and $\lambda_{\parallel}$ increased while FA decreased).
Kershaw et al., 2013 [82]	33.3–133.3	7.5–1.88	*In vivo* rat brain imaging using oscillating gradients showed significant increases of MD and the eigenvalues for cerebellar GM and WM regions, additional to a significant decrease of FA in WM.
Portnoy et al., 2013 [83]	67-1000	3.75–0.25	A magnetic resonance microscopy study was conducted on a rat hippocampal specimen with similar $_{\mathrm{eff}}$ for both PGSE and OGSE, which at low b-values yielded comparable ADCs that later diverged at high b-values.
Pyatigorskaya et al., 2014 [84]	64.5, 129	3.8, 1.9	OGSE *in vivo* imaging of healthy rat brain cortex concluded that even at the shortest diffusion time studied ($_{\mathrm{eff}}$= 1.25 ms), diffusion was not free.
Wu et al., 2014 [85]	50, 100 150, 200	5–1.25	*In vivo* and *ex vivo* OGSE imaging of normal and hypoxia-ischemic mice brains showed frequency-dependent ADC increments in the cortex and hippocampus, as well as improved ADC contrast between specific cell layers in cerebellum at f>100 Hz.
Xu et al., 2014 [86]	50–250	5–1	Temporal diffusion spectroscopy study of rat spinal WM tracts described histology-validated models to map mean axon diameters and intra-axonal volume fractions, showing ADC/frequency dependencies in regions with large axons.
Wu et al., 2017 [87]	50–300	5–0.83	*In vivo* healthy mice brain imaging study with oscillating gradients detected microcirculatory flow effects on diffusion measurements acquired at low b-values. An alternate method to suppress the effects is proposed.
Bongers et al., 2018 [88]	200	1.25	OGSE imaging of mice glioblastoma showed 30%-50% ADC increase compared to surrounding WM; during radiation treatment, a $\sim$ 15% ADC increase was also observed in the tumor.

1.4.2.3 Human Studies

Only a few OGSE human brain studies have been published to this day, which comes as no surprise considering the ineluctable hardware restraints posed by human scanners. A summary of the work is described in Table 1.2 (showing diffusion times for OGSE alone, to correspond with oscillation frequency).

Table 1.2: Summary of previous OGSE human studies.

Article	**B_0 (T)**	***b*-value (s/mm^2)**	**f (Hz)**	**$_{\text{eff}}$ (ms)**	**Core Finding**
Van et al., 2014 [73]	3	200	18, 44, 63	12, 6, 4	First study to implement the OGSE sequence for healthy human brain applications. Reported frequency-dependent ADC increase in the genu and splenium of the corpus callosum using an optimized trapezoid-cosine waveform.
Baron et al., 2014 [74]	4.7	300	20, 50	7.4, 4.1	First healthy human brain DTI study using oscillating gradients found significant increases of $\lambda_\perp$ and $\lambda_\parallel$ in 7 WM regions (up to 40% and 20%, respectively), additional to FA decreases, all at $_{\text{eff}}$=4.1 ms compared to the PGSE $_{\text{eff}}$=40 ms.
Baron et al., 2015 [48]	4.7	300	50	4.1	OGSE diffusion-encoding was used to image ischemic stroke patients for the first time. On average, WM stroke lesions showed an MD decrease of 37% for PGSE compared to only 8% for OGSE. The study provides insight into WM microstructural behavior after stroke.
Xu et al., 2016 [89]	3	400	20, 40	12.5-6.25	Study of the healthy human corpus callosum showed that the diffusion dispersion rate perpendicular to axon bundles ($DDR_\perp$) correlated well with the mean axon diameter (AxD) whereas the diffusion coefficient ($D_\perp$) didn't, indicating that $DDR_\perp$ is a potential indicator of mean AxD in human imaging.
Boonrod et al., 2018 [90]	3	1000	-	6.5-35.2	Stroke study on brain and brain stem reported four lesions with reduced visualization of the infarctions on DWI with the shorter $_{\text{eff}}$.
Iima et al., 2018 [91]	3	700	50	4.3	Study demonstrated that a measurable ADC-diffusion-time dependence was useful to distinguish malignant from benign head and neck tumors.
Maekawa et al., 2019 [92]	3	1000	30	6.5	Choroid plexus cysts yielded higher ADC values at the shorter $_{\text{eff}}$=6.5 ms (OGSE) vs $_{\text{eff}}$=35.2 ms (PGSE), but also showed lower ADC values compared to those in CSF with $_{\text{eff}}$ of 35.2 ms and 6.5 ms.
Arbabi et al., 2019 [93]	7	450	30, 45, 60	-	Demonstrated evidence of linear dependence of ADC on the square root of OGSE frequency in healthy human WM and enabled full-brain maps of the apparent diffusion dispersion rate.

Further OGSE human brain studies are required, even more so at higher frequencies. However, the OGSE implementation for human applications is not straightforward. A deeper analysis of the encountered limitations will be further discussed in the section below.

1.4.3 OGSE Limitations in Human Brain Applications

Any MRI protocol is directly limited by the specifications of the imaging hardware. For the case of human brain applications, the available technology and hardware capabilities are far more restricting than that in animal scanners. Due to the compact size of animal scanner systems, they can be designed to have a far greater field strength and gradient amplitudes that allow an incredible high resolution and image quality, and greater diffusion sensitivity with a minimum TE.

Nonetheless, one of the greatest limiting parameters for OGSE acquisitions is the maximum gradient strength. First, in order to achieve very short $_{\text{eff}}$ diffusion times while simultaneously preserving a constant b-value one would need to increase either the gradient strength G or the number of cycles per waveform N. Since the former is subject to hardware constraints, augmenting the latter would increase TE resulting in an overall SNR loss and also elongate the total acquisition time (TA). An SNR loss could be compensated either by increasing the number of excitations (NEX) (however further extending TA) or by decreasing the resolution. Nevertheless, none of the previous possibilities is optimal. Additionally, accommodating a long TE generates heavily T2-weighted images with high CSF signal that cause Gibbs ringing (GR) artifacts and partial volume effects. Yet, bound by the maximum gradient amplitudes on scanner systems in the clinical (or even research) setting, the only course of action remains to settle for a long TE and TA or to settle with a lower b-value.

A recent publication discussed the advantages of microstructure imaging on a human MRI system with high gradient strengths of 300 mT/m, applicable for axon diameter distribution mapping, microstructural parameter estimation, and cancer/tumor imaging treatment response, among others, that in general enabled a higher SNR and shorter TE for a given b-value [94]. The article debates that the benefit of using such high gradient amplitudes with OGSE remains only on the possibility to achieve higher b-values for lower frequencies, and not as much on potentiating towards higher frequencies.

Table 1.3 depicts a comparison between an animal scanner and the limiting features of a typical human MRI system. Note that the much stronger magnetic field strength and gradient amplitudes achieved by the animal system maintain a short TE for a given b-value, in addition to allowing shorter effective diffusion times and a higher resolution for this example.

Table 1.3: Comparison between an animal scanner and our current 3T Siemens Prisma. The estimates on the human Prisma system arise from our available OGSE sequence in the advanced diffusion WIP and are stated for one b-value alone, not suggesting any ideal settings.

	Animal Scanner [81]	**Human Scanner**
Field strength	11.7 T	3 T
Max Gradient	1000 mT/m	80 mT/m
Slew rate	-	200 T/m/s
TE at b= 700 s/mm^2	50 ms (f=150 Hz; $_{\text{eff}}$= 1.67 ms)	144 ms (f=50 Hz; $_{\text{eff}}$= 4.3 ms) 529 ms (f~100 Hz; $_{\text{eff}}$= 2.6 ms)
Resolution	78 μm × 78 μm	1.72 mm × 1.72 mm

In summary, the principal advantage of imaging with oscillating gradients remains that the OGSE acquisition method (although challenging to apply in human brain) achieves shorter effective diffusion times than its counterpart, the conventional PGSE diffusion imaging sequence.

2 Overview of Methodology and Preliminary OGSE Experiments at 3T

2.1 Introduction

As mentioned in Chapter 1, there are currently as little as four OGSE studies in healthy human brain, one of which was conducted by a former student from our lab here in University of Alberta, using a 4.7T MRI system [74]. The aim of the following studies in this chapter focuses on the implementation and base testing of OGSE on our 3T Siemens Prisma and evaluating the options for expanding previous findings. One goal was to explore higher frequencies (most wanted to achieve very short diffusion times) and higher b-values (i.e. >300 s/mm^2). These experiments were collected on a 3T MAGNETOM Prisma scanner with high-amplitude gradients (maximum of 80 mT/m) using a 64-channel head coil (Siemens Healthcare, Erlangen, Germany) and a prototype 2D ss-EPI sequence (Advanced Diffusion WIP 918 & 919C). Note that the primary novel experiment and results are presented in Chapter 3.

A numerous amount of scanning parameters come into play when designing the imaging protocols. The MRI scanner allows certain degrees of freedom in the choice of TE, TR, NEX (i.e. signal averages), field of view (FOV), voxel size and slice thickness (i.e. resolution), b-value, inter-slice gap, gradient encoding directions, phase partial Fourier, parallel imaging technique and acceleration factor, interpolation, among others.

Given the great number of possible parameter arrangements, the primary objective was to find a balance between them to acquire OGSE data at the highest frequency that allowed good image quality, resolution, adequate SNR, and a large b-value, whilst maintaining TE and TA as short as possible. In the paragraphs below, the choice of some parameters for the experimental acquisitions is discussed.

b-value

High b-values allow greater precision and detail in the modeling of white matter tracts, since the sequence becomes more sensitive to the diffusion of water molecules and can better characterize their displacement, even more so for smaller structures. However, scanning at greater b-values has a drawback: it is accompanied by an increased signal decay (i.e. SNR loss), and overcoming this disadvantage will likely affect other parameter selections such as voxel size or NEX. Additionally, higher b-values increase the TE when the gradient amplitude has reached its maximum, since the gradient will need to be applied for a longer time to achieve the specified diffusion weighting (i.e. b-value), thereby further decreasing SNR. Therefore, there is a cumulative effect of b and TE - as will be shown in the next section. Nonetheless, the experimental acquisitions in this chapter aim to balance SNR limitations at higher b-values to explore the feasibility of $b \geq 400$ s/mm^2.

Gradient encoding directions

It is well known that acquiring more than six gradient directions provides additional information for the calculation of the diffusion tensor, making the estimation less susceptible to errors [27]. The use of >6 directions like 20 or 30 results in all three gradients being applied simultaneously and penalizes the OGSE acquisition with a longer TE for a given b-value. To provide evidence in regards to the previous argument, an OGSE FLAIR (discussion of FLAIR coupled with DTI later) experimental study was acquired comparing two different setups: (1) 6 gradient directions with 3 signal averages (i.e. 18 diffusion-weighted images), and (2) 20 gradient directions with 1 signal average (i.e. 20 diffusion-weighted images); all other parameters were kept consistent between scans (Figure 2.1).

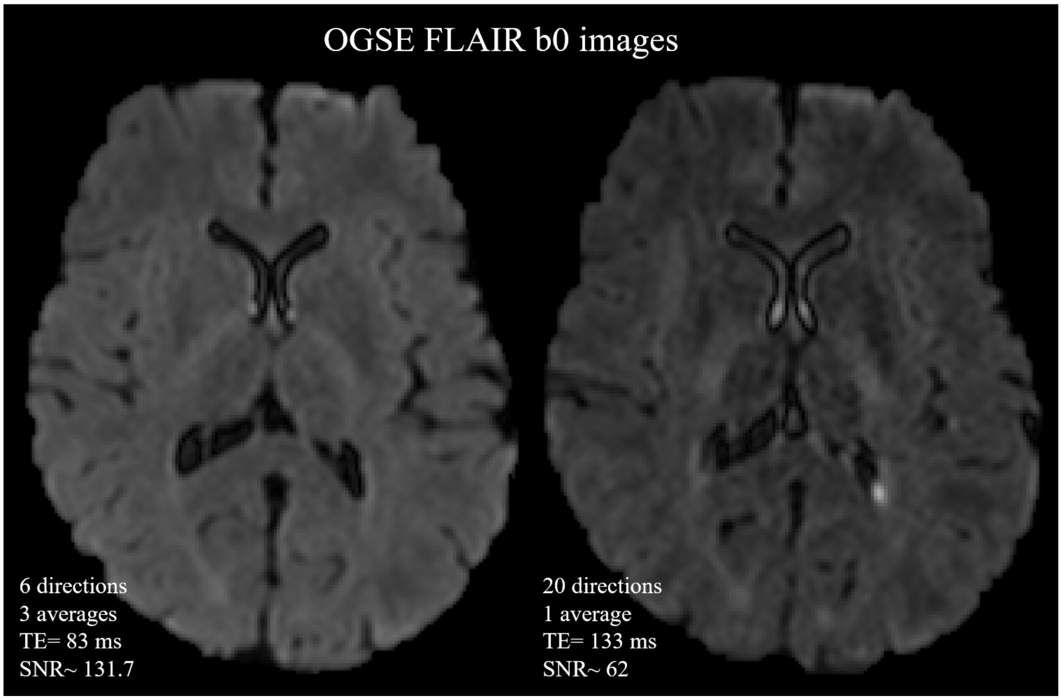

Figure 2.1: Comparison between acquisitions of 6 and 20 directions. OGSE FLAIR non-diffusion weighted b0s (both shown for a single signal average): acquired at 6 directions and 3 averages, yielding a TE= 83 ms and SNR~131.7 (left) and acquired at 20 directions and 1 average, yielding a TE=133 ms and SNR~62 (right). From visual inspection, it is evident that the TE increment of the image on the right caused a substantial signal decay and therefore SNR loss.

The effect of the application of all three gradients gradients in scenario (2) increased the TE by 50 ms from TE= 83 ms to 133 ms. The lengthening of the TE subsequently provoked a substantial SNR loss from SNR~131.7 to 62 (both measured from the first b0 image as the mean signal in brain tissue divided by the standard deviation of the background noise). In summary and for the particular purposes of these studies, trading a 6-direction scan for a 20-direction scan is nonviable due to the considerable TE increment and the more than two-fold SNR loss.

SS-EPI and Parallel Imaging

Since DWI measures displacements it is sensitive to subject motion. It is imperative that the imaging acquisition technique acquires fast high-quality data while simultaneously being able to acquire all the images needed in the lengthy DWI protocol. The single-shot echo planar imaging (SS-EPI) sequence meets these requirements by acquiring all k-space data after a single RF excitation, hence reducing total scanning time and sensitivity to motion. As a result, most DWI/DTI investigations use SS-EPI, and as such it was also the preferred method for all conducted experiments in this thesis.

However, like all modalities, SS-EPI has a number of disadvantages: it is prone to image distortions from eddy currents induced by the rapid switching of the gradients and B_0 susceptibility effects, low spatial resolution, and blurring due to the T2* decay during the prolonged image readout. Fortunately, parallel imaging techniques can be used in conjunction with SS-EPI to reduce susceptibility artifacts and the echo time (TE), thereby reducing the total acquisition time. The parallel imaging technique used here for all acquired experiments, Generalized Autocalibrating Partially Parallel Acquisitions (GRAPPA), collected under-sampled k-space data in the phase-encoding direction in order to accelerate the acquisition, as specified by the acceleration factor R. For all scans, an acceleration factor of $R = 2$ was employed.

2.2 Feasibility of OGSE Protocol

Having set the basis of important parameter considerations, an MRI protocol was designed to test the feasibility of OGSE acquisitions on our 3T Siemens Prisma. More specifically, the use of different b-values and OGSE frequencies is investigated for their effect on the acquisition parameters such as TR and TE, and to then estimate the expected signal loss, as will be discussed in the following sections.

2.2.1 OGSE Experimental Protocol

The protocol consisted of OGSE and PGSE DTI with: partial Fourier at 75%, GRAPPA R=2, 10 slices of 2.5 mm isotropic voxels (no gap), 1 signal average, FOV 220 mm, 88×72 acquisition matrix, and 6 diffusion encoding directions (optimal for shortest TE and highest b-value) with a total scan time of 30 min. Different b-values ranging from $b=$ 200-700 s/mm^2 were set at different OGSE frequencies depending on the maximum acceptable frequency allowed for each b-value, starting from 40 Hz. The frequency dictated the minimum TE and repetition time (TR) for each acquisition. Table 2.1 summarizes the protocol parameters for $b=$ 400-500 s/mm^2 at varying frequencies. The estimated percentage of residual WM signal after an acquisition is also shown assuming a T2 in frontal white matter of T2$_{\text{WM}}=$ 58 ms at 3T [95]. Notice how as frequencies are increased, the TE increases substantially leading to a significant signal loss, such as seen at higher frequencies of $f=$ 70 - 90 Hz. Therefore, these frequencies remain infeasible for OGSE acquisitions with current hardware.

Table 2.1: OGSE protocol describing acquisition parameters for $b=$ 400 s/mm^2 and $b=$ 500 s/mm^2. The estimated percentage of remaining signal in WM relative to tissue is shown (assuming a T2$_{\text{WM}}=$ 58 ms, but not accounting for diffusion effects). Note that the TR shown is for 10 slices only; a much longer TR would be needed for a full-brain acquisition. Moreover, although there was no change in TE for $f=$ 40 Hz and 50 Hz across both b-values, the TR increased, possibly due to high duty cycles from the oscillating gradients.

OGSE		b-value= 400 s/mm^2			b-value= 500 s/mm^2		
f (Hz)	$_{\textbf{eff}}$ **(ms)**	**TR (ms)**	**TE (ms)**	**WM signal**	**TR (ms)**	**TE (ms)**	**WM signal**
40	5.1	2200	73*	28%	2700	73*	28%
50	4.3	3300	101*	18%	4100	101*	18%
60	3.7	4700	127	11%	5800	161	6%
70	3.3	6200	168	6%	7700	196	3%
80	2.9	8000	219	2%	10000	269	1%
90	2.7	10100	286	1%			

* TE remained the same between b=400-500 s/mm^2 because the gradients had not reached their maximum strength limit.

Figure 2.2 shows a bar graph of the minimum OGSE TE values obtained at different *b*-values and oscillation frequencies. It can be observed that as both the *b*-values and frequencies were increased, the TE also increased considerably. In fact, the echo times at $f=$ 80, 90, and 100 Hz at high *b*-values of $b=$ 600 – 700 s/mm^2 became too large to be considered. Even at 70 Hz for $b=$ 500 s/mm^2, the TE came to be ~200 ms. Assuming the $T2_{WM}=$ 58 ms, such an unreasonably long echo time would cause an immense signal intensity reduction, down to an estimated ~3% (considering that the average SNR in the diffusion weighted image is usually around 30% of that in the non-diffusion weighted b0 [25]). Hence, any data acquired around these values would be deemed impractical and no useful information could be derived from it. Evidently, OGSE acquisitions become very challenging at short diffusion times.

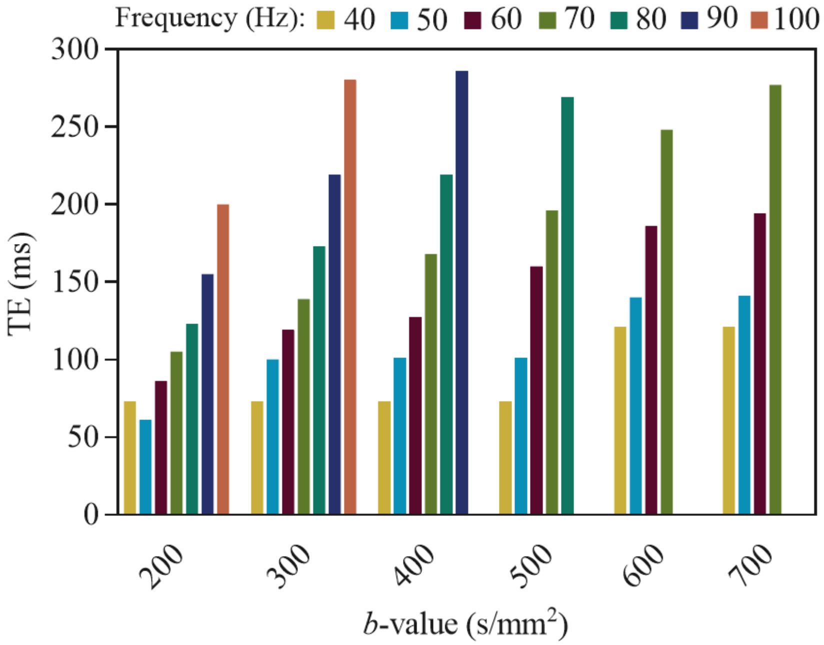

Figure 2.2: OGSE TE values as a function of *b*-value. Bar graph depicting minimum TE values obtained as a result of increasing OGSE frequencies at varying *b*-values. The TE for higher frequencies, namely TE at f=100 Hz for *b*400, f=90-100 Hz for *b*500, f=80-100 Hz for *b*600, and f=80-100 Hz for *b*700 were infeasible, therefore they were not included in this depiction.

2.3 Phantom Validation Experiment

After analysing practical OGSE parameters on our 3T scanner, a phantom experiment was needed to verify their feasibility prior to testing it on a human subject. The following section will describe the conducted phantom validation.

2.3.1 Introduction

The phantom of choice consisted of N-Dodecane ($CH_3(CH_2)_{10}CH_3$), an oily liquid alkane hydrocarbon that was placed inside a small 250 ml cylinder-shaped plastic container to carry out the experiments. The motivation behind the phantom of choice stemmed from the similarity of its diffusion coefficient to the diffusion coefficient of white matter in the brain, as N-Dodecane has a $D=$ 0.783×10^{-3} mm^2/s at 20C ($\sim 0.8\times10^{-3}$ mm^2/s in WM). Therefore, scanning this particular phantom should, in theory, provide an indication of feasible parameters for OGSE experiments and yield similar results as expected from a human subject.

In addition, it was of utter importance to ensure that the diffusion measurements from both OGSE and PGSE remained consistent throughout different *b*-values and frequencies in a free diffusion environment, and the way to do that was to scan a phantom with no restrictions to diffusion. In fact, a previous study on multiple n-alkane phantoms using PGSE and OGSE at different diffusion times found no dependency of ADC values on $_{\mathrm{eff}}$ [96], demonstrating its practicality. Hence, the phantom study provides a legitimate approach to confirm there are no systematic differences between the diffusion sequences.

After the previous analysis discussed in section 2.2, a more limited range of *b*-values and frequencies more adequate for realistic echo times was considered for this experiment. The following subsections describe the acquisition parameters and methodology.

2.3.2 Methods

MRI Protocol

OGSE/PGSE DTI acquisition parameters were as follows: 10 3 mm slices (no slice gap), 2×2 mm^2 in-plane resolution zero filled to 1×1 mm^2, 88×72 acquisition matrix, 6 signal averages (one b0 for each), FOV of 176 mm, partial Fourier at 75%, GRAPPA R=2, 6 diffusion encoding directions of $b = 200 - 500$ s/mm^2. The acquired OGSE frequencies were f= 40 (${}_{\mathrm{eff}}$=5.1 ms), 50 (${}_{\mathrm{eff}}$=4.3 ms), and 60 (${}_{\mathrm{eff}}$=3.7 ms) Hz, whereas the PGSE diffusion time was ${}_{\mathrm{eff}}$=40 ms. TE/TR were kept consistent between sequences, and total acquisition times for both OGSE and PGSE was TA= 56:58 min.

It was the goal at first to equalize the TE values throughout the different frequencies for the same b-value to achieve the same level of signal attenuation. However, the innate programing of the pulse sequence in the scanner made it impossible to increase the OGSE TE but for a few milliseconds (i.e. for b= 300 s/mm^2 at 40 Hz, the maximum TE is 83 ms, whereas at 60 Hz the TE is 120 ms). Therefore, there was no alternative but to utilize different echo times throughout the different frequencies, dictated by the minimum achievable TE for the OGSE sequence. Scanning parameters are detailed in Table 2.2.

Table 2.2: OGSE protocol parameters for phantom study. OGSE frequencies were set at f= 40-60 Hz for b-values in the range of b= 200-500 s/mm^2.

OGSE	b200(s/mm^2)		b300(s/mm^2)		b400(s/mm^2)		b500(s/mm^2)	
f (Hz)	**TR (ms)**	**TE (ms)**	**TR (ms)**	**TE (ms)**	**TR (ms)**	**TE (ms)**	**TR (ms)**	**TE (ms)**
40	1200	73	1700	73	2200	73	2700	73
50	1700	71	2500	100	3300	101	4100	101
60	2400	87	3500	120	4700	127	5800	161

Image Analysis

Diffusion maps were processed using ExploreDTI and ROI analysis was performed with ITK-SNAP. Figure 2.3 depicts OGSE and PGSE MD maps at b= 500 s/mm^2 shown for one slice. The mean diffusivity maps can be seen to remain consistent for both sequences in the unrestricted medium, regardless of differences in diffusion time.

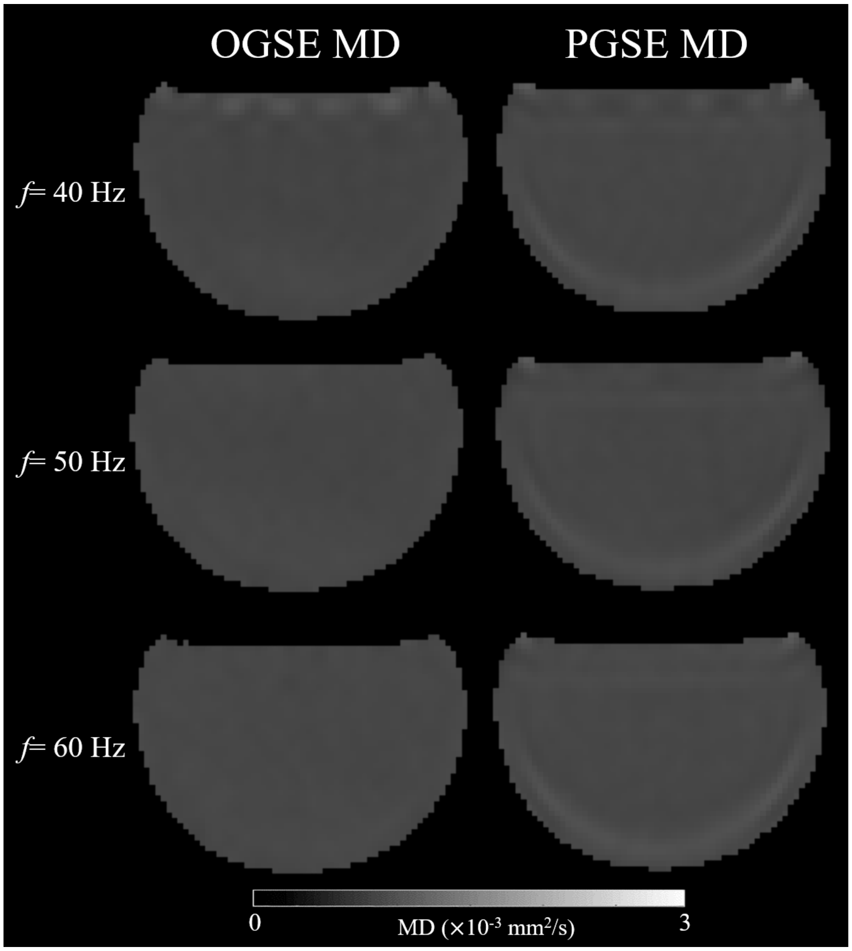

Figure 2.3: N-Dodecane OGSE/PGSE MD maps. It can be seen that mean diffusivity maps remain uniform throughout different diffusion times (shown for b= 500 s/mm^2).

2.3.3 Results

Mean OGSE and PGSE MD measurements from three different slices are plotted in Figure 2.4 for b= 200 − 500 s/mm^2. On an important note, such plots appear to compare the sequences at varying frequencies; however, it must be clarified that PGSE is not characterized by oscillating gradients (hence, has no frequency). Instead, both sequences are paired with the same TE as allowed by each of the OGSE frequencies.

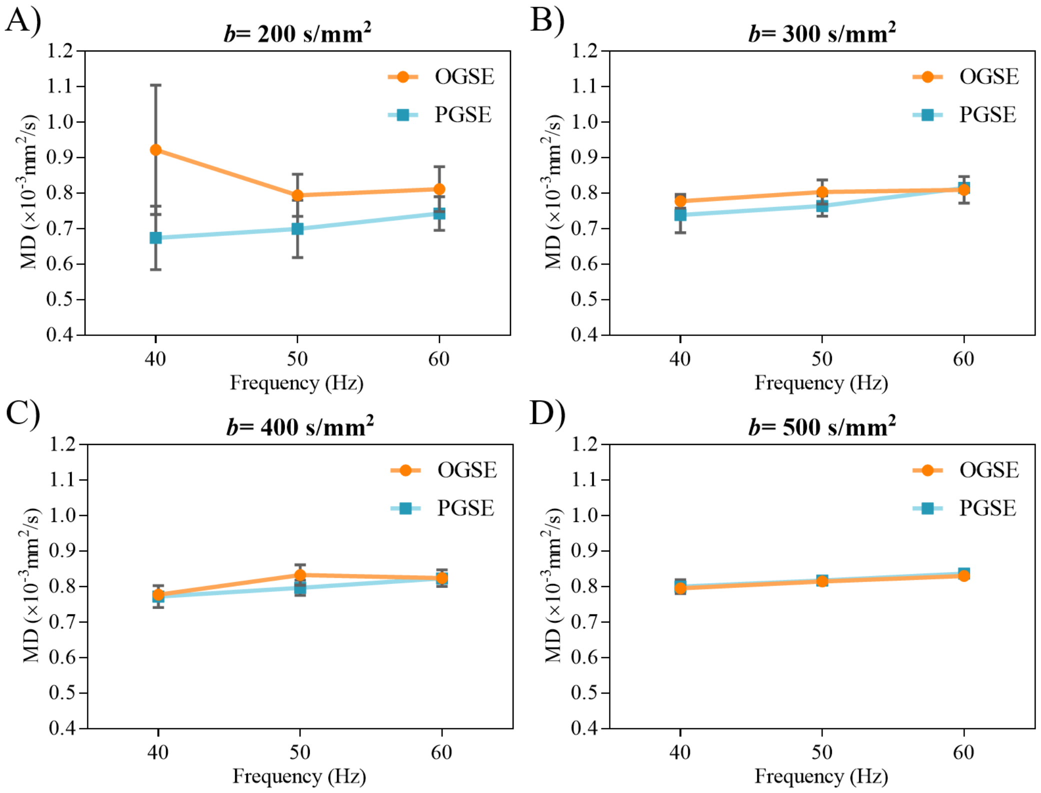

Figure 2.4: N-Dodecane MD measurements. MeanSD of OGSE and PGSE MD measurements in three different slices. A) b= 200 s/mm^2; notice the unstable MD values at different frequencies (most likely due to the very low b-value), particularly for OGSE. B) b= 300 s/mm^2; MD measurements between sequences become more similar. C) b= 400 s/mm^2; except for f= 50 Hz, the rest of the frequencies show good correlation between OGSE and PGSE MD values. D) b= 500 s/mm^2; great correlation of MD values between sequences throughout varying frequencies. Note: The independent variable in the graphs is set to be the frequency for better visual representation; however, in reality both OGSE and PGSE sequences are paired by the TE.

At the low b-value of 200 s/mm^2, the MD presents great variability between OGSE and PGSE among all frequencies, proving a persistent systematic effect. However, as the b-value is increased, the MD measurements for both sequences become more uniform. The best agreement between OGSE and PGSE can be seen for b-values of 400 s/mm^2 and 500 s/mm^2, especially the latter, at any oscillation frequency. The meanSD MD values for a b= 500 s/mm^2 with OGSE at f= 40, 50, and 60 Hz were 0.800.008$\times10^{-3}$ mm^2/s, 0.810.006$\times10^{-3}$ mm^2/s, and 0.830.008$\times10^{-3}$ mm^2/s, respectively; corresponding PGSE meanSD MD values were 0.800.02×10^{-3} mm^2/s, 0.820.02×10^{-3} mm^2/s, and 0.840.001×10^{-3} mm^2/s, respectively. All MD values are in close agreement with the expected D= 0.783×10 $^{-3}$ mm^2/s (at 20C) for this phantom, where the slight variations might be due to a different temperature at the time of the scan.

Having obtained the best agreement between OGSE MD and PGSE MD for b= 400 and 500 s/mm^2, it was decided that both values were feasible and provided confidence to investigate diffusion time effects in human brain scans.

2.4 OGSE Human Brain Experimental Data

This section will cover three different OGSE human brain pilot studies where acquisition parameters were varied to investigate their effect on the quality of the derived diffusion maps and on the quantitation of diffusion metrics in different white matter tracts. These preliminary studies were acquired on one healthy human subject only, as to establish the basis for the main OGSE human brain experiment discussed in Chapter 3.

2.4.1 Pilot Study 1

2.4.1.1 Introduction

As a brief overview, the following experiment was acquired at 2.5 mm isotropic resolution (no interpolation) with a b-value of b= 400 s/mm^2.

2.4.1.2 Methods

MRI Protocol

OGSE and PGSE DTI were acquired in one healthy volunteer (25 years old, female) with 2.5 mm isotropic voxels, 20 slices (no gap), matrix size 88×88, FOV 220 mm, b= 400 s/mm^2, 6 gradient encoding directions, phase partial Fourier at 75%, GRAPPA R= 2. Similar to previous experiments, OGSE determined the minimum TE/TR and such parameters were maintained consistent with PGSE. The acquired oscillating frequencies ranged from f=

40 – 60 Hz; NEX was increased for *f* = 60 Hz, however practical considerations limited the acquisition of more averages to maintain the same SNR across frequencies (60 Hz alone would require 16 NEX to achieve a 28% residual signal, with a total scan time of >40 min for that frequency only). Table 2.3 depicts the protocol parameters, including TA (shown as the scanning time required for a single sequence) and percentage of expected residual WM signal, considering the effects of diffusion, signal averaging, and T2 ($T2_{\mathrm{WM}}$= 58 ms).

Table 2.3: Pilot study 1: protocol parameters. OGSE and PGSE protocol parameters are shown for b=400 s/mm^2 using a 2.5 mm isotropic resolution for 20 slices.

OGSE		PGSE	b= 400 s/mm^2				
f (Hz)	**eff (ms)**	**eff (ms)**	**NEX**	**TR (ms)**	**TE (ms)**	**TA (min)**	**WM signal**
40	5.1	40	2	4300	73	1:24	28%
50	4.3	40	2	6500	102	2:03	16%
60	3.7	40	3	9200	128	3:56	12%

Image Analysis

Raw DWIs were visually inspected for motion artifacts and a common total-variation (TV) GR correction was applied using ExploreDTI v4.8.6 [97]. The aforementioned software was additionally utilized to produce MD and FA diffusion maps. ROI analysis was performed in ITK-SNAP for the following structures: genu of the corpus callosum (gCC), superior corona radiata (SCR), corticospinal tract (CST), and anterior corona radiata (ACR). Each ROI was placed in one slice that better defined the structure of interest.

2.4.1.3 Results

Calculated MD OGSE and PGSE maps are shown in Figure 2.5 for all acquired frequencies. MD maps at *f* = 40 Hz had an acceptable quality between OGSE and PGSE, whereas the maps at 50 Hz and 60 Hz began to show MD inconsistencies, as can be observed in the enlarged region around the anterior horns of the lateral ventricles (outlined in yellow).

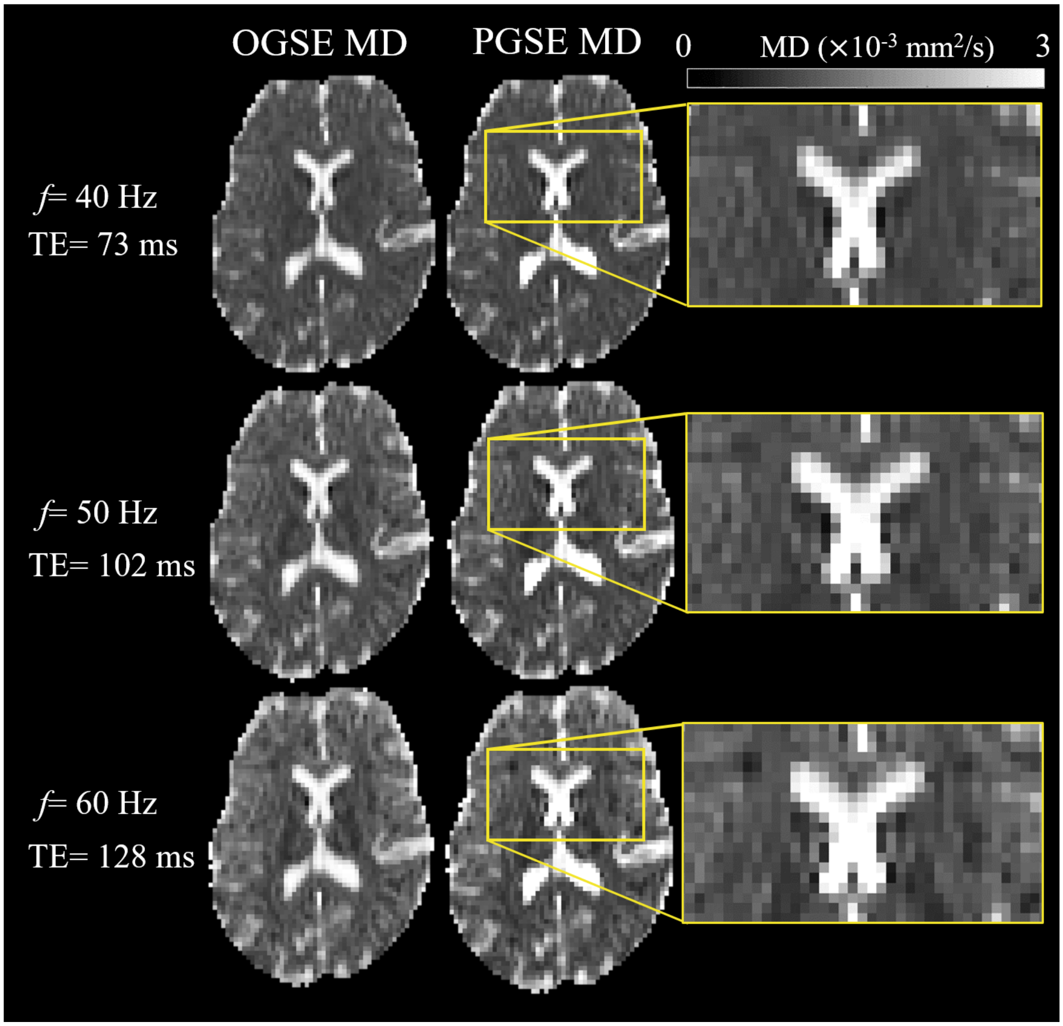

Figure 2.5: Pilot study 1: OGSE/PGSE MD maps. Images were acquired at oscillating frequencies of f= 40-60 Hz for b= 400 s/mm^2 with a 2.5 mm isotropic resolution. As frequency was increased, the TE increased causing a deterioration in image quality. The zoomed-in region highlights the noise and artifacts surrounding the lateral ventricles.

Figure 2.6 depicts the MD measurements for the above-mentioned ROIs placed in the gCC, SCR, CST, and ACR. OGSE MD is greater than PGSE MD in the SCR and CST for all frequencies, but only greater than PGSE at f= 50 Hz in the genu and ACR.

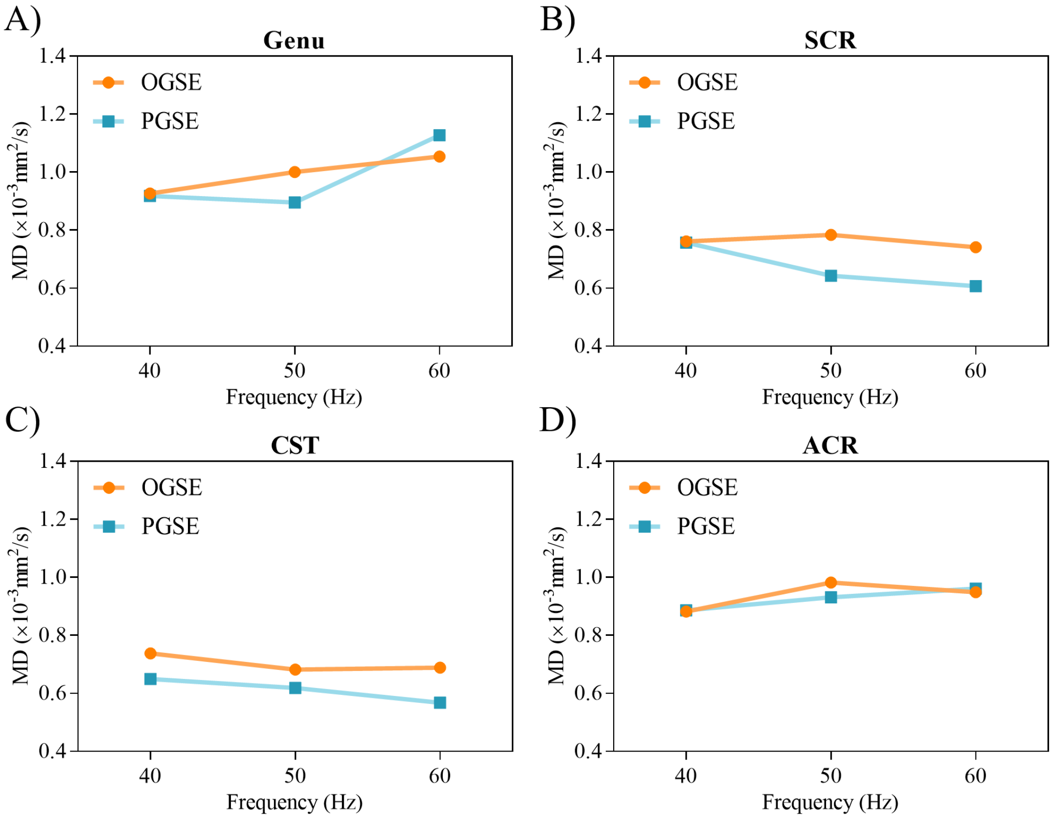

Figure 2.6: Pilot study 1: OGSE/PGSE MD measurements for f= 40-60 Hz. PGSE MD is expected to remain constant (as seen mostly in the CST and ACR) whilst OGSE MD should increase with frequency. Measurements were collected from four different ROIs as follows: A) Genu of the corpus callosum; the OGSE MD increases across all three frequencies, however PGSE appears to have a greater MD value at 60 Hz compared to OGSE. B) SCR; OSGE MD values seem to remain reasonably constant while PGSE MD slightly decreases. C) CST; MD values for both frequencies appear consistent throughout frequencies. D) ACR; OGSE MD values increase with frequency.

2.4.2 Pilot Study 2

2.4.2.1 Introduction

Given the results obtained from the previous experiment, the current protocol was designed with a higher resolution of 2 mm isotropic and f= 40 – 60 Hz. Moreover, the b-value was increased to b= 500 s/mm^2.

2.4.2.2 Methods

MRI Protocol

OGSE and PGSE DTI were acquired in one healthy volunteer (25 years old, female) at a spatial resolution of 2×2×2 mm^3 isotropic for 20 slices (no interslice gap), 6 averages with one b0 each, 6 gradient encoding directions of b= 500 s/mm^2, 88×88 matrix, FOV = 180 mm, 75% phase partial Fourier and GRAPPA R= 2. Acquired oscillating frequencies were f= 40 − 60 Hz, which determined the minimum attainable TE/TR for OGSE. To keep OGSE and PGSE sequences comparable, the PGSE TE/TR values were increased to match those for OGSE. Protocol parameters are summarized in Table 2.4, depicting an estimated percentage of WM residual signal after the effects of diffusion, signal averaging (SNR $\propto \sqrt{}$NEX), and T2$_{\mathrm{WM}}$= 58 ms.

Table 2.4: Pilot study 2: protocol parameters. OGSE and PGSE acquisition parameters using b= 500 s/mm^2 and 2 mm isotropic resolution for 20 slices. OGSE effective diffusion times for corresponding frequencies are shown, while PGSE was set at typical $_{\mathrm{eff}}$= 40 ms. Total acquisition time (TA) corresponds to a single diffusion sequence for the given TE/TR. Total scan time for the complete study was 39:18 min.

OGSE		PGSE	b= 500 s/mm^2				
f (Hz)	**eff (ms)**	**eff (ms)**	**NEX**	**TR (ms)**	**TE (ms)**	**TA (min)**	**WM signal**
40	5.1	40	6	5400	73	4:15	43%
50	4.3	40	6	8200	102	6:24	25%
60	3.7	40	6	11600	162	9:00	7%

Image Analysis

Visual inspection of the raw DWIs was performed for motion artifacts. It was decided that no motion correction method from an imaging software package would be applied in order to avoid unnecessary blurring and smoothing of the images, since if a motion artifact was detected, the data would be corrupt anyhow. Standard TV Gibbs ringing correction and processing of diffusion maps was executed using ExploreDTI. ROI analysis was completed on a single slice that best portrayed the structure of interest using the software ITK-

SNAP, for the regions: gCC, CST, SCR, and superior longitudinal fasciculus (SLF).

2.4.2.3 Results

Increasing the b-value from $b=$ 400 to $b=$ 500 s/mm^2 (i.e. compared to the previous experiment) enlarged the TE by 34 ms for the frequency of 60 Hz, while having no effect on $f=$ 40 and 50 Hz. An attempt to compensate for this considerable TE increment was made by acquiring more signal averages, but a total of ~72 NEX would have been needed to even achieve the same percentage of residual WM signal as $f=$ 50 Hz, which is not practical with respect to scanning time.

The calculated OGSE and PGSE MD maps are shown in Figure 2.7 for the acquired oscillation frequencies; PGSE and OGSE are paired by TE. The MD maps for $f=$ 40 and 50 Hz have adequate image quality and show an improvement from the previous pilot study, however as the frequency increases the maps show more heterogeneity for both sequences, with clear image artifacts and erroneous values at $f=$ 60 Hz.

Figure 2.8 illustrates OGSE and PGSE color-coded FA maps for all acquisitions. FA maps at frequencies of $f=$ 40 and 50 Hz appear to have reasonable quality, however the higher frequency of 60 Hz is inaccurate.

ROI analysis performed on OGSE and PGSE MD maps for four different WM structures is presented in Figure 2.9 (i.e. OGSE/PGSE are paired by their TE, however frequency is plotted as the independent variable). As the frequency is increased, the MD values in the genu increase for both sequences; this is because of low SNR at the higher TEs for both PGSE and OGSE. Nonetheless, OGSE MD values are constantly greater than PGSE MD for $f=$ 40-60 Hz in the CST, SCR, and SLF (Figure 2.9B, C, D, respectively), which is encouraging as the findings are in-line with expectations. In contrast with the previous experiment shown in section 2.4.1, the additional NEX acquired in this study substantially increased the SNR and allowed a better estimation of MD maps.

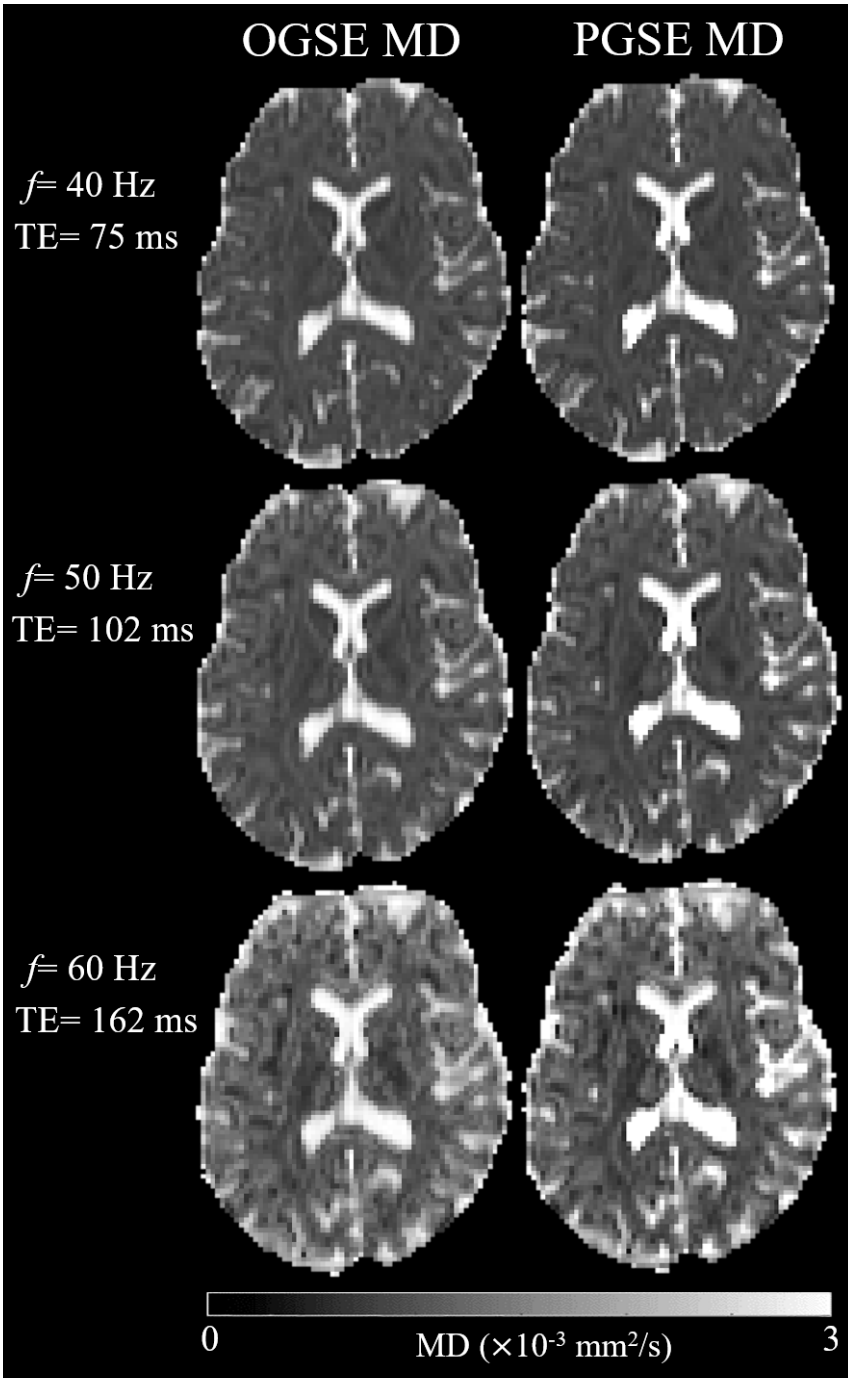

Figure 2.7: Pilot study 2: OGSE/PGSE MD maps. Images at f= 40 and 50 Hz appear to have decent quality overall, however the MD maps at f= 60 Hz have notable artifacts and erroneous MD values, partially due to the low SNR.

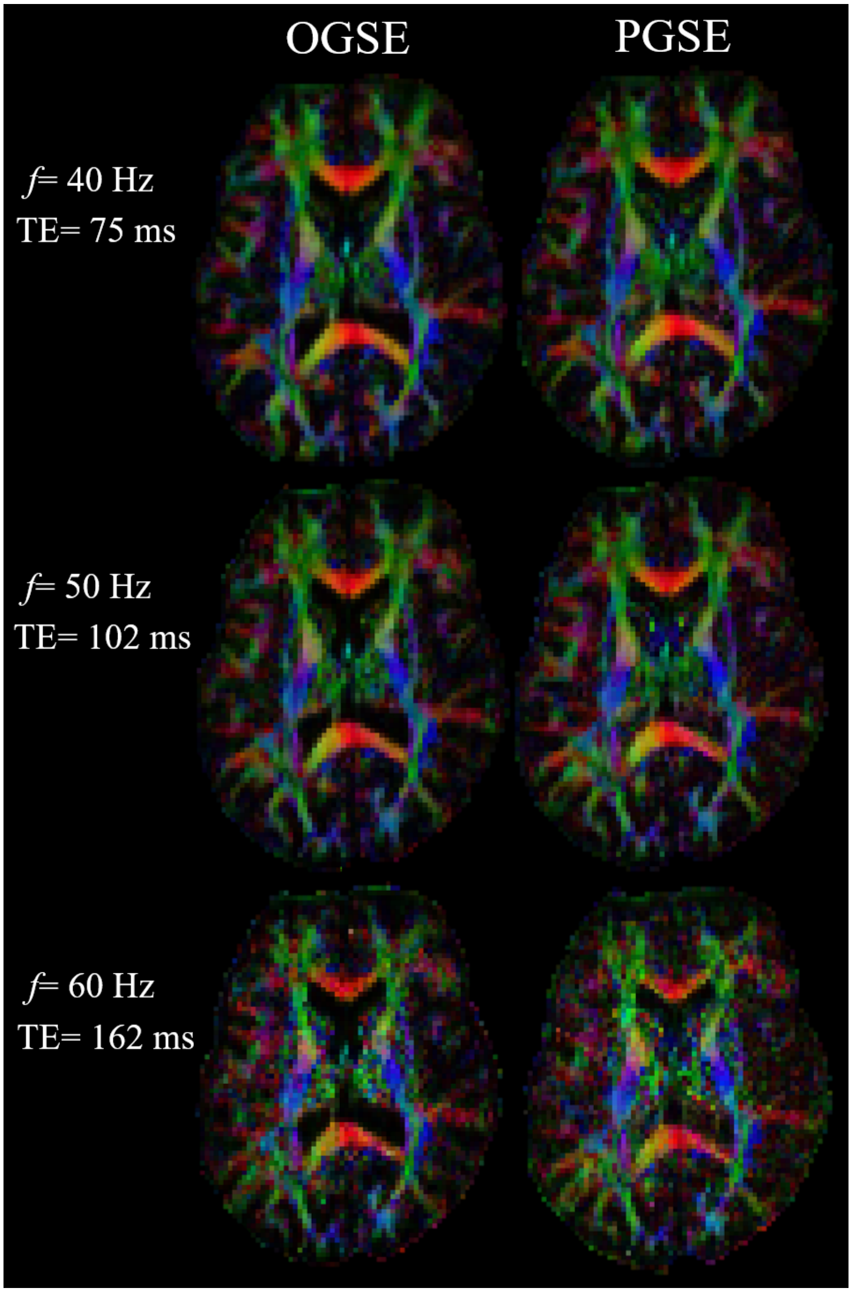

Figure 2.8: Pilot study 2: OGSE/PGSE colored-FA maps. As TE increased with frequency, the colored-FA maps progressively became noisier, especially at $f=$ 60 Hz due to low SNR.

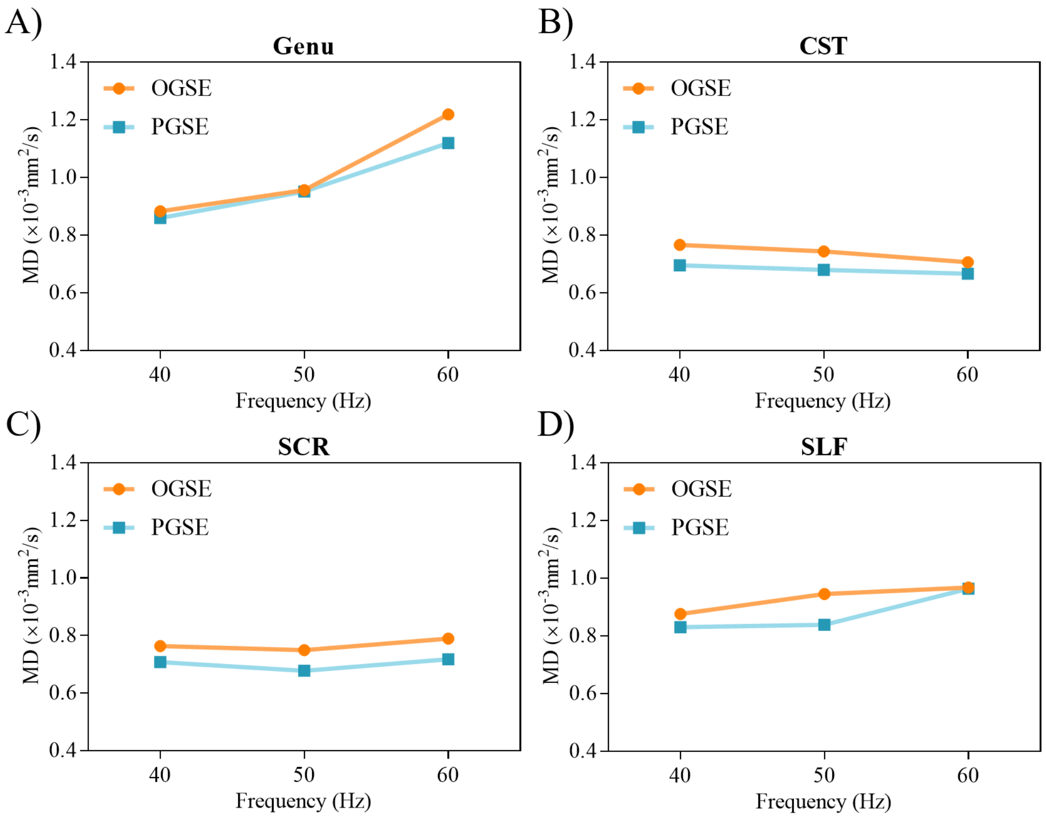

Figure 2.9: Pilot study 2: OGSE/PGSE MD measurements for f= 40-60 Hz. ROI analysis performed was for: A) Genu; both OGSE and PGSE MDs increase with oscillation frequency, whereas PGSE should remain constant. B) CST; OGSE MD is higher than PGSE MD, however it does not show an increase with frequency. C) SCR; similar to CST, OGSE MD values are constantly larger than those of PGSE across all frequencies. D) SLF; OGSE MD shows a constant increase with frequency, however PGSE MD at f= 60 Hz also increased, possibly due to low SNR.

2.4.3 Pilot Study 3

2.4.3.1 Introduction

Considering the SNR problems from the previous pilot study, specifically for the frequency of f= 60 Hz, and seeing that it was not duable to increase SNR by increasing the NEX, it was decided that the following experiment would require a different strategy. Hence, thicker slices of 3 mm were acquired at an in-plane image resolution of 2×2 mm^2 (zero-filled to 1×1 mm^2) with a smaller b-value of b= 400 s/mm^2 (i.e. to reduce the TE at f= 60 Hz and improve the diffusion tensor calculation at this frequency). In this manner, SNR was substantially increased and scan time was reduced by more than half (since less slices were required for an acceptable brain coverage) as compared to pilot study 2 discussed in section 2.4.2.

2.4.3.2 Methods

MRI Protocol

OGSE and PGSE DTI were acquired in one healthy adult (25 years, female) at 2×2 mm^2 in-plane spatial resolution zero-filled to 1×1 mm^2, 10 3 mm slices (i.e. less slices needed given the slice thickness), no inter-slice gap, GRAPPA 2, 6 averages (1 b0 for each NEX), 75% phase partial Fourier, and 6 diffusion encoding directions of b= 400 s/mm^2. The protocol was originally designed with a FOV= 144 mm and 72×88 acquisition matrix for all experiments, however during the acquisition, there was an unexpected FOV alteration and images were acquired at FOV= 144 mm and 72×88 matrix for the OGSE f= 40 Hz only, with a swapped FOV= 176 mm and 88×72 matrix for the rest of the protocols; nonetheless, this incident had no negative effect in any of the acquisition parameters. The minimum achievable OGSE TE (and therefore TR) was regulated by the oscillation frequencies acquired (f= 40-60 Hz); PGSE TE/TR were set to match the exact values. Table 2.5 describes the protocol parameters for the experiment, additionally showing an estimated residual WM signal after the process of diffusion weighting, signal averaging, and $T2_{\mathrm{WM}}$= 58 ms.

Table 2.5: Pilot study 3: protocol parameters. OGSE and PGSE acquisition parameters for b= 400 s/mm^2 at a 2×2×3 mm^3 resolution zero-filled to 1×1×3 mm^3 for 10 slices. Total acquisition time (TA) shown corresponds to a single diffusion sequence for the given TE/TR.

OGSE		PGSE	b= 400 s/mm^2				
f (Hz)	**eff (ms)**	**eff (ms)**	**NEX**	**TR (ms)**	**TE (ms)**	**TA (min)**	**WM signal**
40	5.1	40	6	2200	73	1:47	51%
50	4.3	40	6	3300	101	2:36	32%
60	3.7	40	6	4700	127	3:40	20%

Image Analysis

The first step of the analysis stage consisted in performing a visual inspection of the raw DWIs that confirmed motion-free images, followed by standard TV GR correction and generation of diffusion maps using ExploreDTI. ROIs for different WM structures were placed on a single slice that best contained the particular tract, namely on the genu and splenium of the corpus callosum (sCC), CST, posterior limb of the internal capsule (PLIC), and SCR.

2.4.3.3 Results and Discussion

A great improvement in image quality, resolution, and noise-reduction can be observed in Figure 2.10A as compared to the previous two pilot studies discussed in this chapter (sections 2.4.1 and 2.4.2). The MD maps for both diffusion sequences depict good homogeneity, even for the highest acquired frequency (i.e. $f = 60$ Hz). However, it is notable that image quality degrades as the oscillation frequency of the diffusion gradients rises, and Gibbs ringing artifacts are apparent around areas of abrupt contrast differences such as CSF/tissue boundaries for all OGSE frequencies and PGSE. Figure 2.10B illustrates the earlier OGSE ($f = 50$ Hz) human brain study acquired at 4.7T [74] for comparison. The 4.7T images were acquired at a 2×2×2.5 mm^3 resolution (zero-filled to 1×1×2.5 mm^3), $b = 300$ s/mm^2 with 6 diffusion encoding directions, 6 averages, oscillation frequency of $f = 50$ Hz, and TA= 10 min. It is notable that these earlier images contain marked Gibbs ringing (GR) artifacts throughout the entirety of the MD maps (Figure 2.10B).

Figure 2.11A, B depicts colored-FA maps for this OGSE/PGSE protocol, alongside colored-FA maps of the aforementioned earlier OSGE human brain study at $f = 50$ Hz [74]. It is clear that the maps in Figure 2.11A hold superior quality and present an improved WM definition in comparison to the analogous 4.7T study in Figure 2.11B.

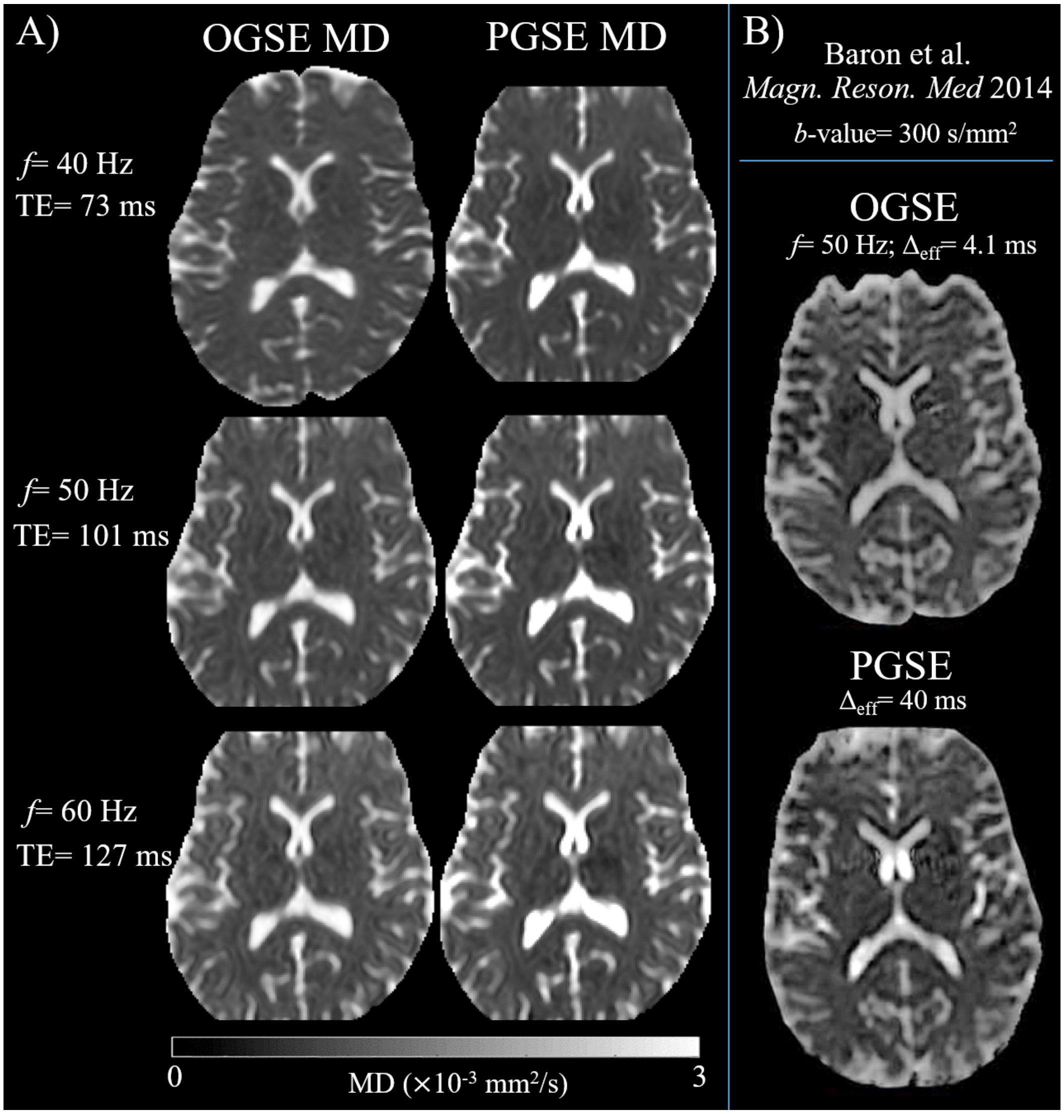

Figure 2.10: Pilot study 3: OGSE/PGSE MD maps and their comparison to previous study at 4.7T. A) Calculated MD maps for the current protocol at b= 500 s/mm^2 with 2×2×3 mm^3 resolution (zero-filled to 1×1×3 mm^3) and gradient oscillation frequencies of f= 40 – 60 Hz. A considerable quality improvement can be observed from the previous conducted pilot experiments. Maps appear more homogeneous, although GR artifacts are present, especially for f= 50-60 Hz. Note that images seem to be cropped due to the FOV shift. B) Previous OGSE human brain study acquired in a 4.7T system with 2×2×2.5 mm^3 resolution (zero-filled to 1×1×2.5 mm^3), b= 300 s/mm^2, and an oscillation frequency of f= 50 Hz. Both OGSE and PGSE MD maps depict pronounced GR artifacts shown as dark ripples (false impression of low diffusivity values). MD Maps from Baron et al., 2014. [74]

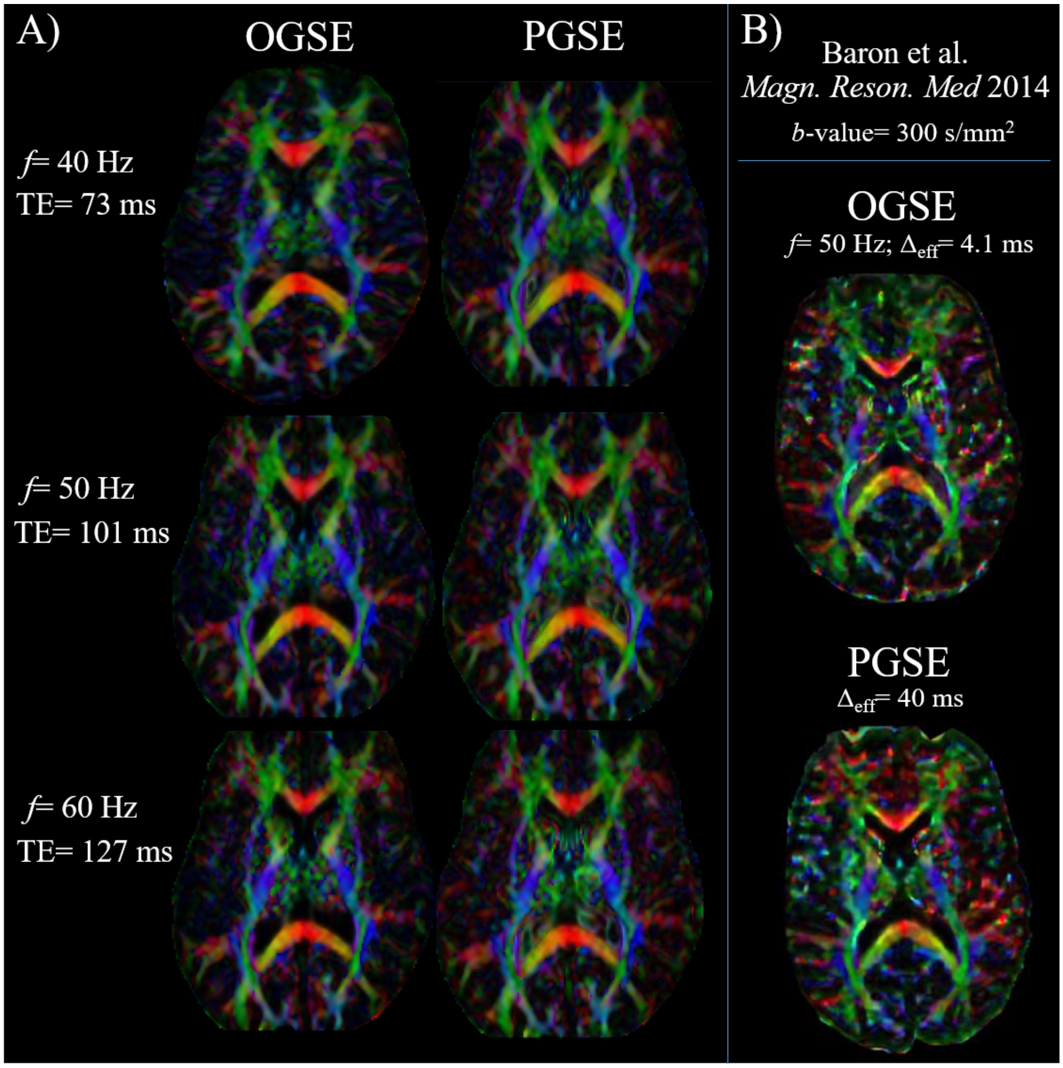

Figure 2.11: Pilot study 3: OGSE/PGSE colored-FA maps and their comparison to previous study at 4.7T. A) Calculated FA maps for current acquired protocol at b= 500 s/mm^2 with gradient oscillation frequencies of f= 40 – 60 Hz. Compared to previous acquisitions, the maps show a significant quality improvement, reduced artifacts, and a clearer definition of the WM tract boundaries. Similar to MD maps in Figure 2.10A, the FOV inadvertently changed, affecting the phase-encoding direction. B) Previous OGSE human brain study acquired in a 4.7T system with b= 300 s/mm^2 and an oscillation frequency of f= 50 Hz. Both OGSE and PGSE FA maps have reduced resolution and quality, as major WM structures appear to 'blend' with one other. Maps from Baron et al., 2014. [74]

Figure 2.12 shows the computed plots from the ROI analysis for five different white matter structures (note that once more the frequency is depicted as the independent variable for simple visualization). Overall, there was an approximately 10% difference between OGSE MD compared to PGSE MD in most WM tracts with increasing OGSE frequencies (as was expected from the difference in diffusion times), with the exception of the genu at $f = 40$ Hz that showed no differences between sequences (presumably due to Gibbs ringing artifacts). These small, but noticeable OGSE MD increases confirm an improvement in the current acquisition protocol with higher SNR. Nonetheless, the OGSE MD increase is yet to be seen growing at higher frequencies relative to PGSE.

In addition, a qualitative examination of OGSE/PGSE MD maps from Figure 2.10A revealed problematic Gibbs ringing artifacts that could be particularly appreciated with increments of the gradient oscillation frequency. A more comprehensive discussion on the characteristic GR artifact, its implications on DWI and DTI derived measures, and available approaches for its correction is examined in the next section.

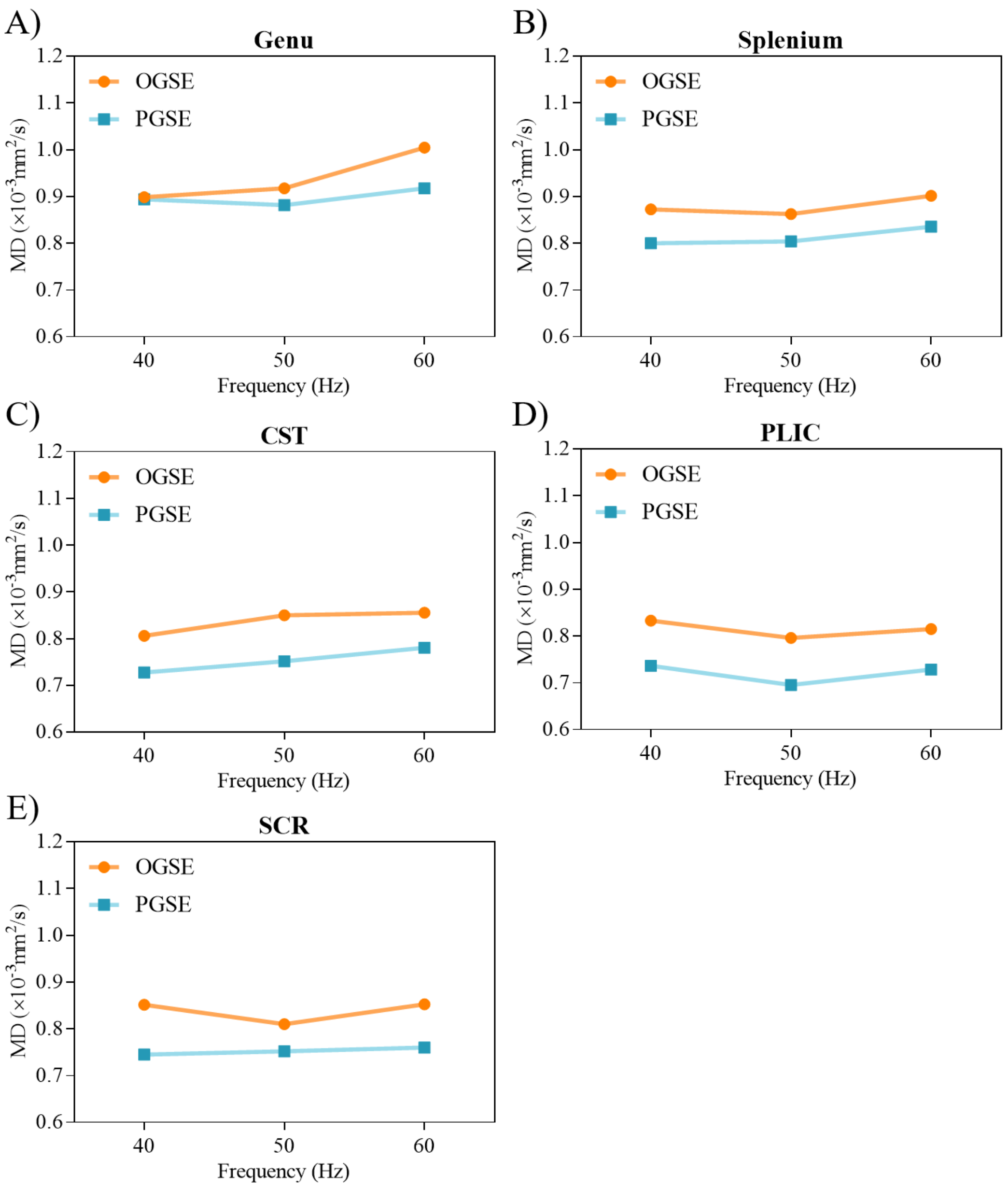

Figure 2.12: Pilot study 3: OGSE/PGSE MD measurements for f= 40 − 60 Hz. A) Genu; OGSE MDs are higher than PGSE MD with the exception of f= 40 Hz. The ROI analysis in the splenium, CST, PLIC, and SCR (plots B, C, D, and E, respectively) all revealed larger OGSE MD values compared to PGSE MD.

2.5 The Gibbs Ringing Artifact

2.5.1 What is Gibbs ringing?

Recall that the MRI scanner acquires signal in the form of spatial frequencies encoded in k-space. Following the acquisition, an image can be reconstructed from k-space data using an inverse Fourier transform. However, the image can only be perfectly reconstructed if all infinite k-space frequencies were acquired, which in practice is not possible due to sampling constraints. Therefore, during an acquisition one is effectively “truncating” or sampling only a finite amount of k-space, resulting in a loss of information from the periphery.

In fact, the outer k-space regions (i.e. high frequencies) describe the fine details and edges of an image. If part of that high-frequency information is missing, signal ripples in the form of overshoots and undershoots (Figure 2.13) will cause a “ringing effect” in the reconstructed image. These rings will commonly occur within the image around areas with sharp edges or abrupt contrast transitions, appearing in the form of parallel dark bands. Among the scientific community, this image artifact is more generally known as Gibbs ringing (GR), named after J.W. Gibbs who described the phenomenon in 1898 [98].

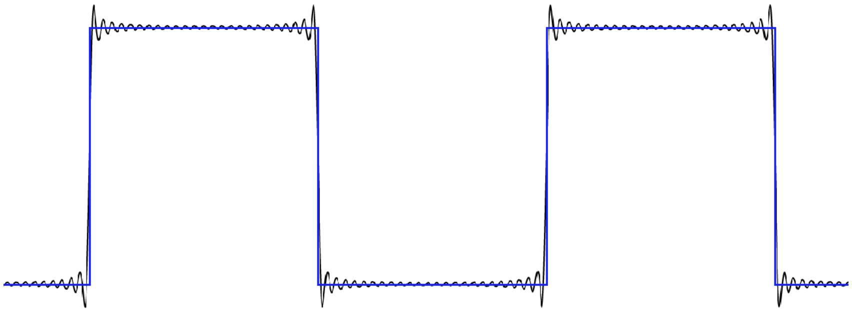

Figure 2.13: Gibbs ringing oscillations. Periodic rectangular pulse function (blue) and its approximation with a finite summation of a Fourier series (black). Notice the overshoots and undershoots around discontinuity points.

2.5.2 Gibbs ringing implications on DTI-derived data

The first study to qualitatively assess the effects of GR on DWI data was by Barker et al. in 2001 [99]; they observed that in human brain images, the range of sharp signal intensities at the interface of CSF/tissue would greatly vary between the non-diffusion weighted b0s and the diffusion-weighted images, causing different Gibbs ringing artifacts for each b-value that could potentially confound diffusion parameter estimations. Indeed, the GR artifact is more prominent on the b0 image due to the steep contrast differences arising from bright CSF immediately adjacent to lower-signal tissue, as seen in Figure 2.14.

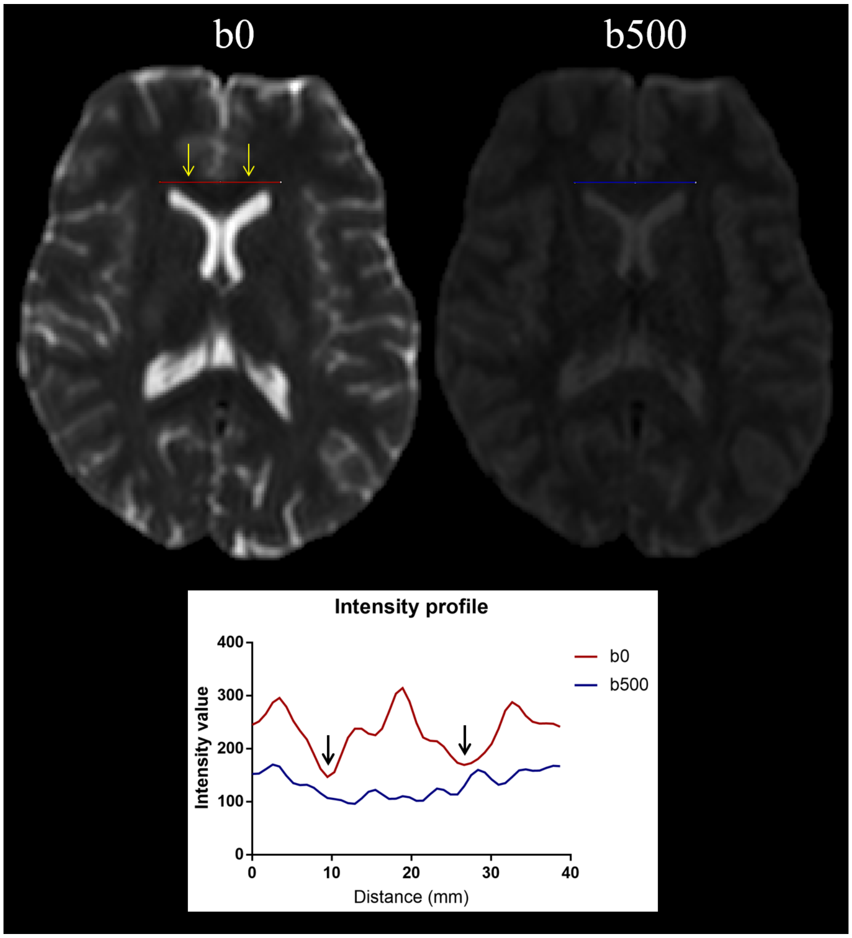

Figure 2.14: Intensity profile across the genu of the corpus callosum shown for non-diffusion weighted b0 (left) and a diffusion image at $b500$ s/mm^2 (right). The black arrows on the intensity profile plot emphasize the marked signal undershoots characteristic of Gibbs ringing on the b0 image, whereas the $b500$ is less impacted by the artifact.

Since diffusion metric maps are calculated from a combination of both non-diffusion and diffusion-weighted images, they are liable to suffer from the GR artifact and their accuracy is compromised. Figure 2.15 illustrates PGSE b0 images and corresponding MD maps across several slices with typical GR artifacts surrounding the ventricles and even some reduced MD values adjacent to the cortex.

For a long time the MRI society mostly neglected the influence of GR on the estimation of diffusion measures until recent years, when physically implausible signal (PIS) maps revealed erroneous FA values in GR-contaminated voxels [37]. Furthermore, quantitative studies began to assess the effects of the artifact on additional DTI parameters such as MD, RD, and AD. For instance, a study showed that (1) simulations with GR undershoots all caused the underestimation of MD, RD, and AD measures, but an overestimation of FA (contrary to GR overshoots that produced the opposite outcome); and (2) similarly, in real human data: mean MD, RD, and AD were found to be significantly lower and FA significantly higher before GR correction in the splenium of the corpus callosum [100]. Another realistic simulation study indicated that the contrasting signal intensities between b0s and DWIs caused a concave-like signal decay (rather than convex) with increasing b-values, resulting in the intensification of GR in parametric maps; even moderate over- and undershoots substantially affected the ADC estimation towards non-physical values [101].

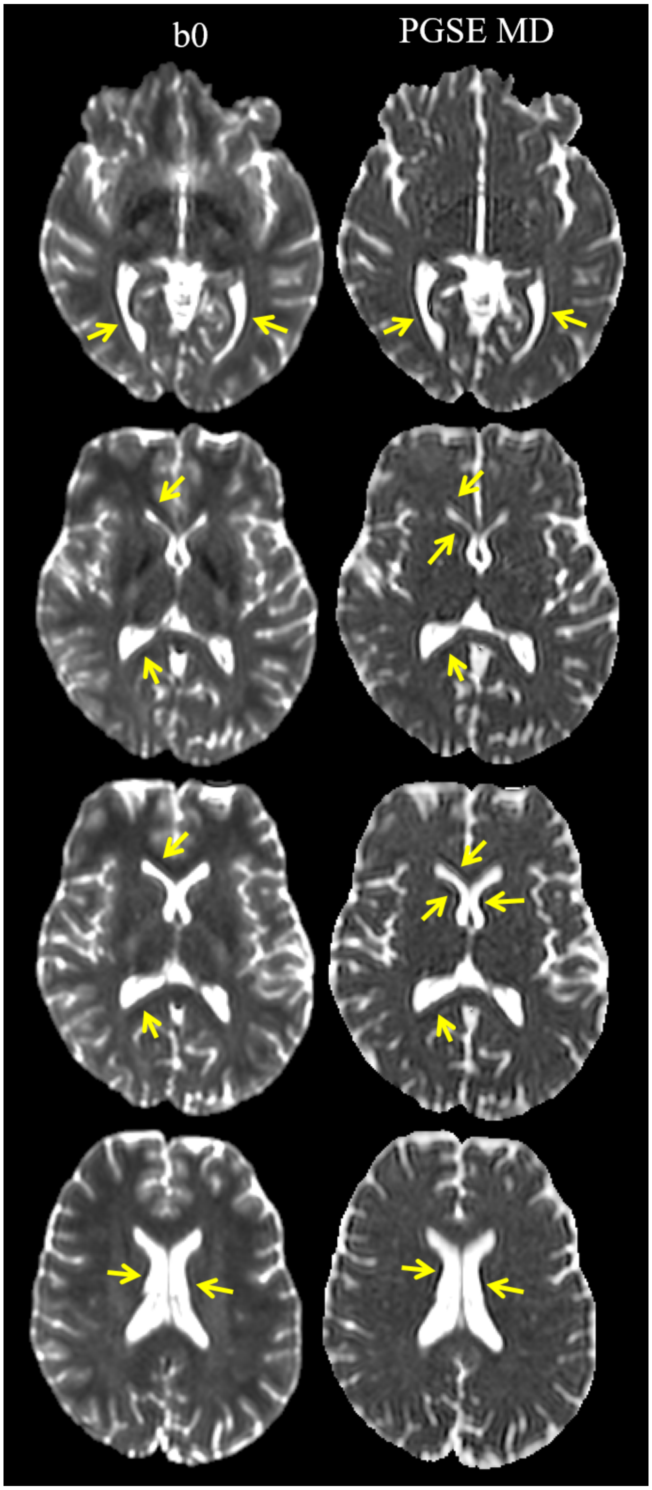

Figure 2.15: Gibbs ringing in DWI. Axial slices across the brain showing marked GR artifacts as dark bands surrounding the ventricles and proximate to the cortex in non-diffusion weighted b0 images (left) and mean diffusivity (MD) maps (right), as pointed out by yellow arrows. The artificially reduced MD values in these regions (i.e. lateral ventricles) range from ~0.14-0.67×10^{-3} mm^2/s relative to the expected 0.8×10^{-3} mm^2/s.

Clearly, the Gibbs phenomenon has proven to be a powerful confounder in the accurate estimation of diffusion measures and it is of vital interest to remove it in favor of revealing the long-sought small diffusion-time differences expected at high OGSE frequencies discussed in this chapter.

2.5.3 Gibbs ringing correction methods

Several GR post-acquisition correction methods have been proposed in the past few years (since 2015-2016 for diffusion MRI) to alleviate the problematic artifact, such as image filters (i.e. Gaussian or Lanczos) that however simultaneously create image blurring and reduce spatial resolution. Other approaches include the Gegenbauer reconstruction (based on piecewise reconstruction of smooth data) that efficiently maintains tissue integrity, although it is rather computationally costly [102]; the widely used total variation (TV) method that corrects for both noise and signal oscillations [100, 101, 103, 104], and the local subvoxel-shifts GR removal technique [105].

It is worth emphasizing that prior knowledge (i.e. pre-acquisition) of a weighting factor 'λ' is essential to carry out optimal TV corrections, and its exact value can only be calculated through simulations as it relies on the data's SNR and the acuteness of GR artifacts. That being said, it is impossible to eliminate GR effectively post-acquisition through this approach. Secondly, there is an important consideration to be made for the local subvoxel-shifts GR removal method: it assumes symmetric k-space data. Essentially, this feature indicates the method does not function properly on zero-filled (ZF) acquisitions with phase partial Fourier (PPF), a common technique used in diffusion MRI and throughout the work of this thesis to reduce TE. This situation can be observed in Figure 6 of Kellner MRM 2016 [105], where the GR correction method fails to avoid artificially low MD values in PPF-acquired human brain b0 images and MD maps.

The performance of the TV method (implemented on ExploreDTI) and the subvoxel-shifts correction technique (implemented on MRtrix3) was evaluated on non-ZF (Figure 2.16) and ZF data (Figure 2.17) for both no-PPF and PPF acquisitions to test their efficacy on the removal of the GR artifact for OGSE/PGSE derived MD maps.

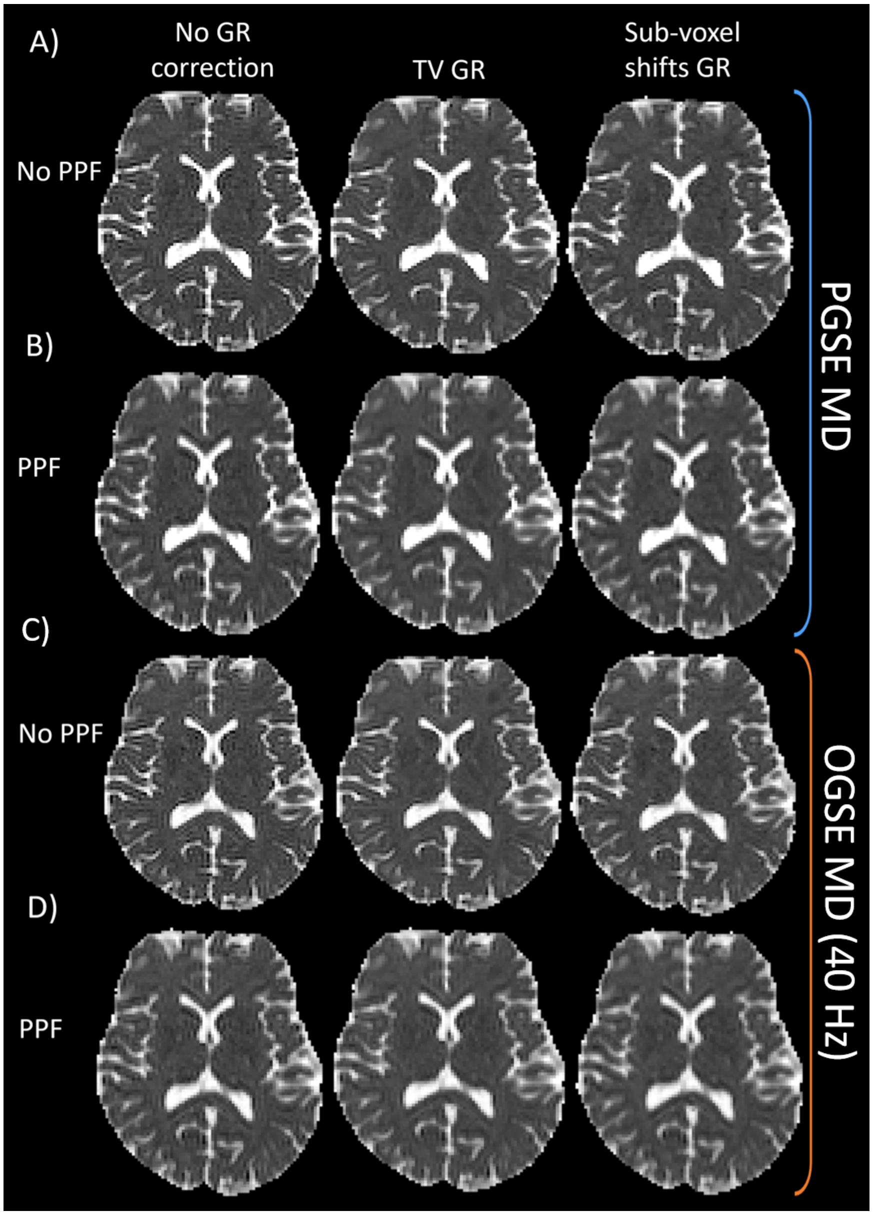

Figure 2.16: Evaluation of GR correction methods (non-ZF). MD maps with no GR correction (column 1), TV GR correction (column 2), and local sub-voxel shifts GR correction (column 3) are shown for non-zero filled full Fourier space (A, C) and 75% PPF (B, D) for PGSE (A, B) at $_{\text{eff}}$= 40 ms and OGSE (C, D) at 40 Hz, $_{\text{eff}}$= 5.1 ms for a healthy volunteer (25 year old female). Despite the use of full Fourier space and no zero filling, GR is still present post-correction, although less marked compared to PPF.

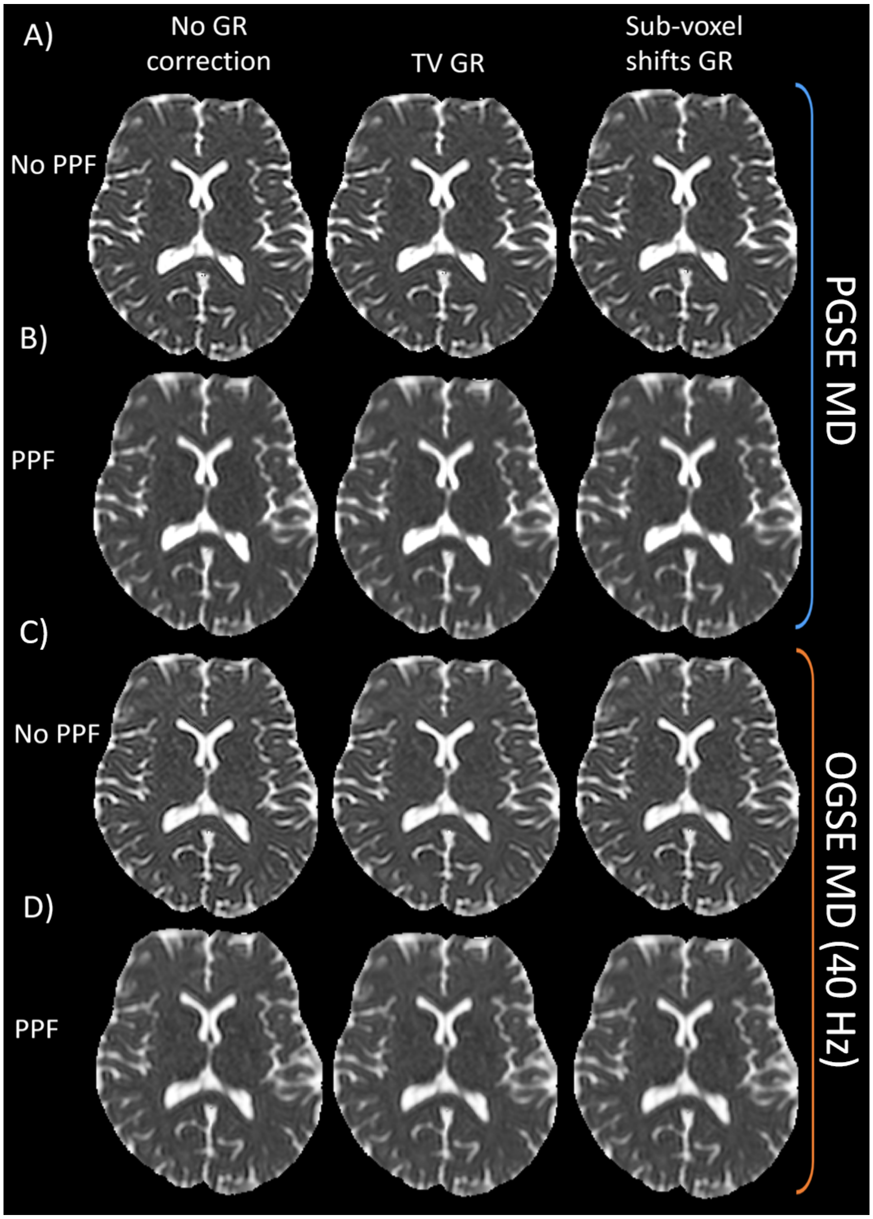

Figure 2.17: Evaluation of GR correction methods (ZF). MD maps with no GR correction (column 1), TV GR correction (column 2), and local sub-voxel shifts GR correction (column 3) are shown for zero-filled full Fourier space (A, C) and 75% PPF (B, D) for PGSE (A, B) at $_{\text{eff}}$= 40 ms and OGSE (C, D) at 40 Hz, $_{\text{eff}}$= 5.1 ms for a healthy volunteer (25 year old female). Low MD bands characteristic of GR are consistent after post-correction methods, mostly around the ventricular area.

Although both methods seem to perform better on non-ZF full k-space data, marked dark bands are still visible in both OGSE and PGSE MD maps in the periventricular area, compromising the measurements of true diffusion metrics as mainly seen in this slice for the genu and splenium of the corpus callosum, a universally studied white matter tract. Evidently, it is of utter importance to address the GR artifact in DTI acquired data as it corrupts any derived measures. Specifically, even the slightest MD underestimations can lead to obscuring very small, but measurable OGSE-PGSE differences.

All above-mentioned GR removal approaches are designed as post-acquisition remedial measures and yet do not adequately remove the artifact. Ideally, one would initially acquire data without the likelihood of developing the GR artifact. If the ringing is mainly originating from the sharp signal intensity jumps in the non-diffusion weighted b0s at CSF/tissue boundaries, then if one were to suppress that high signal, it is likely the GR artifacts would be prevented in the first place. Fluid-attenuated inversion recovery (FLAIR) is an MRI sequence used to null fluids (i.e. CSF) by means of an inversion time (TI) measured between the application of a 180° inversion pulse and a 90° excitation RF pulse, and was first implemented in the clinical setting in 1985 [106].

Since then, the inversion recovery sequence has proven beneficial in brain studies for different applications, such as to reduce the appearance of flow artifacts [107, 108], in conditions such as traumatic brain injury [109], and even multiple sclerosis [110, 111]. In addition, FLAIR has been widely incorporated with diffusion studies for the main reason of removing CSF partial volume effects [38, 112–116]. Nonetheless, to the best of my knowledge, FLAIR has never been applied before for the sole prevention of GR artifacts in diffusion MRI. Therefore, an assessment of its feasibility in the generation of artifact-free, high quality data is required as to properly investigate the very small OGSE-PSGE differences. However, FLAIR acquisitions do considerably increase the TR and hence the total acquisition time.

Chapter 3 provides an in-depth evaluation of the viability of FLAIR OGSE/PGSE acquisitions and its efficacy in the removal of the Gibbs ringing artifact to uncover the true diffusion parameter estimations as a function of diffusion time in healthy young adult human brain.

3 Fluid-Suppressed Oscillating Gradient Spin-Echo DTI Demonstrates Variable Diffusion Time Dependency Across the Human Brain

3.1 Introduction

The apparent diffusion coefficient or mean diffusivity (MD) can be calculated from diffusion-weighted imaging (DWI) based upon the time water molecules are allowed to assess their surroundings, also known as the effective diffusion time ($_{\text{eff}}$) [117]. At long diffusion times (i.e. $_{\text{eff}}=$ 40 ms for typical human studies), water molecules will have dispersed far enough in both small and large axons to be impeded by characteristic cellular barriers such as the axonal membrane, resulting in a similar measure of the diffusion coefficient despite the different-sized axonal calibers. However, if water molecules were only permitted to travel for a very short time (i.e. $_{\text{eff}}\leq$5 ms), diffusion would become less restricted for wider axons as they would have less time to reach these boundaries, whilst it would remain restricted for thinner axons. The latter approach enables a measurable change of the diffusion coefficient that can provide insight into the varying micro-scale tissue differences within the brain. The well-known Pulsed-Gradient Spin-Echo (PGSE) has been the gold standard DWI sequence to image diffusion of water [118]. Nevertheless, its typically long diffusion time ($_{\text{eff}}=$ 40 ms) is not particularly sensitive to explore tissue in the smaller spatial scale (i.e. <5m), and it would require very high gradient amplitudes to achieve shorter diffusion times.

Conversely, oscillating-gradient spin-echo (OGSE) diffusion tensor imaging (DTI) facilitates shorter diffusion times that can yield insight into the aforementioned micro-structural scale restrictions of water diffusion [72, 76]. OGSE maximizes current hardware components by trading the pulsed gradients characteristic of PGSE for two oscillating, periodic waveforms, sampling the diffusion spectrum by adjusting the frequency range of the sinusoidal diffusion-weighted gradients. The higher the frequency, the shorter the diffusion times attained. There have been several OGSE simulations [71, 78, 119, 120] and animal studies [68, 80–84, 88, 121] that examine the advantages of short diffusion times for the elucidation of microstructural features in brain tissue (not an exhaustive list). However, there have been limited OGSE human studies on healthy brain [73, 74, 89, 93], stroke [48, 90], and tumours/cysts [91, 92], mostly due to unavoidable hardware limitations (i.e. maximum gradient strength) in current clinical scanners. In addition, only one study examined the tensor parameters in multiple white matter tracts and two gray matter regions, where 7 tracts showed significant increases of up 20% and 40% in parallel (i.e. AD, $\lambda_{\|}$) and perpendicular (i.e. RD, $\lambda_{\perp}$) diffusivities, respectively, as well as a significant decrease of FA in 4/8 tracts [74]. One other whole-brain study at 7T analyzed different white matter tracts through diffusion dispersion imaging [93], whereas the other two healthy brain studies only measured the corpus callosum [73, 89]. An alternative high b-value method of investigating the brain microstructure with AxCaliber type modelling suggested differences of axon diameters between various tracts with the corticospinal tract (CST), superior longitudinal fasciculus (SLF), and forceps major having the largest diameters, albeit with data acquired using very long scan times of 55 min on a high-performance gradient Connectome 3T [122].

Probing the nerve cell microenvironment in the human brain is one key to understanding biological processes in both health and disease. To achieve this, though, it is essential to obtain high quality images to ensure the derived measurements are reliable. As a low-resolution technique, DWI data is particularly sensitive to noise and image artifacts such as Gibbs ringing (GR) and partial-volume effects. The problematic GR artifacts arise from sharp contrast differences between areas with bright cerebrospinal fluid (CSF) (on non-diffusion-weighted b0) and brain tissue, causing marked dark rims to form on MD maps around these tissue boundaries, such as adjacent to the ventricles [123]. Consequentially, the ringing can obscure the quantification of small diffusion parameter differences between OGSE and PGSE sequences.

Even so, the GR artifact has long been overlooked and underestimated by the diffusion MRI community. The previous OGSE human brain study that performed a tract-based analysis on several white matter tracts depicted a voxel by voxel OGSE – PSGE difference map for both the parallel and perpendicular eigenvalues [74]. Although displaying an increment for both eigenvalues at the shortest diffusion time, the difference map does not appear to highlight any specific regions as was expected from the quantitative analysis, possibly due to the contribution of image artifacts such as GR, notwithstanding the already very small OGSE – PGSE differences involved. It has been previously shown that GR creates signal intensity undershoots and overshoots that cause erroneous diffusion parameter estimations such as lower MD, axial diffusivity (AD), and radial diffusivity (RD), as well as higher fractional anisotropy (FA) [100, 101]. The Gibbs ringing artifact has therefore attracted attention with various corrective strategies in the post-acquisition stage to overcome problems in diffusion estimations, although the algorithms often need full Fourier space (or else it still fails to avoid generating low MD regions at the periventricular area) [105] or a priori knowledge of an optimal lambda value (obtained uniquely through noised-based estimations [101] and simulations [100]). All three methods, though, agree with one fact: GR is a function of the amount of diffusion weighting and its severity will depend on the degree of signal intensity variations between CSF/tissue interfaces.

Facing the challenges around the artifact removal during post-processing, a straightforward solution is to null CSF in the acquisition. Numerous diffusion MRI studies in the past have applied inversion recovery sequences to suppress CSF contributions with a primary focus on reducing partial volume effects and not necessarily to avoid GR, such as in cortical gray matter [112], DTI [114], tractography [115], and stroke [113], as some of these earlier investigations were acquired at low spatial resolution and SNR. The focus of this work is, for the first time, to avert the artifact by acquiring fluid-attenuated inversion-recovery (FLAIR) [106] OGSE DTI data to investigate diffusion-time effects throughout the brain. The application of the inversion recovery sequence nulls the signal originating from CSF, preventing the appearance of the abrupt bright signal boundaries in the image. This methodology provides numerous advantages, as it enables the estimation of uncorrupted, high quality, consistent diffusion maps. However, scans become somewhat longer with the addition of the inversion time (TI) and more averages are required to compensate for signal loss. The purpose here is to evaluate the efficacy of FLAIR OGSE (versus FLAIR PGSE) for assessing potential differences of diffusion time dependencies in various white matter and gray matter regions in healthy adults.

3.2 Methods

3.2.1 Image Acquisition

Eight healthy volunteers (mean 263 (23-30) years old, 4 males/4 females) were recruited to participate in this study and provided written informed consent. Magnetic resonance images were acquired on a 3T MAGNETOM Prisma (Siemens Healthcare, Erlangen, Germany) with a 64-channel head coil using an Advanced WIP 919C (single-shot echo-planar imaging (EPI) sequence prototype). The four-scan protocol (26 min total) incorporated PGSE and OGSE (trapezoid and trapezoid-cosine diffusion sensitizing gradients, respectively) both with and without CSF suppression. Acquisition parameters were as follows: 48 3 mm thick slices to cover whole-brain and cerebellum with no slice gap at 1.7×1.7 mm^2 in-plane resolution (zero filled to 0.85×0.85 mm^2), field of view (FOV) 220 mm, matrix size 128×128, anterior-to-posterior phase-encoding, 3 averages, GRAPPA acceleration mode with a factor of 2, phase partial Fourier (PPF) at 75%, and b-value 500 s/mm^2 using 6 diffusion sensitizing gradient directions. The TR for OGSE was nearly double as that for PGSE in both FLAIR and non-FLAIR scans, presumably due to the high duty cycle of the oscillating gradients. Scanning time parameters are detailed in Table 3.1 (TE was kept nearly equivalent for both OGSE/PGSE between non-FLAIR and FLAIR protocols to discard T2 effects).

Although acquiring the data with a greater number of gradient encoding directions would be ideal, the TE for FLAIR would increase from 83 ms to 130 ms by shifting from 6 to 10 directions, which would be associated with SNR loss. Further, the focus here is on low b-value and tensor analysis. The PGSE effective diffusion time, duration, and separation were $_{\mathrm{eff}} = 40$ ms, $_{\mathrm{eff}}=$ 3.9 ms, and $_{\mathrm{sep}}=$ 41.4 ms, respectively. The OGSE diffusion time was much shorter with $_{\mathrm{eff}} = 5.1$ ms at f$=$ 40 Hz, accommodating 4 lobes on either side of the refocusing pulse. The current 3T study utilizes a higher b-value of 500 s/mm^2 and lower frequency of 40 Hz relative to our previous 4.7T OGSE study [74]($b=$ 300 s/mm^2, 50 Hz). The SNR measurements collected from the b0 images (i.e. calculated as the ratio of the mean signal intensity in the genu divided by the standard deviation of air in the background) were $\sim$104 and $\sim$95 for the OGSE and PGSE FLAIR sequences, respectively, and $\sim$110 and $\sim$105 for the OGSE and PGSE non-FLAIR acquisitions, respectively.

Table 3.1: PGSE and OGSE acquisition parameters for typical non-FLAIR and FLAIR.

Protocol	TE (ms)	TR (s)	TA (min)	TI (s)
PGSE Non-FLAIR	80	5.6	2:33	-
OGSE Non-FLAIR - 40 Hz	80	13.1	5:41	-
PGSE FLAIR	83	12.8	5:33	2.3
OGSE FLAIR - 40 Hz	83	27	11:28	2.3

3.2.2 DTI Region of Interest Analysis

Post-processing included Total-variation (TV) Gibbs ringing (GR) correction and subsequent calculation of Mean, Fractional, Radial, and Axial Diffusivity maps (MD, FA, RD, and AD, respectively) on ExploreDTI v4.8.6 [97]. OGSE-PGSE difference maps were calculated per voxel for all diffusion metrics, and an automated brain masking approach in ExploreDTI was applied to remove the skull and adjacent noise voxels. Given the lack of artifacts with FLAIR preparation (discussed in Results), manual region of interest (ROI) analysis was performed (ITK-SNAP [124]) on only the FLAIR OGSE-PGSE difference maps for every diffusion parameter (guided by the directionally encoded FA maps) to evaluate nine white matter regions, namely the anterior limb of the internal capsule (ALIC), posterior limb of the internal capsule (PLIC), corpus callosum (CC) subdivided into three main regions (genu CC, body CC, and splenium CC), inferior fronto-occipital fasciculus (IFO), superior longitudinal fasciculus (SLF), corticospinal tract (CST), and white matter portions of the cerebellum, as well as two deep gray matter structures (thalamus and caudate) for comparison purposes. ROIs were delineated only on slices that had a good depiction of each structure (and on both left and right hemispheres for bilateral regions: ALIC, PLIC, IFO, SLF, CST, cerebellum, thalamus, and caudate - which were averaged as one measurement) to yield one value per region per participant, which were then averaged over the eight subjects. Two non-parametric tests were used: a sign test to compare whether the OGSE-PGSE diffusion differences differed from zero and a Wilcoxon signed rank test to examine differences between compared regions ($p<0.05$).

3.3 Results

3.3.1 Improved DTI Map Quality with FLAIR

The standard non-FLAIR on both PGSE and OGSE displays focal and marked artifacts on the MD maps caused by Gibbs ringing in regions near CSF, for example the zoomed-in area of the genu and lateral ventricles (as pointed out by the arrows in Figure 3.1A, 3.1C), despite the use of Gibbs ringing correction in post-processing [100]. This problematic artifact is prone to cause bias in the diffusion parameter estimations and measurements due to the low MD in this and other brain regions. The use of FLAIR for attenuating the bright CSF signal on the b0 images (and an additive effect with diffusion-weighting on the b500 images) avoided these dark MD regions (as low as 0.64×10^{-3} mm^2/s on non-FLAIR DTI versus 0.89×10^{-3} mm^2/s in the same CC region on FLAIR) characteristic of Gibbs ringing and lead to the expected uniform MD maps, as well as good-quality FA maps, for both PGSE and OGSE (Figure 3.1B, 3.1D).

Given the more accurate diffusion maps with CSF-suppression, only FLAIR acquisitions were utilized for subsequent diffusion parameter analysis across brain regions. Voxel-by-voxel OGSE-PGSE difference maps were calculated and color-coded to visually inspect the areas with highest diffusion-time dependence, as shown in Figure 3.2 for MD (note that the MD difference map has been overlaid on an FA map for anatomical reference). It is evident that such areas are clustered mainly within white matter regions, with some of the greatest OGSE-PGSE MD increases (some voxels with MD$>0.1\times10^{-3}$ mm^2/s in this example) in the core tracts such as corpus callosum, PLIC, CST, and SLF.

As expected, MD from the shorter diffusion-time OGSE was significantly greater than that derived from the longer diffusion-time PGSE for all nine white matter regions, but not for the two deep gray matter structures (Figure 3.3). The highest MD diffusion-time dependences was found in the CST (OGSE MD - PGSE MD= $0.060.01\times10^{-3}$ mm^2/s), followed by the

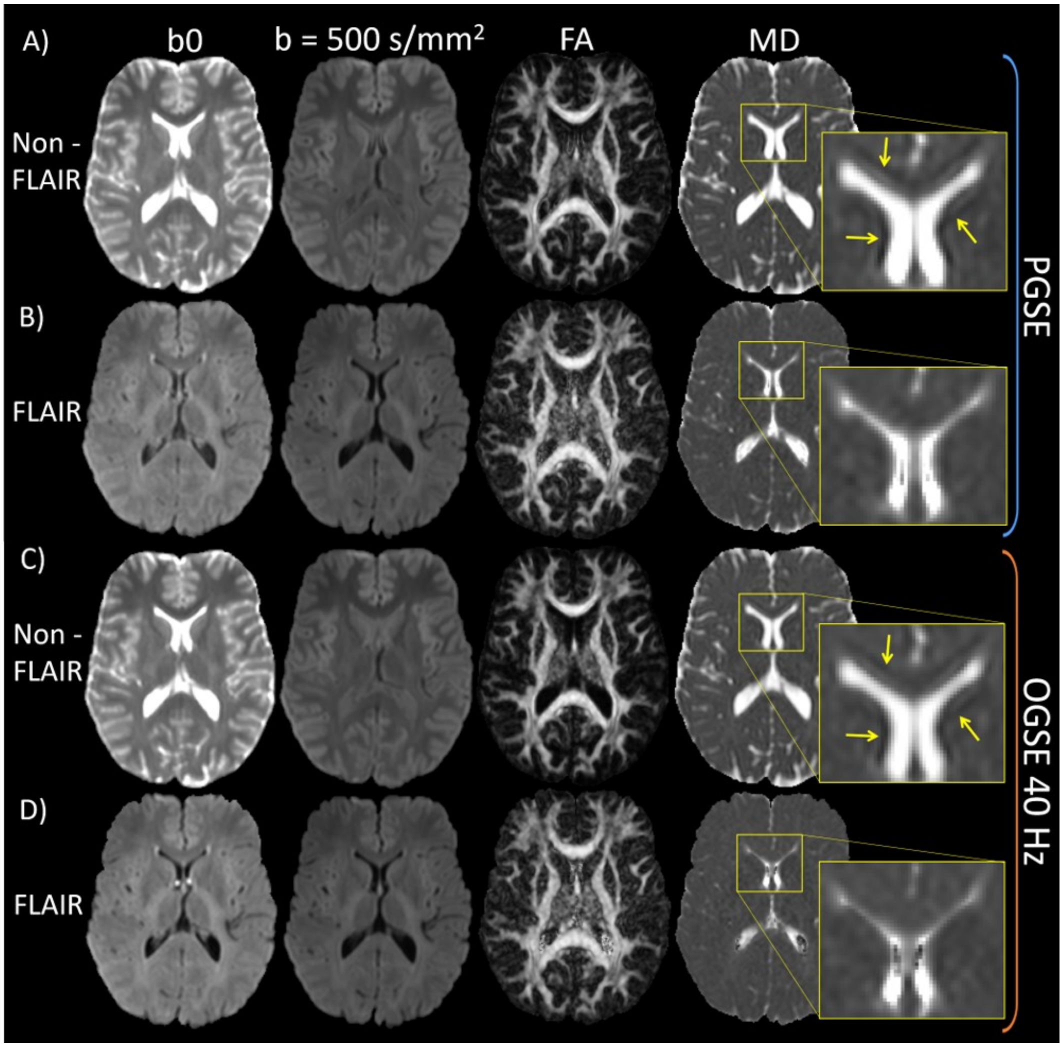

Figure 3.1: PGSE and OGSE with/without FLAIR. Mean images at b= 0 s/mm^2 and 500 s/mm^2 and FA and MD maps are shown for the standard non-FLAIR (A, C) and FLAIR (B, D) DTI protocols for PGSE (A, B) at $_{\text{eff}}$= 40 ms and OGSE (C, D) at 40 Hz, $_{\text{eff}}$= 5.1 ms for a healthy volunteer (25 year old female). Notice the pronounced Gibbs ringing artifact (as pointed out by the arrows) for the non-FLAIR MD maps around the lateral ventricles near the genu and its absence in the FLAIR MD maps. Note that the detrimental Gibbs ringing artifact can go unnoticed if visualized only on the FA maps.

PLIC, SLF, and splenium CC. FA presented a significant decrease in the CST (-0.030.01) and an increase in ALIC (0.030.02), whereas the rest did not differ between OGSE and PGSE. RD showed a distinct elevation in the CST (0.060.01×10^{-3} mm^2/s), SLF, PLIC, and IFO comparable to the observed increases in MD across the eight subjects. All the white matter structures displayed increments in AD, especially higher for all callosal subcomponents (up to 0.100.02×10^{-3} mm^2/s in the splenium) and the PLIC, whereas the two gray matter regions showed no change.

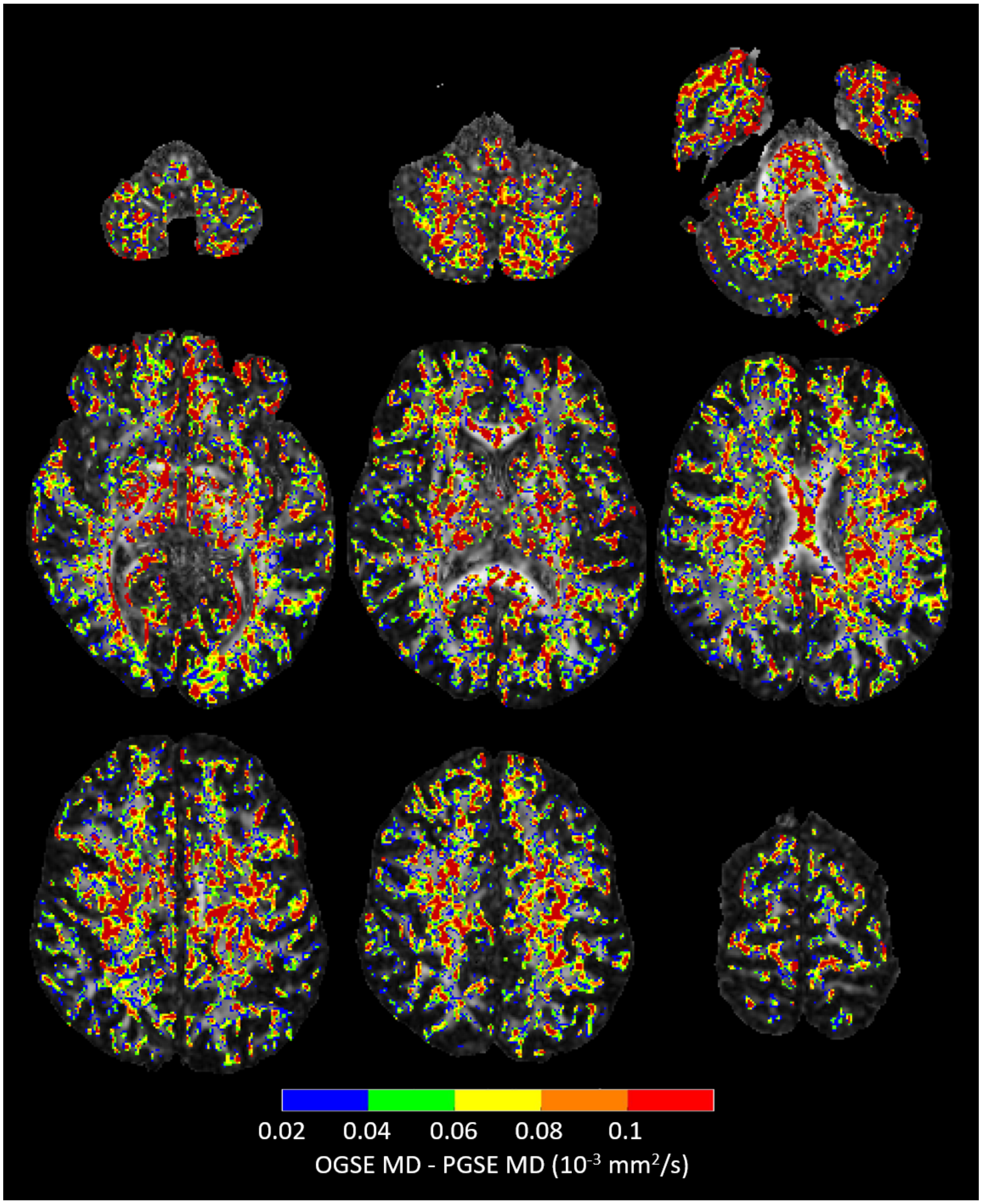

Figure 3.2: Voxel-by-voxel subtraction of OGSE MD - PGSE MD shown for nine axial slices in one healthy volunteer (25 year old female). Note that an FA map is employed as an overlay for anatomical reference. MD diffusion-time dependences can be observed throughout the whole brain white matter regions, notably higher in core tracts.

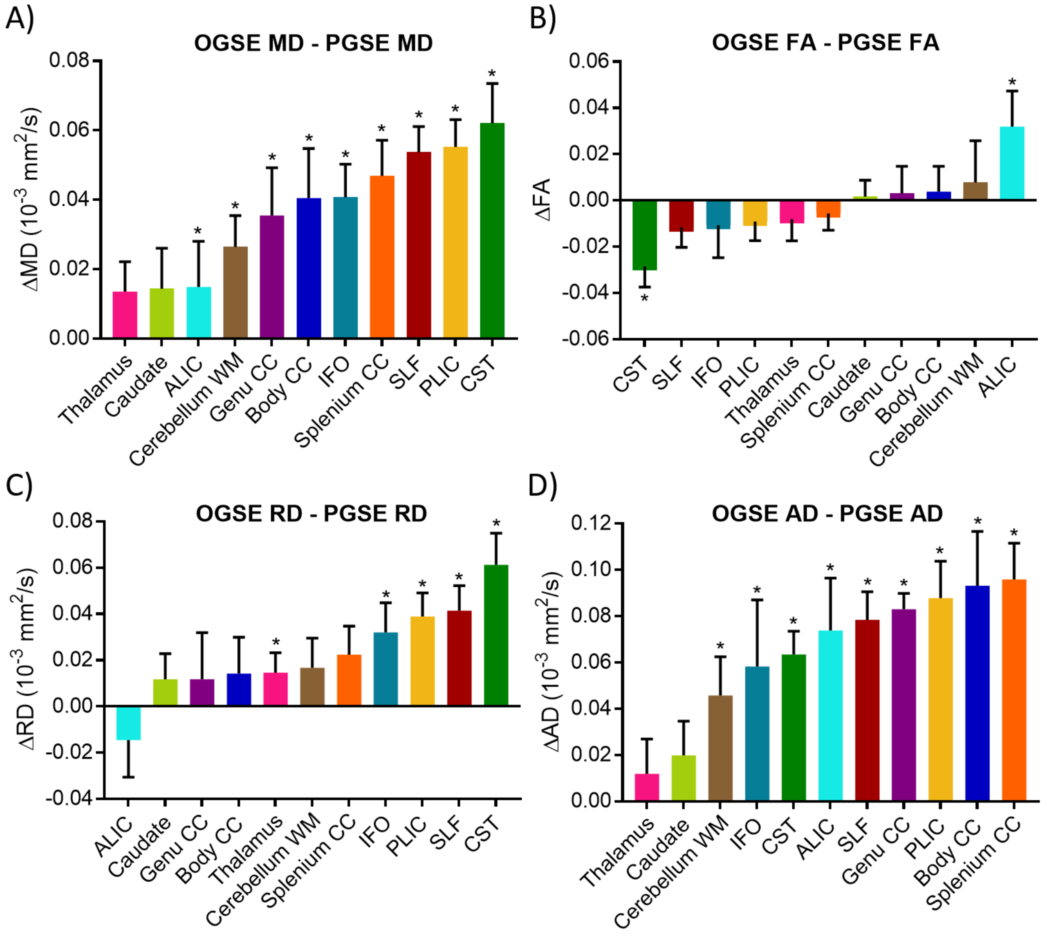

Figure 3.3: OGSE - PGSE diffusion parameter differences for FLAIR DTI over eight healthy subjects (mean SD) for nine white matter regions and two deep gray matter structures. Significant diffusion-time dependences can be observed for both (A) MD and (D) AD for all nine white matter regions at shorter diffusion times (i.e. $_{\mathrm{eff}}$= 5.1 ms). (C) Radial diffusivity increases in 4/9 tracts, remaining consistent with those that show highest differences in MD (e.g. CST, SLF. PLIC). (B) FA shows a notable decrease in only one tract (CST), as well as an increase in one tract (ALIC).

OGSE – PGSE diffusion parameter differences per tract for all eight subjects are depicted in Figure 3.4. In agreement with Figure 3.3, the MD differences were highest in the CST for most subjects, while the thalamus and caudate had the lowest MD values. OGSE RD - PGSE RD differences were greatest in the CST for all subjects. Similar to MD, the lowest AD differences were found in the two deep gray matter regions for all subjects.

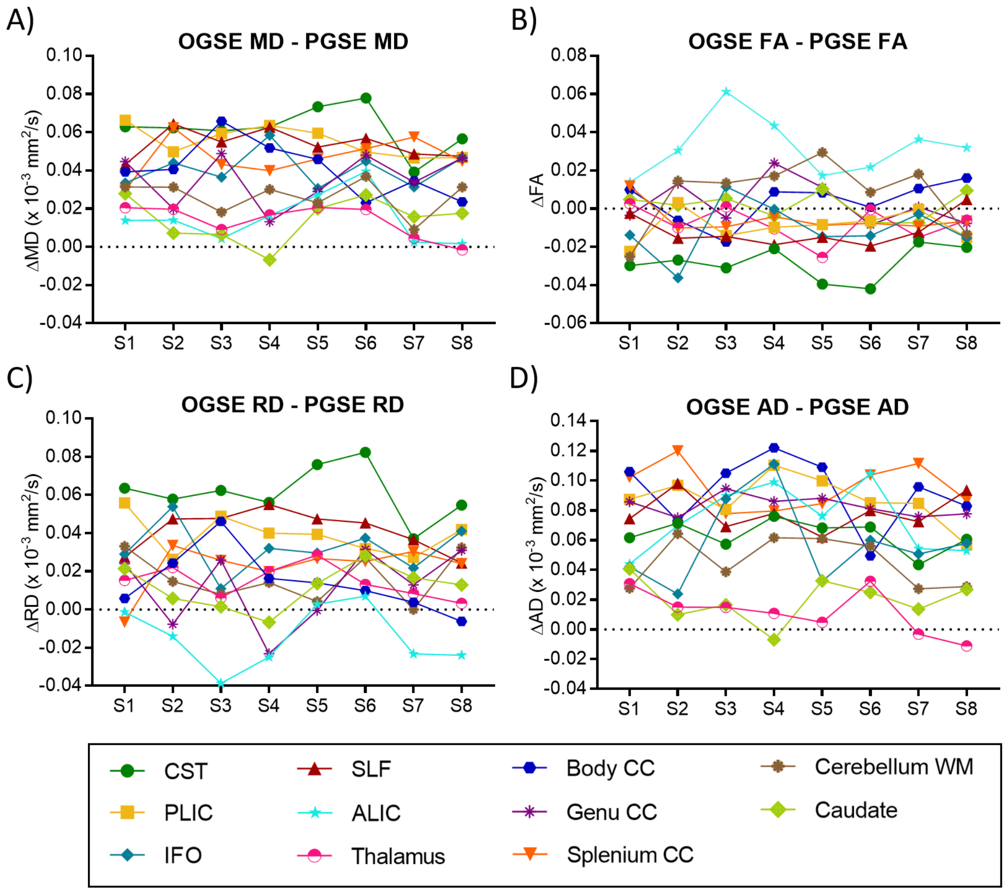

Figure 3.4: OGSE - PGSE differences of absolute diffusion parameters for FLAIR DTI per studied region (i.e. 9 WM/2 GM) for eight healthy subjects (S1-S8). Notice that both deep gray matter structures have the lowest (A) MD and (D) AD diffusion differences at shorter diffusion times (i.e. OGSE $_{\text{eff}}$= 5.1 ms) relative to longer diffusion times ($_{\text{eff}}$= 40 ms). (C) Radial diffusivity in the CST was the highest across all subjects, followed by the SLF and PLIC. (B) In 7/8 subjects, the CST had the lowest FA differences and ALIC the highest.

Significant OGSE – PGSE diffusion metric differences between paired regions are shown in Figure 3.5. Excluding one another, the CST, PLIC, and SLF MD differences were significantly higher from the other regions, whereas the ALIC, thalamus, and caudate had significantly lower MD values compared to all other studied regions. Confirming previous analysis, FA was lowest in the CST and highest in ALIC in comparison to other structures. The CST had significantly higher RD differences than all other studied regions, followed by the SLF and PLIC higher than 8 structures. Both deep gray matter structures had lower AD differences than those found in all WM tracts.

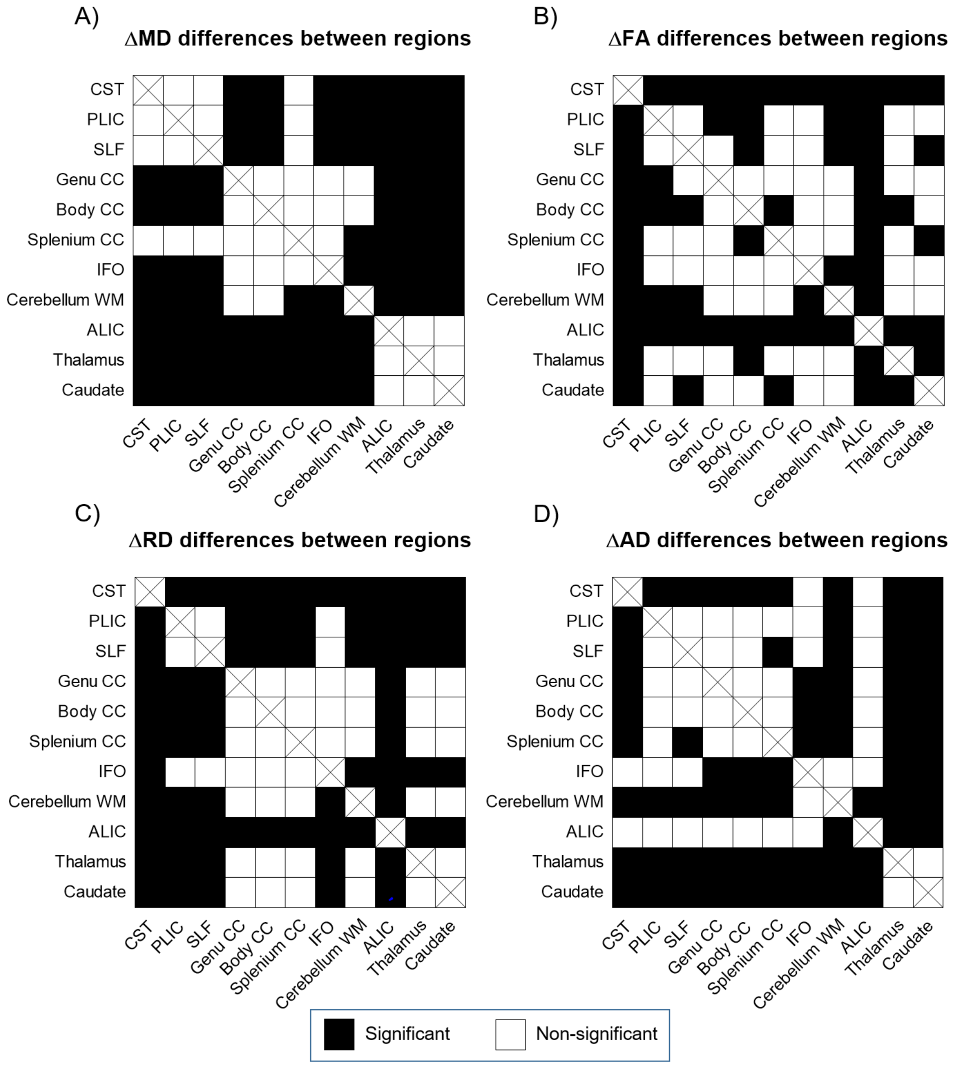
A) ΔMD differences between regions

B) ΔFA differences between regions

C) ΔRD differences between regions

D) ΔAD differences between regions

Figure 3.5: Cross table of OGSE - PGSE diffusion parameter differences showing significant differences between paired structures (using the Wilcoxon signed rank test [$p<0.5$]) in eight healthy subjects. A) Exclusive of one another, CST, PLIC, and SLF had significantly higher MD, while ALIC and both GM structures had the lowest, compared to all regions. B) FA in the CST had the lowest OGSE-PGSE differences. C) CST had the highest RD from all regions, next to SLF and PLIC in 8/10. D) Thalamus and caudate showed significantly lower AD than all studied WM tracts.

Normalized OGSE-PGSE % differences of diffusion metrics averaged across eight healthy subjects are presented in Figure 3.6 for the 9 white and 2 gray matter structures. Radial diffusivity showed the highest % increases of any of the diffusion parameters, namely 11.8%, 9.5%, 8.3%, and 7.6% for the CST, PLIC, SLF, and splenium CC, respectively. Similar findings were observed for MD in the same structures, with increments of 7.9% (CST), 7% (PLIC), 6.8% (SLF), and 5.8% (splenium). Axial diffusivity showed increases of up to 5.8% which were quite consistent across 8/9 white matter tracts, but was the least changed in the caudate, thalamus and IFO. FA showed minimal changes for most regions.

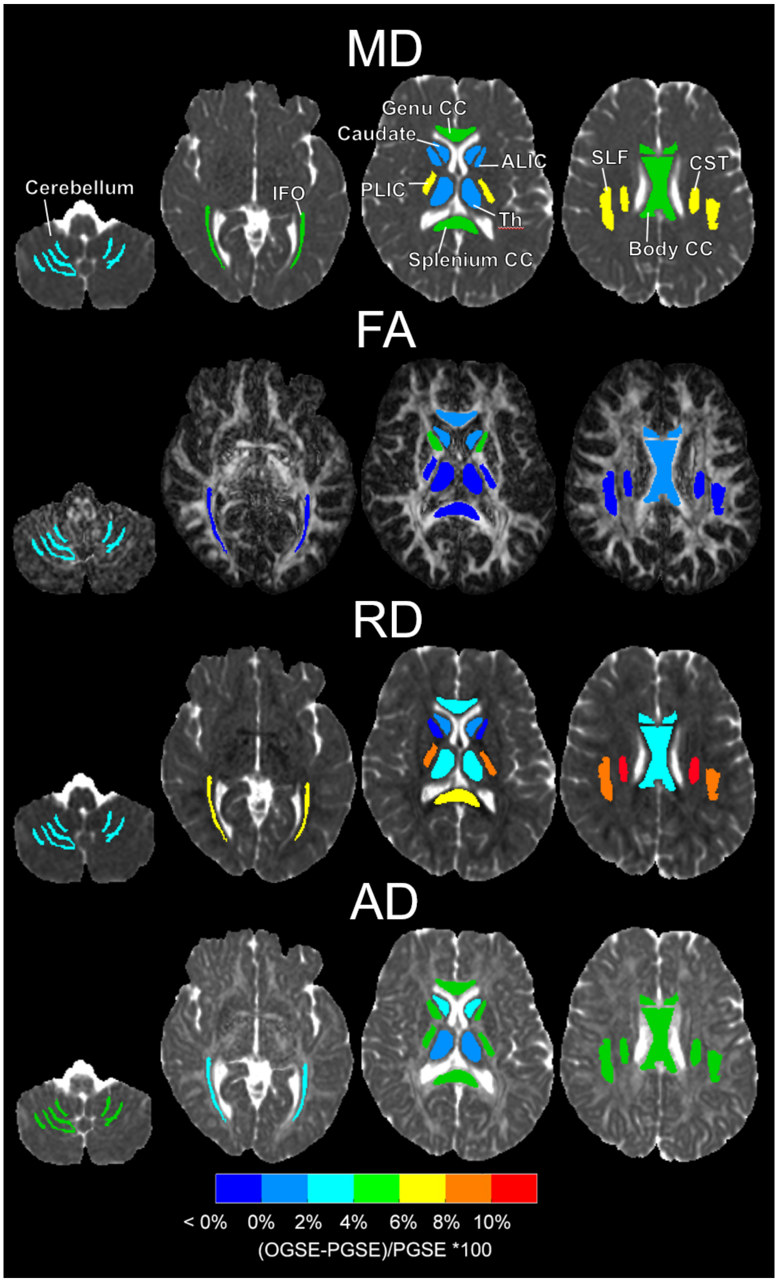

Figure 3.6: Pictorial representation of relative (%) OGSE- PGSE differences of diffusion metrics averaged (left and right combined for calculation) over eight healthy subjects for nine white matter regions and two deep gray matter structures , displayed in their corresponding maps. Radial diffusivity had the largest % increases of any of the diffusion metric, with the CST, PLIC, SLF, splenium CC, and IFO being the most evident. Similar to RD, mean diffusivity showed considerable increases in the CST, PLIC, and SLF of around 8% with the least changes in the deep gray mater. Axial diffusivity also showed notable increases of up to 6% with the lowest % changes in the two gray matter regions and the IFO. Note that data shown was normalized to PGSE FLAIR.

3.4 Discussion

The purpose of this study was to improve the ability to measure diffusion time effects with OGSE in the human brain by using CSF-suppression with FLAIR preparation and then to use this methodology to investigate differences in diffusion time sensitivity across various white matter tracts in the healthy young adult brain. Eliminating CSF signal on the b0 images with FLAIR minimized Gibbs ringing artifacts and improved the quantitative diffusion maps which is necessary to measure the small differences between OGSE and PGSE, by removing erroneous values which were most noticeable on MD in regions near CSF/brain interfaces. Using an OGSE frequency of 40 Hz, with an effective diffusion time of 5.1 ms compared to PGSE with 40 ms, a voxel-by-voxel subtraction of diffusion parameters showed OGSE-PGSE differences predominantly in white matter regions, but not in deep or cortical gray matter. The MD and RD diffusion-time dependences differed between tracts and was greatest for the corticospinal tract, posterior limb of the internal capsule, and the superior longitudinal fasciculus. Notably AD was elevated on OGSE for all 9 white matter tracts, with significantly higher OGSE-PGSE differences from those in both deep gray matter regions.

The previous OGSE human brain studies, albeit limited in numbers, all have evident Gibbs ringing artifacts in the ADC/MD maps shown in their publications – often seen as regions of abnormally low diffusivity at the brain/CSF interfaces [123] (e.g. see Figure 4 in Baron MRM 2014 [74], Figure 6 in Van MRM 2014 [73] Figure 1 Boonrod Neurorad 2018 [90], Figure 1C,D Maekawa MRI 2019 [92], Figures 2, 5, and 7 Arbabi MRM 2019 [93]). While this may be less of an issue when examining OGSE vs PGSE in ischemic lesions or tumours with large diffusion time effects, these quantitative parameter errors will deleteriously impact white matter studies which have much smaller diffusion time effects. Early implementation of OGSE here on a state-of-the-art Siemens Prisma 3T (relative to our earlier healthy white matter study on a Varian Inova 4.7T [74]) also showed these problematic Gibbs ringing artifacts, prompting the current FLAIR strategy. It should be noted that the FA or color-encoded FA maps do not demonstrate these artifacts as readily (as seen in Figure 3.1), and thus examination of the other diffusion parameter maps is necessary. Recent publications have proposed strategies to remove Gibbs ringing artifacts in post-processing of the output images (i.e. not on the raw k-space), but these did not entirely alleviate these errors either for the case of non-interpolated nor interpolated data (i.e. Figures 2.16 and 2.17 in Chapter 2 of this thesis, respectively). In fact, these regions of incorrect low diffusion are still evident after Gibbs ringing correction when 6/8 partial Fourier is used in acquisition (see Figure 6 in Kellner MRM 2016 [105]), as is commonly done like in this study (note: non-interpolated data was not acquired in the group of 8 subjects). CSF suppression with FLAIR removes these quantitative diffusion artifacts in acquisition by providing the same contrast between CSF spaces and the brain on both non-diffusion-weighted (b0) and diffusion-weighted (b500) images. The limitation with FLAIR of course is the reduced SNR in the brain tissue and the longer scan time to allow for the inversion recovery. Nonetheless the scan time of 5.5 min for the whole brain FLAIR PGSE is reasonable, and the much longer 11 min scan time for the whole brain FLAIR OGSE was driven mainly by vendor-set hard limits for a very much longer minimum TR of 27 sec (versus 13 sec in FLAIR PGSE) presumably to minimize gradient duty cycle and heating. The overall long scan time would limit the application of the FLAIR OGSE/PGSE pair to clinical populations, although scan times could be reduced by limiting slice coverage and determining strategies to reduce TR for the OGSE. The current study is the first time FLAIR has been incorporated into OGSE acquisition and a higher b-value of $b=$ 500 s/mm^2 (relative to previous studies at $b=$ 200 s/mm^2 [73], 300 s/mm^2 [74], 400 s/mm^2 [89], or 450 s/mm^2 [93]) was used for greater diffusion sensitivity.

Using a higher frequency of 50 Hz (and shorter effective shorter diffusion time of 4 ms), a previous healthy human brain study reported much larger

OGSE – PGSE differences of 8-20% for AD (i.e. $\lambda_{\|}$) and 13-40% for RD (i.e. $\lambda_{\perp}$) in 7/8 white matter tracts identified with tractography [74], with the exception being the body of the corpus callosum. The rank order of RD increases with OGSE in that study was 30-40% (genu and splenium of corpus callosum, superior longitudinal fasciculus), 20-30% (corticospinal tract, inferior longitudinal fasciculus), and then 10-20% (inferior fronto-occipital fasciculus, cingulum). Here, using 40 Hz OGSE, only 4/9 white matter regions showed increased RD by 7-12%, namely the CST, SLF, PLIC, and IFO. However, all 9 white matter regions showed elevated MD (2-8%), mainly due to the fact that AD was elevated (3-6%) with OGSE in all white matter regions. FA on the other hand did not differ between OGSE and PGSE for 6/8 regions suggesting proportional AD and RD changes, but FA went down for the CST and up for the ALIC given differential changes in AD and RD with diffusion time. Of the six regions that overlapped between the two studies, 3/6 showed RD increases in both studies (SLF, CST, IFO), 1/6 did not show RD increases in both (body CC), whereas the genu and splenium of the corpus callosum regions showed RD increases in the previous 50 Hz work but no RD changes with the current 40 Hz. That said, the genu and splenium of the corpus callosum did show marked diffusion time effects for AD in both studies. The proportional changes were much less in the current study, but it is unclear if such differences are related to the lower OGSE frequency here, or whether CSF artifacts (Gibbs ringing, pulsatility, partial volume) had any influence in the earlier work.

Further studies are needed to examine higher OGSE frequencies while avoiding Gibbs ringing artifacts. Notably the two deep gray matter regions of the thalamus and caudate showed no diffusion time dependencies for MD, FA or AD, but the thalamus did show an elevated RD although it was only by ~0.01×10^{-3} mm^2/s between OGSE and PGSE. The earlier 4.7T human study showed elevations of RD and AD in the thalamus with OGSE [74]. There are few pre-clinical OGSE studies of the healthy brain white matter, but one study on excised, fixed mouse brain showed elevated MD (ADC), AD, and RD with

OGSE frequency (show 50 Hz and up) in the genu and splenium of the corpus callosum, and the cerebellar peduncles [81]; note that our study also shows elevated MD and AD in the cerebellum WM. An in vivo rat brain study has also shown diffusion time differences in cerebellar WM and CC [82]. However, much of the focus in the pre-clinical studies has been on gray matter.

It has long been known that the alteration of the diffusion time can be used to examine cell size and barrier separations [125]. For ordered axonal systems, the slope of change of RD (i.e. perpendicular diffusivity) with shorter diffusion time, given by higher OGSE frequency, is greater with larger axon diameters in excised rat spinal cord [86, 89]. Thus, the white matter tracts with the greatest OGSE RD – PGSE RD changes would presumably be expected to have the largest axons of those tracts examined. The CST/PLIC and SLF showed the greatest RD increase at the shorter diffusion time, where histological studies indicate the presence of large diameter axons: CST is composed of 90% 1 – 4 μm, 7% 5 – 10 μm, and 3% 10 – 22 μm axon diameters [126], while the axons in SLF are ~0.63 – 1.34 μm [127] in diameter. The OGSE-PGSE RD findings agree with a high b connectome study in healthy adults that has reported a larger axon diameter index in the corticospinal tract compared to adjacent white matter tracts [122]. A multiple contrast MRI study in healthy adults showed higher values of magnetization transfer ratio, quantitative susceptibility mapping, myelin water fraction, FA, mean kurtosis, and intra-cellular volume fraction along the CST (relative to frontal white matter) reflecting thicker myelin sheaths and tightly packed and larger fibres [128]. In our study, only 4/9 white matter tracts (CST/PLIC/SLF/IFO) showed significant differences of OGSE 40 Hz - PGSE RD, perhaps due to the lack of sensitivity to small axons in the other tracts suggesting the need for shorter diffusion times with higher OGSE frequency [78, 129]. Higher frequencies such as 50 Hz and 60 Hz will be attempted in future using similar FLAIR preparation - as shown previously in Chapter 2 (Figure 2.10) to be feasible with decent MD map quality, but they have the challenge of imparting greater TE for a given b-value; even higher frequencies would be very challenging given hardware limitations on a clinical scanner resulting in unreasonably long TE and low SNR. In contrast to limited tracts with RD OGSE changes, axial diffusivity was elevated on short diffusion time OGSE in all 9 WM tracts examined, agreeing with previous work showing AD diffusion time dependency over much longer diffusion times (i.e. 45-600 ms) in stimulated echo DTI studies of healthy human brain [130]. Certainly the length scales are longer along the length of the axons, regardless of the axon diameter, making the axial/longitudinal diffusivity measurement more sensitive to diffusion time differences that have been interpreted in that paper to be present due to short-range disorder along the axon length (e.g. undulating axonal membranes – see Figure 5B in Alexander DC NMR Biomed 2017 [131]).

3.5 Conclusions

Oscillating gradient spin-echo FLAIR acquisitions have proven to eliminate problematic Gibbs ringing artifacts *a priori* in the acquisition process, allowing the estimation of diffusion metrics that unveiled potential micro-scale tissue differences at reduced diffusion times. Although challenging to acquire, the OGSE technique remains a promising tool to study healthy brain microstructure and the mechanisms of disease.

4 | Conclusions

Molecular water diffusion provides an additional non-invasive tool to improve our understanding of human brain anatomy and physiology *in vivo*. By varying the time allowed for molecules to diffuse and measuring key diffusion parameters, one can infer micro-scale tissue properties. The oscillating gradient spin echo (OGSE) diffusion sequence enables shorter effective diffusion times than its counterpart pulsed gradient spin echo (PGSE), effectively providing a means to discriminate between small and large axon diameters. The conducted work outlined in this thesis was centered on unveiling these small OGSE-PGSE differences in human brain at 3T by imaging at short diffusion times.

As discussed in Chapter 2, constrained by hardware limitations, the implementation of high OGSE frequencies on our current 3T system was challenging, explaining still the limited number of healthy human brain studies by four independent groups [73, 74, 89, 93]. Penalized by long scanning times and very low signal, images with OGSE frequencies of f>60 Hz were infeasible to acquire. Nonetheless, after several iterated experiments, an optimization of scanning parameters led to higher-quality diffusion images and derived maps for f= 40 - 50 Hz, where mean diffusivity (MD) values showed increments for the OSGE acquisitions relative to PGSE in several white matter tracts, as expected with the differences in diffusion time.

Visual inspection of the data revealed the presence of Gibbs ringing (GR), an image artifact that would compromise the accurate estimation of diffusion parameters across multiple brain regions, such as by introducing artificially low MD values near CSF ventricular spaces. Therefore, it became a priority to eradicate the artifact and obtain homogeneous MD maps, since the expected OGSE-PGSE differences would likely be masked under these low MD regions. Attempts were made to correct for GR with conventional GR removal methods (i.e. TV and sub-voxel shifts), however they both failed to eliminate the artifact entirely.

In search of a solution, Chapter 3 examined the application of fluid-attenuated inversion recovery (FLAIR) – a sequence widely used to attenuate the bright signal from cerebrospinal fluid (CSF) – as an addition to the imaging protocol discussed herein and was found to effectively avoid the detrimental GR artifact from the start, as it suppressed the steep signal intensity transitions at CSF/tissue interfaces seen in the non-diffusion weighted images (and on a smaller scale in diffusion-weighted images) that originated the ringing. Image quality increased considerably with FLAIR, however at the cost of nearly double the scan time.

With a substantial improvement in image quality and derived OGSE/PGSE diffusion maps, the FLAIR method was used to better investigate OGSE-PGSE differences between brain regions in a small sample of healthy young adults (n=8). The findings included significant elevations of mean and radial diffusivities in the corticospinal tract, superior longitudinal fasciculus, and posterior limb of the internal capsule, among others, in OGSE-PGSE difference maps. As expected, the results obtained through this method were in agreement with previous histological and scientific literature that indicate larger axons in these regions.

In brief, FLAIR was found to be extremely effective but not time-efficient, in avoiding the formation of GR. Therefore, it is recommended to implement the use of FLAIR as a GR prevention method taking into consideration its time limitation.

As for future directions, further hardware advancements in human scanners (such as increased gradient strength) are necessary in order to explore molecular water displacements within shorter time-scales using oscillating gradients. Furthermore, the OGSE method should be applied in a larger sample size to investigate potential axon diameter differences with demographics, such as age and sex, as these factors could highlight microstructural distinctions between groups. Additional OGSE human brain studies are necessary overall to explore changes in diffusion processes beyond ischemic stroke, as these OGSE-PGSE differences could act as a potential biomarker and shed light upon other neurological disorders and disease mechanisms such as multiple sclerosis, benign and malignant tumors, and brain injury.

References

[1] R. Brown, "Xxvii. a brief account of microscopical observations made in the months of june, july and august 1827, on the particles contained in the pollen of plants; and on the general existence of active molecules in organic and inorganic bodies," *The Philosophical Magazine*, vol. 4, no. 21, pp. 161–173, 1828. 2

[2] A. Einstein, "Über die von der molekularkinetischen theorie der wärme geforderte bewegung von in ruhenden flüssigkeiten suspendierten teilchen," *Annalen Der Physik*, vol. 322, no. 8, pp. 549–560, 1905. 3

[3] E. L. Hahn, "Spin echoes," *Physical Review*, vol. 80, no. 4, p. 580, 1950. 3, 4

[4] H. Y. Carr and E. M. Purcell, "Effects of diffusion on free precession in nuclear magnetic resonance experiments," *Physical Review*, vol. 94, no. 3, p. 630, 1954. 3

[5] H. C. Torrey, "Bloch equations with diffusion terms," *Physical Review*, vol. 104, no. 3, p. 563, 1956. 3

[6] I. Edelman and J. Leibman, "Anatomy of body water and electrolytes," *The American Journal of Medicine*, vol. 27, no. 2, pp. 256–277, 1959. 4

[7] E. O. Stejskal and J. E. Tanner, "Spin diffusion measurements: Spin echoes in the presence of a time-dependent field gradient," *The Journal of Chemical Physics*, vol. 42, no. 1, pp. 288–292, 1965. 4, 6

[8] D. M. Patterson, A. R. Padhani, and D. J. Collins, "Technology insight: Water diffusion mri—a potential new biomarker of response to cancer therapy," *Nature Reviews Clinical Oncology*, vol. 5, no. 4, p. 220, 2008. 5

[9] G. E. Wesbey, M. E. Moseley, and R. L. Ehman, "Translational molecular self-diffusion in magnetic resonance imaging. ii. measurement of the self-diffusion coefficient.," *Investigative Radiology*, vol. 19, no. 6, pp. 491–498, 1984. 6

[10] D. Taylor and M. Bushell, "The spatial mapping of translational diffusion coefficients by the nmr imaging technique," *Physics in Medicine & Biology*, vol. 30, no. 4, p. 345, 1985. 6

[11] D. Le Bihan, E. Breton, D. Lallemand, P. Grenier, E. Cabanis, and M. Laval-Jeantet, “Mr imaging of intravoxel incoherent motions: Application to diffusion and perfusion in neurologic disorders.,” *Radiology*, vol. 161, no. 2, pp. 401–407, 1986. 9

[12] D. Le Bihan, E. Breton, D. Lallemand, M. Aubin, J. Vignaud, and M. Laval-Jeantet, “Separation of diffusion and perfusion in intravoxel incoherent motion mr imaging.,” *Radiology*, vol. 168, no. 2, pp. 497–505, 1988. 9

[13] C. Thomsen, O. Henriksen, and P. Ring, “In vivo measurement of water self diffusion in the human brain by magnetic resonance imaging,” *Acta Radiologica*, vol. 28, no. 3, pp. 353–361, 1987. 10

[14] M. E. Moseley, Y. Cohen, J. Kucharczyk, J. Mintorovitch, H. Asgari, M. Wendland, J. Tsuruda, and D. Norman, “Diffusion-weighted mr imaging of anisotropic water diffusion in cat central nervous system.,” *Radiology*, vol. 176, no. 2, pp. 439–445, 1990. 10, 13

[15] T. L. Chenevert, J. A. Brunberg, and J. G. Pipe, “Anisotropic diffusion in human white matter: Demonstration with mr techniques in vivo.,” *Radiology*, vol. 177, no. 2, pp. 401–405, 1990. 10

[16] M. E. Moseley, J. Kucharczyk, H. S. Asgari, and D. Norman, “Anisotropy in diffusion-weighted mri,” *Magnetic Resonance in Medicine*, vol. 19, no. 2, pp. 321–326, 1991. 11, 13

[17] C. Beaulieu, “The basis of anisotropic water diffusion in the nervous system–a technical review,” *NMR in Biomedicine*, vol. 15, no. 7-8, pp. 435–455, 2002. 11, 13, 26

[18] C. Beaulieu and P. S. Allen, “Determinants of anisotropic water diffusion in nerves,” *Magnetic Resonance in Medicine*, vol. 31, no. 4, pp. 394–400, 1994. 11, 13

[19] C. Beaulieu and P. Allen, “Water diffusion in the giant axon of the squid: Implications for diffusion-weighted MRI of the nervous system,” *Magnetic Resonance in Medicine*, vol. 32, no. 5, pp. 579–583, 1994. 11

[20] P. Basser, J. Mattiello, and D. LeBihan, *Estimation of the Effective Self-Diffusion Tensor from the NMR Spin Echo*, 1994. 13–15

[21] L. Garrido, V. J. Wedeen, K. K. Kwong, U. M. Spencer, and H. L. Kantor, “Anisotropy of water diffusion in the myocardium of the rat.,” *Circulation Research*, vol. 74, no. 5, pp. 789–793, 1994. 13

[22] G. Cleveland, D. Chang, C. Hazlewood, and H. Rorschach, “Nuclear magnetic resonance measurement of skeletal muscle: Anisotrophy of the diffusion coefficient of the intracellular water,” *Biophysical journal*, vol. 16, no. 9, pp. 1043–1053, 1976. 13

[23] P. J. Basser, J. Mattiello, and D. LeBihan, "MR diffusion tensor spectroscopy and imaging," *Biophysical Journal*, vol. 66, no. 1, pp. 259–267, 1994. 13, 16, 17

[24] J. Mattiello, P. J. Basser, and D. LeBihan, "Analytical expressions for the b matrix in nmr diffusion imaging and spectroscopy," *Journal of magnetic resonance, Series A*, vol. 108, no. 2, pp. 131–141, 1994. 14

[25] D. Jones, *Diffusion MRI: Theory, Methods, and Applications*. OUP USA, 2011, ISBN: 9780195369779. 14, 26, 45

[26] P. J. Basser and C. Pierpaoli, "A simplified method to measure the diffusion tensor from seven mr images," *Magnetic Resonance in Medicine*, vol. 39, no. 6, pp. 928–934, 1998. 15

[27] D. K. Jones, M. A. Horsfield, and A. Simmons, "Optimal strategies for measuring diffusion in anisotropic systems by magnetic resonance imaging," *Magnetic Resonance in Medicine: An Official Journal of the International Society for Magnetic Resonance in Medicine*, vol. 42, no. 3, pp. 515–525, 1999. 15, 41

[28] P. J. Basser, "Inferring microstructural features and the physiological state of tissues from diffusion-weighted images," *NMR in Biomedicine*, vol. 8, no. 7, pp. 333–344, 1995. 15, 18

[29] C. Pierpaoli, P. Jezzard, P. J. Basser, A. Barnett, and G. Di Chiro, "Diffusion tensor mr imaging of the human brain.," *Radiology*, vol. 201, no. 3, pp. 637–648, 1996. 16

[30] P. B. Kingsley, "Introduction to diffusion tensor imaging mathematics: Part i. tensors, rotations, and eigenvectors," *Concepts in Magnetic Resonance Part A*, vol. 28, no. 2, pp. 101–122, 2006. 17

[31] H. Johansen-Berg and T. E. Behrens, *Diffusion MRI: from quantitative measurement to in vivo neuroanatomy*. Academic Press, 2013. 19

[32] S. Pajevic and C. Pierpaoli, "Color schemes to represent the orientation of anisotropic tissues from diffusion tensor data: Application to white matter fiber tract mapping in the human brain," *Magnetic Resonance in Medicine*, vol. 42, no. 3, pp. 526–540, 1999. 21

[33] S. Mori, B. J. Crain, V. P. Chacko, and P. C. Van Zijl, "Three-dimensional tracking of axonal projections in the brain by magnetic resonance imaging," *Annals of Neurology*, vol. 45, no. 2, pp. 265–269, 1999. 22

[34] D. K. Jones, A. Simmons, S. C. Williams, and M. A. Horsfield, "Non-invasive assessment of axonal fiber connectivity in the human brain via diffusion tensor mri," *Magnetic Resonance in Medicine*, vol. 42, no. 1, pp. 37–41, 1999. 22

[35] T. E. Conturo, N. F. Lori, T. S. Cull, E. Akbudak, A. Z. Snyder, J. S. Shimony, R. C. McKinstry, H. Burton, and M. E. Raichle, "Tracking neuronal fiber pathways in the living human brain," *Proceedings of the National Academy of Sciences*, vol. 96, no. 18, pp. 10 422–10 427, 1999. 22

[36] P. J. Basser, S. Pajevic, C. Pierpaoli, J. Duda, and A. Aldroubi, "In vivo fiber tractography using dt-mri data," *Magnetic Resonance in Medicine*, vol. 44, no. 4, pp. 625–632, 2000. 22

[37] J.-D. Tournier, S. Mori, and A. Leemans, "Diffusion tensor imaging and beyond," *Magnetic Resonance in Medicine*, vol. 65, no. 6, pp. 1532–1556, 2011. 22, 23, 27, 67

[38] Y. A. Bhagat and C. Beaulieu, "Diffusion anisotropy in subcortical white matter and cortical gray matter: Changes with aging and the role of csf-suppression," *Journal of Magnetic Resonance Imaging: An Official Journal of the International Society for Magnetic Resonance in Medicine*, vol. 20, no. 2, pp. 216–227, 2004. 24, 72

[39] C. Lebel, S. Caverhill-Godkewitsch, and C. Beaulieu, "Age-related regional variations of the corpus callosum identified by diffusion tensor tractography," *NeuroImage*, vol. 52, no. 1, pp. 20–31, 2010. 24

[40] L. Snook, L.-A. Paulson, D. Roy, L. Phillips, and C. Beaulieu, "Diffusion tensor imaging of neurodevelopment in children and young adults," *NeuroImage*, vol. 26, no. 4, pp. 1164–1173, 2005. 24

[41] D. Qiu, L.-H. Tan, K. Zhou, and P.-L. Khong, "Diffusion tensor imaging of normal white matter maturation from late childhood to young adulthood: Voxel-wise evaluation of mean diffusivity, fractional anisotropy, radial and axial diffusivities, and correlation with reading development," *NeuroImage*, vol. 41, no. 2, pp. 223–232, 2008. 24

[42] D. Salat, D. Tuch, N. Hevelone, B. Fischl, S. Corkin, H. Rosas, and A. Dale, "Age-related changes in prefrontal white matter measured by diffusion tensor imaging," *Annals of the New York Academy of Sciences*, vol. 1064, no. 1, pp. 37–49, 2005. 24

[43] D. J. Madden, I. J. Bennett, and A. W. Song, "Cerebral white matter integrity and cognitive aging: Contributions from diffusion tensor imaging," *Neuropsychology Review*, vol. 19, no. 4, p. 415, 2009. 24

[44] L. Bello, A. Gambini, A. Castellano, G. Carrabba, F. Acerbi, E. Fava, C. Giussani, M. Cadioli, V. Blasi, A. Casarotti, *et al.*, "Motor and language dti fiber tracking combined with intraoperative subcortical mapping for surgical removal of gliomas," *NeuroImage*, vol. 39, no. 1, pp. 369–382, 2008. 25

[45] F. Vassal, F. Schneider, and C. Nuti, “Intraoperative use of diffusion tensor imaging-based tractography for resection of gliomas located near the pyramidal tract: Comparison with subcortical stimulation mapping and contribution to surgical outcomes,” *British Journal of Neurosurgery*, vol. 27, no. 5, pp. 668–675, 2013. 25

[46] F. Vassal, F. Schneider, A. Sontheimer, J.-J. Lemaire, and C. Nuti, “Intraoperative visualisation of language fascicles by diffusion tensor imaging-based tractography in glioma surgery,” *Acta Neurochirurgica*, vol. 155, no. 3, pp. 437–448, 2013. 25

[47] C. H. Sotak, “The role of diffusion tensor imaging in the evaluation of ischemic brain injury–a review,” *NMR in Biomedicine*, vol. 15, no. 7-8, pp. 561–569, 2002. 25

[48] C. A. Baron, M. Kate, L. Gioia, K. Butcher, D. Emery, M. Budde, and C. Beaulieu, “Reduction of Diffusion-Weighted Imaging Contrast of Acute Ischemic Stroke at Short Diffusion Times,” *Stroke; A Journal of Cerebral Circulation*, vol. 46, no. 8, pp. 2136–2141, 2015. 25, 37, 75

[49] Y. A. Bhagat, M. S. Hussain, R. W. Stobbe, K. S. Butcher, D. J. Emery, A. Shuaib, M. M. Siddiqui, P. Maheshwari, F. Al-Hussain, and C. Beaulieu, “Elevations of diffusion anisotropy are associated with hyper-acute stroke: A serial imaging study,” *Magnetic Resonance Imaging*, vol. 26, no. 5, pp. 683–693, 2008. 25

[50] Y. J. Hong, B. Yoon, S.-C. Lim, Y. S. Shim, J.-Y. Kim, K. J. Ahn, I.-W. Han, and D. W. Yang, “Microstructural changes in the hippocampus and posterior cingulate in mild cognitive impairment and alzheimer’s disease: A diffusion tensor imaging study,” *Neurological Sciences*, vol. 34, no. 7, pp. 1215–1221, 2013. 25

[51] G. Stebbins and C. Murphy, “Diffusion tensor imaging in alzheimer’s disease and mild cognitive impairment,” *Behavioural Neurology*, vol. 21, no. 1, 2, pp. 39–49, 2009. 25

[52] T. M. Nir, N. Jahanshad, J. E. Villalon-Reina, A. W. Toga, C. R. Jack, M. W. Weiner, P. M. Thompson, A. D. N. I. (ADNI, *et al.*, “Effectiveness of regional dti measures in distinguishing alzheimer’s disease, mci, and normal aging,” *NeuroImage: Clinical*, vol. 3, pp. 180–195, 2013. 25

[53] R. McKavanagh, M. Torso, M. Jenkinson, J. Kolasinski, C. J. Stagg, M. M. Esiri, J. A. McNab, H. Johansen-Berg, K. L. Miller, and S. A. Chance, “Relating diffusion tensor imaging measurements to microstructural quantities in the cerebral cortex in multiple sclerosis,” *Human Brain Mapping*, 2019. 25

[54] R. Woitek, F. Leutmezer, A. Dal-Bianco, J. Furtner, G. Kasprian, D. Prayer, and V. Schöpf, “Diffusion tensor imaging of the normal-appearing deep gray matter in primary and secondary progressive multiple sclerosis,” *Acta Radiologica*, p. 0 284 185 119 852 735, 2019. 25

[55] K. C. Atkinson, J. B. Lee, A. J. Khalaj, J. P. Hasselmann, S. H. Kim, A. Drew, J. Soto, J. A. Katzenellenbogen, N. G. Harris, A. Obenaus, *et al.*, "Diffusion tensor imaging identifies aspects of therapeutic estrogen receptor β ligand-induced remyelination in a mouse model of multiple sclerosis," *Neurobiology of Disease*, p. 104 501, 2019. 25

[56] D. W. Gross, L. Concha, and C. Beaulieu, "Extratemporal white matter abnormalities in mesial temporal lobe epilepsy demonstrated with diffusion tensor imaging," *Epilepsia*, vol. 47, no. 8, pp. 1360–1363, 2006. 25

[57] V. Pozorski, J. M. Oh, N. Adluru, A. P. Merluzzi, F. Theisen, O. Okonkwo, A. Barzgari, S. Krislov, J. Sojkova, B. B. Bendlin, *et al.*, "Longitudinal white matter microstructural change in parkinson's disease," *Human Brain Mapping*, vol. 39, no. 10, pp. 4150–4161, 2018. 25

[58] F. Theisen, R. Leda, V. Pozorski, J. M. Oh, N. Adluru, R. Wong, O. Okonkwo, D. C. Dean III, B. B. Bendlin, S. C. Johnson, *et al.*, "Evaluation of striatonigral connectivity using probabilistic tractography in parkinson's disease," *NeuroImage: Clinical*, vol. 16, pp. 557–563, 2017. 25

[59] S. Mori and J. Zhang, "Principles of diffusion tensor imaging and its applications to basic neuroscience research," *Neuron*, vol. 51, no. 5, pp. 527–539, 2006. 26

[60] S. G. Waxman, J. D. Kocsis, P. K. Stys, *et al.*, *The axon: structure, function, and pathophysiology.* Oxford University Press, USA, 1995. 27

[61] T. Niendorf, D. G. Norris, and D. Leibfritz, "Detection of apparent restricted diffusion in healthy rat brain at short diffusion times," *Magnetic Resonance in Medicine*, vol. 32, no. 5, pp. 672–677, 1994. 28

[62] C. Beaulieu, M. D. Does, R. E. Snyder, and P. S. Allen, "Changes in water diffusion due to wallerian degeneration in peripheral nerve," *Magnetic Resonance in Medicine*, vol. 36, no. 4, pp. 627–631, 1996. 28

[63] Y. SEo, Y. Morita, Y. Kusaka, M. C. Steward, and M. Murakami, "Diffusion of water in rat sciatic nerve measured by 1h pulsed field gradient nmr: Compartmentation and anisotropy," *The Japanese Journal of Physiology*, vol. 46, no. 2, pp. 163–169, 1996. 28

[64] G. J. Stanisz and R. M. Henkelman, "Diffusional anisotropy of t2 components in bovine optic nerve," *Magnetic Resonance in Medicine*, vol. 40, no. 3, pp. 405–410, 1998. 28

[65] B. Gross and R. Kosfeld, "Anwendung der spin-echo-methode der messung der selbstdiffusion," *Messtechnik*, vol. 77, pp. 171–177, 1969. 29

[66] J. Stepišnik, "Analysis of nmr self-diffusion measurements by a density matrix calculation," *Physica B+ C*, vol. 104, no. 3, pp. 350–364, 1981. 29

[67] P. T. Callaghan and J. Stepišnik, "Generalized analysis of motion using magnetic field gradients," in *Advances in magnetic and optical resonance*, vol. 19, Elsevier, 1996, pp. 325–388. 29

[68] M. D. Does, E. C. Parsons, and J. C. Gore, "Oscillating gradient measurements of water diffusion in normal and globally ischemic rat brain," *Magnetic Resonance in Medicine*, vol. 49, no. 2, pp. 206–215, 2003. 29, 31, 35, 36, 75

[69] E. C. Parsons, M. D. Does, and J. C. Gore, "Modified oscillating gradient pulses for direct sampling of the diffusion spectrum suitable for imaging sequences," *Magnetic Resonance Imaging*, vol. 21, no. 3-4, pp. 279–285, 2003. 29–31

[70] J. Xu, M. D. Does, and J. C. Gore, "Sensitivity of mr diffusion measurements to variations in intracellular structure: Effects of nuclear size," *Magnetic Resonance in Medicine*, vol. 61, no. 4, pp. 828–833, 2009. 30

[71] I. Drobnjak, B. Siow, and D. C. Alexander, "Optimizing gradient waveforms for microstructure sensitivity in diffusion-weighted mr," *Journal of Magnetic Resonance*, vol. 206, no. 1, pp. 41–51, 2010. 30, 75

[72] J. C. Gore, J. Xu, D. C. Colvin, T. E. Yankeelov, E. C. Parsons, and M. D. Does, "Characterization of tissue structure at varying length scales using temporal diffusion spectroscopy," *NMR in Biomedicine*, vol. 23, no. 7, pp. 745–756, 2010. 30, 31, 33, 34, 75

[73] A. T. Van, S. J. Holdsworth, and R. Bammer, "In vivo investigation of restricted diffusion in the human brain with optimized oscillating diffusion gradient encoding," *Magnetic Resonance in Medicine*, vol. 71, no. 1, pp. 83–94, 2014. 31, 32, 37, 75, 88, 89, 93

[74] C. A. Baron and C. Beaulieu, "Oscillating gradient spin-echo (OGSE) diffusion tensor imaging of the human brain," *Magnetic Resonance in Medicine*, vol. 72, no. 3, pp. 726–736, 2014. 31, 37, 40, 60–62, 75, 76

[75] K. R. Minard, "Spectral analysis of molecular diffusion in heterogeneous systems using pulsed gradient nmr," PhD thesis, Rice University, 1995. 32

[76] M. Schachter, M. D. Does, A. W. Anderson, and J. C. Gore, "Measurements of Restricted Diffusion Using an Oscillating Gradient Spin-Echo Sequence," *Journal of Magnetic Resonance*, vol. 147, no. 2, pp. 232–237, 2000. 33, 35, 75

[77] J. Xu, M. D. Does, and J. C. Gore, "Quantitative characterization of tissue microstructure with temporal diffusion spectroscopy," *Journal of Magnetic Resonance*, vol. 200, no. 2, pp. 189–197, 2009. 34

[78] I. Drobnjak, H. Zhang, A. Ianuş, E. Kaden, and D. C. Alexander, "Pgse, ogse, and sensitivity to axon diameter in diffusion mri: Insight from a simulation study," *Magnetic Resonance in Medicine*, vol. 75, no. 2, pp. 688–700, 2016. 35, 75, 91

[79] D. C. Colvin, T. E. Yankeelov, M. D. Does, Z. Yue, C. Quarles, and J. C. Gore, "New insights into tumor microstructure using temporal diffusion spectroscopy," *Cancer Research*, vol. 68, no. 14, pp. 5941–5947, 2008. 35, 36

[80] D. C. Colvin, M. E. Loveless, M. D. Does, Z. Yue, T. E. Yankeelov, and J. C. Gore, "Earlier detection of tumor treatment response using magnetic resonance diffusion imaging with oscillating gradients," *Magnetic Resonance Imaging*, vol. 29, no. 3, pp. 315–323, 2011. 35, 36, 75

[81] M. Aggarwal, M. V. Jones, P. A. Calabresi, S. Mori, and J. Zhang, "Probing mouse brain microstructure using oscillating gradient diffusion MRI," *Magnetic Resonance in Medicine*, vol. 67, no. 1, pp. 98–109, 2012. 35, 36, 39, 75, 91

[82] J. Kershaw, C. Leuze, I. Aoki, T. Obata, I. Kanno, H. Ito, Y. Yamaguchi, and H. Handa, "Systematic changes to the apparent diffusion tensor of in vivo rat brain measured with an oscillating-gradient spin-echo sequence," *NeuroImage*, vol. 70, pp. 10–20, 2013. 35, 36, 75, 91

[83] S. Portnoy, J. J. Flint, S. J. Blackband, and G. J. Stanisz, "Oscillating and pulsed gradient diffusion magnetic resonance microscopy over an extended b-value range: Implications for the characterization of tissue microstructure," *Magnetic Resonance in Medicine*, vol. 69, no. 4, pp. 1131–1145, 2013. 35, 36, 75

[84] N. Pyatigorskaya, D. Le Bihan, O. Reynaud, and L. Ciobanu, "Relationship between the diffusion time and the diffusion MRI signal observed at 17.2 tesla in the healthy rat brain cortex," *Magnetic Resonance in Medicine*, vol. 72, no. 2, pp. 492–500, 2014. 35, 36, 75

[85] D. Wu, L. J. Martin, F. J. Northington, and J. Zhang, "Oscillating gradient diffusion MRI reveals unique microstructural information in normal and hypoxia-ischemia injured mouse brains.," *Magnetic Resonance in Medicine*, vol. 72, no. 5, pp. 1366–74, 2014. 35, 36

[86] J. Xu, H. Li, K. D. Harkins, X. Jiang, J. Xie, H. Kang, M. D. Does, and J. C. Gore, "Mapping mean axon diameter and axonal volume fraction by mri using temporal diffusion spectroscopy," *NeuroImage*, vol. 103, pp. 10–19, 2014. 35, 36, 91

[87] D. Wu and J. Zhang, "The Effect of Microcirculatory Flow on Oscillating Gradient Diffusion MRI and Diffusion Encoding with Dual-Frequency Orthogonal Gradients (DEFOG)," *Magnetic Resonance in Medicine*, vol. 77, no. 4, pp. 1583–1592, 2017. 35, 36

[88] A. Bongers, E. Hau, and H. Shen, "Short Diffusion Time Diffusion-Weighted Imaging With Oscillating Gradient Preparation as an Early Magnetic Resonance Imaging Biomarker for Radiation Therapy Response Monitoring in Glioblastoma: A Preclinical Feasibility Study," *International Journal of Radiation Oncology Biology Physics*, vol. 102, no. 4, pp. 1014–1023, 2018. 35, 36, 75

[89] J. Xu, H. Li, K. Li, K. D. Harkins, X. Jiang, J. Xie, H. Kang, R. D. Dortch, A. W. Anderson, M. D. Does, *et al.*, "Fast and simplified mapping of mean axon diameter using temporal diffusion spectroscopy," *NMR in Biomedicine*, vol. 29, no. 4, pp. 400–410, 2016. 37, 75, 89, 91, 93

[90] A. Boonrod, A. Hagiwara, M. Hori, I. Fukunaga, C. Andica, T. Maekawa, and S. Aoki, "Reduced visualization of cerebral infarction on diffusion-weighted images with short diffusion times," *Neuroradiology*, vol. 60, no. 9, pp. 979–982, 2018. 37, 75, 88

[91] M. Iima, A. Yamamoto, M. Kataoka, Y. Yamada, K. Omori, T. Feiweier, and K. Togashi, "Time-dependent diffusion mri to distinguish malignant from benign head and neck tumors," *Journal of Magnetic Resonance Imaging*, 2018. 37, 75

[92] T. Maekawa, M. Hori, K. Murata, T. Feiweier, C. Andica, I. Fukunaga, S. Koshino, A. Hagiwara, K. Kamiya, K. Kamagata, *et al.*, "Choroid plexus cysts analyzed using diffusion-weighted imaging with short diffusion-time," *Magnetic Resonance Imaging*, vol. 57, pp. 323–327, 2019. 37, 75, 88

[93] A. Arbabi, J. Kai, A. R. Khan, and C. A. Baron, "Diffusion dispersion imaging: Mapping oscillating gradient spin-echo frequency dependence in the human brain," *Magnetic Resonance in Medicine*, 2019. 37, 75, 88, 89, 93

[94] D. K. Jones, D. C. Alexander, R. Bowtell, M. Cercignani, F. Dell'Acqua, D. J. McHugh, K. L. Miller, M. Palombo, G. J. Parker, U. Rudrapatna, *et al.*, "Microstructural imaging of the human brain with a 'super-scanner': 10 key advantages of ultra-strong gradients for diffusion mri," *NeuroImage*, vol. 182, pp. 8–38, 2018. 39

[95] K. C. McPhee and A. H. Wilman, "T1 and t2 quantification from standard turbo spin echo images," *Magnetic Resonance in Medicine*, vol. 81, no. 3, pp. 2052–2063, 2019. 44

[96] T. Maekawa, M. Hori, K. Murata, T. Feiweier, I. Fukunaga, C. Andica, A. Hagiwara, K. Kamagata, S. Koshino, O. Abe, *et al.*, "Changes in the adc of diffusion-weighted mri with the oscillating gradient spin-echo (ogse) sequence due to differences in substrate viscosities," *Japanese Journal of Radiology*, vol. 36, no. 7, pp. 415–420, 2018. 46

[97] A. Leemans, B. Jeurissen, J. Sijbers, and D. K. Jones, "ExploreDTI: a graphical toolbox for processing, analyzing, and visualizing diffusion MR data," *Proceedings 17th Scientific Meeting International Society for Magnetic Resonance in Medicine*, vol. 17, no. 2, p. 3537, 2009. 51, 79

[98] J. W. Gibbs, "Fourier's series," *Nature*, vol. 59, no. 1522, p. 200, 1898. 65

[99] G. J. Barker, G. J. M. Parker, and C. A. Wheeler-Kingshot, "Gibbs ringing and negative adc values," in *Proceedings of the 9th Annual Meeting of International Society for Magnetic Resonance in Medicine*, 2001. 66

[100] D. Perrone, J. Aelterman, A. Pižurica, B. Jeurissen, W. Philips, and A. Leemans, "The effect of gibbs ringing artifacts on measures derived from diffusion mri," *NeuroImage*, vol. 120, pp. 441–455, 2015. 67, 69, 76, 80

[101] J. Veraart, I. O. Jelescu, F. Knoll, D. S. Novikov, and E. Fieremans, "Gibbs ringing in diffusion MRI," *Magnetic Resonance in Medicine*, vol. 76, no. 1, pp. 301–314, 2015. 67, 69, 76

[102] R. Archibald and A. Gelb, "A method to reduce the gibbs ringing artifact in mri scans while keeping tissue boundary integrity," *IEEE Transactions on Medical Imaging*, vol. 21, no. 4, pp. 305–319, 2002. 69

[103] S. A. Sarra, "Digital total variation filtering as postprocessing for Chebyshev pseudospectral methods for conservation laws," *Numerical Algorithms*, vol. 41, no. 1, pp. 17–33, 2006. 69

[104] K. T. Block, M. Uecker, and J. Frahm, "Suppression of mri truncation artifacts using total variation constrained data extrapolation," *International Journal of Biomedical Imaging*, 2008. 69

[105] E. Kellner, B. Dhital, V. G. Kiselev, and M. Reisert, "Gibbs-ringing artifact removal based on local subvoxel-shifts," *Magnetic Resonance in Medicine*, vol. 76, no. 5, pp. 1574–1581, 2016. 69, 76, 89

[106] G. Bydder and I. Young, "Mr imaging: Clinical use of the inversion recovery sequence," 1985. 72, 77

[107] A. H. Herlihy, J. V. Hajnal, W. L. Curati, N. Virji, A. Oatridge, B. K. Puri, and G. M. Bydder, "Reduction of csf and blood flow artifacts on flair images of the brain with k-space reordered by inversion time at each slice position (krisp)," *American Journal of Neuroradiology*, vol. 22, no. 5, pp. 896–904, 2001. 72

[108] A. H. Herlihy, A. Oatridge, W. L. Curati, B. K. Puri, G. M. Bydder, and J. V. Hajnal, "Flair imaging using nonselective inversion pulses combined with slice excitation order cycling and k-space reordering to reduce flow artifacts," *Magnetic Resonance in Medicine*, vol. 46, no. 2, pp. 354–364, 2001. 72

[109] G. Trifan, R. Gattu, E. M. Haacke, Z. Kou, and R. R. Benson, "Mr imaging findings in mild traumatic brain injury with persistent neurological impairment," *Magnetic Resonance Imaging*, vol. 37, pp. 243–251, 2017. 72

[110] R. E. Gabr, K. M. Hasan, M. E. Haque, F. M. Nelson, J. S. Wolinsky, and P. A. Narayana, "Optimal combination of flair and t2-weighted mri for improved lesion contrast in multiple sclerosis," *Journal of Magnetic Resonance Imaging*, vol. 44, no. 5, pp. 1293–1300, 2016. 72

[111] R. E. Gabr, A. S. Pednekar, K. A. Govindarajan, X. Sun, R. F. Riascos, M. G. Ramırez, K. M. Hasan, J. A. Lincoln, F. Nelson, J. S. Wolinsky, *et al.*, "Patient-specific 3d flair for enhanced visualization of brain white matter lesions in multiple sclerosis," *Journal of Magnetic Resonance Imaging*, vol. 46, no. 2, pp. 557–564, 2017. 72

[112] K. Kwong, R. McKinstry, D. Chien, A. Crawley, J. Pearlman, and B. Rosen, "Csf-suppressed quantitative single-shot diffusion imaging," *Magnetic Resonance in Medicine*, vol. 21, no. 1, pp. 157–163, 1991. 72, 77

[113] C. Beaulieu, A. De Crespigny, D. C. Tong, M. E. Moseley, G. W. Albers, and M. P. Marks, "Longitudinal magnetic resonance imaging study of perfusion and diffusion in stroke: Evolution of lesion volume and correlation with clinical outcome," *Annals of Neurology*, vol. 46, no. 4, pp. 568–578, 1999. 72, 77

[114] N. G. Papadakis, K. M. Martin, M. H. Mustafa, I. D. Wilkinson, P. D. Griffiths, C. L.-H. Huang, and P. W. Woodruff, "Study of the effect of csf suppression on white matter diffusion anisotropy mapping of healthy human brain," *Magnetic Resonance in Medicine*, vol. 48, no. 2, pp. 394–398, 2002. 72, 77

[115] L. Concha, D. W. Gross, and C. Beaulieu, "Diffusion tensor tractography of the limbic system," *American Journal of Neuroradiology*, vol. 26, no. 9, pp. 2267–2274, 2005. 72, 77

[116] G. Thomalla, P. Rossbach, M. Rosenkranz, S. Siemonsen, A. Krützelmann, J. Fiehler, and C. Gerloff, "Negative fluid-attenuated inversion recovery imaging identifies acute ischemic stroke at 3 hours or less," *Annals of Neurology*, vol. 65, no. 6, pp. 724–732, 2009. 72

[117] P. P. Mitra, P. N. Sen, and L. M. Schwartz, "Short-time behavior of the diffusion coefficient as a geometrical probe of porous media," vol. 47, no. 14, pp. 8565–8574, 1993. 74

[118] J. E. Tanner and E. O. Stejskal, "Restricted self-diffusion of protons in colloidal systems by the pulsed-gradient, spin-echo method," *The Journal of Chemical Physics*, vol. 49, no. 4, pp. 1768–1777, 1968. 74

[119] M. Mercredi, T. J. Vincent, C. P. Bidinosti, and M. Martin, "Assessing the accuracy of using oscillating gradient spin echo sequences with axcaliber to infer micron-sized axon diameters," *Magnetic Resonance Materials in Physics, Biology and Medicine*, vol. 30, no. 1, pp. 1–14, 2017. 75

[120] L. S. Kakkar, O. F. Bennett, B. Siow, S. Richardson, A. Ianuş, T. Quick, D. Atkinson, J. B. Phillips, and I. Drobnjak, "Low frequency oscillating gradient spin-echo sequences improve sensitivity to axon diameter: An experimental study in viable nerve tissue," *NeuroImage*, vol. 182, pp. 314–328, 2018. 75

[121] D. Wu, L. J. Martin, F. J. Northington, and J. Zhang, “Oscillating gradient diffusion mri reveals unique microstructural information in normal and hypoxia-ischemia injured mouse brains,” *Magnetic Resonance in Medicine*, vol. 72, no. 5, pp. 1366–1374, 2014. 75

[122] S. Y. Huang, Q. Tian, Q. Fan, T. Witzel, B. Wichtmann, J. A. McNab, J. D. Bireley, N. Machado, E. C. Klawiter, C. Mekkaoui, *et al.*, “High-gradient diffusion mri reveals distinct estimates of axon diameter index within different white matter tracts in the in vivo human brain,” *Brain Structure and Function*, pp. 1–15, 2019. 75, 91

[123] G. J. Barker, G. Parker, and C. Wheeler-Kingshott, “Gibbs Ringing and Negative ADC Values,” *Proceedings of the 9th Annual Meeting of International Society for Magnetic Resonance in Medicine*, p. 1546, 2001. 76, 88

[124] P. A. Yushkevich, J. Piven, H. C. Hazlett, R. G. Smith, S. Ho, J. C. Gee, and G. Gerig, “User-guided 3D active contour segmentation of anatomical structures: Significantly improved efficiency and reliability,” *NeuroImage*, vol. 31, no. 3, pp. 1116–1128, 2006. 79

[125] J. Tanner, “Self diffusion of water in frog muscle,” *Biophysical Journal*, vol. 28, no. 1, pp. 107–116, 1979. 91

[126] W. W. Campbell and R. N. DeJong, *DeJong’s the neurologic examination*, 2005. Lippincott Williams & Wilkins, 2005. 91

[127] D. Liewald, R. Miller, N. Logothetis, H.-J. Wagner, and A. Schüz, “Distribution of axon diameters in cortical white matter: An electron-microscopic study on three human brains and a macaque,” *Biological Cybernetics*, vol. 108, no. 5, pp. 541–557, 2014. 91

[128] S. Groeschel, G. E. Hagberg, T. Schultz, D. Z. Balla, U. Klose, T.-K. Hauser, T. Nägele, O. Bieri, T. Prasloski, A. L. MacKay, *et al.*, “Assessing white matter microstructure in brain regions with different myelin architecture using mri,” *PLoS One*, vol. 11, no. 11, e0167274, 2016. 91

[129] M. Nilsson, S. Lasič, I. Drobnjak, D. Topgaard, and C.-F. Westin, “Resolution limit of cylinder diameter estimation by diffusion mri: The impact of gradient waveform and orientation dispersion,” *NMR in Biomedicine*, vol. 30, no. 7, e3711, 2017. 91

[130] E. Fieremans, L. M. Burcaw, H.-H. Lee, G. Lemberskiy, J. Veraart, and D. S. Novikov, “In vivo observation and biophysical interpretation of time-dependent diffusion in human white matter,” *NeuroImage*, vol. 129, pp. 414–427, 2016. 92

[131] D. C. Alexander, T. B. Dyrby, M. Nilsson, and H. Zhang, “Imaging brain microstructure with diffusion mri: Practicality and applications,” *NMR in Biomedicine*, vol. 32, no. 4, e3841, 2019. 92